Diplomarbeit

The impact of ATGL on metabolism and angiogenesis in A549 lung carcinoma cell line under hypoxia

eingereicht von

Isra Hatab

zur Erlangung des akademischen Grades

Doktor(in) der gesamten Heilkunde

(Dr. med. univ.)

an der

Medizinischen Universität Graz

ausgeführt am

Lehrstuhl für Immunologie und Pathophysiologie,
Otto Loewi Forschungszentrum für Gefäßbiologie, Immunologie und Entzündung

unter der Anleitung von

Univ.-Ass.in Priv.-Doz.in Mag.a Dr.in Nassim Ghaffari Tabrizi-Wizsy

Dr.in Tamara Tomin

Graz, am 23.11.2020

Eidesstattliche Erklärung

Ich erkläre ehrenwörtlich, dass ich die vorliegende Arbeit selbstständig und ohne fremde Hilfe verfasst habe, andere als die angegebenen Quellen nicht verwendet habe und die den benutzten Quellen wörtlich oder inhaltlich entnommenen Stellen als solche kenntlich gemacht habe.

Graz, am 23.11.2020 *Isra Hatab eh.*

Acknowledgment

First, I would like to express my sincere gratitude to Univ. Ass. Dr. Nassim Ghaffari Tabrizi-Wizsy for providing me the topic, supervising my work, being very supportive and encouraging at each step of my work, and who saw and believed on my abilities and potentials. A special thank to Dr.Tamara Tomin for her guidance and support, assisting me on the proteomics analysis as well giving me insightful and constructive feedbacks on my thesis. Also, a huge thank to everybody working at the Division of Immunology and Pathophysiology, Otto Loewi Research Center, for taking their time showing and teaching me the essential laboratory skills for my research. My sincere thanks also go to Assoc. Prof. Dr. Andelko Hrzenjak at the Division of Pulmonology, Department of Internal Medicine for his assistance and giving me the opportunity to use their lab for my thesis. A huge thank goes to all my friends and colleagues, who were there for me during my medical studies.

Last but not least, I am very grateful for the endless support and encouragement from my parents and siblings who have always been there at my side throughout my life and wishing me all the bests.

Table of Contents

Abbreviations

3D	3-dimensional
Acetyl-CoA	acetyl-coenzyme A
ACN	acetonitrile
AI	angiogenesis index
ATGL	adipose triglyceride lipase
ATP	adenosine triphosphate
BCA-RAC	bicinchoninic acid-reducing agent compatible
bFGF	basic fibroblast growth factor
BM	basement membrane
BSA	bovine serum albumin
CAA	chloroacetamide
CAM	chorioallantoic membrane
DAG	diacylglycerol
EC	endothelial cell
ECM	extracellular matrix
ER	endoplasmic reticulum
FA	fatty acid
FBS	fetal bovine serum
FDR	false discovery rate
FFA	free fatty acid
GO	gene ontology
GOBP	Gene Ontology Biological Process
H&E	Hematoxylin and Eosin
HEPES	4-(2-hydroxyethyl)-1-piperazineethanesulfonic acid
HIF	hypoxia-inducible factor
HSL	hormone-sensitive lipase
IARC	International Agency for Research on Cancer
KO	knock out
LC-MS/MS	liquid chromatography - tandem mass spectrometry
LD	lipid droplet
LDH	lactate dehydrogenase

LFQ	label free quantitation
MAGL	monoacylglycerol lipase
MEM	Minimum Essential Medium
MMP	matrix metalloproteinase
mRNA	messenger ribonucleic acid
NADPH	nicotinamide adenine dinucleotide phosphate
NSCLC	non-small cell lung carcinoma
P/S	penicillin/streptomycin
PBS	phosphate-buffered saline
PDK	pyruvate dehydrogenase kinase
PPP	pentose phosphate pathway
RMPI-160	Rosswell Park Memorial Institute-1640
RT	room temperature
SCLC	small cell lung carcinoma
SDS	sodium dodecyl sulfate
SE	standard error
SMC	smooth muscle cell
SREBP-1	sterol regulatory element-binding protein 1
TAG	triacylglyceride
TCA	tricarboxylic acid cycle,
TCEP	tris(2-carboxyethyl)phosphine
TFA	trifluoracetic acid
TFE	trifluoroethanol
TSP-1	thrombospondin-1
uPA	urokinase-type plasminogen activator
UV	ultraviolet
VEGF	vascular endothelial growth factor
WT	wild type

List of Figures

List of Tables

Zusammenfassung

HINTERGRUND: Angiogenese und Stoffwechselanpassungen treten als Reaktion auf das schnelle Wachstum der Tumorzellen und die Hypoxie im Tumorgewebe auf. Hypoxie führt unter anderem zu einer Reduktion von Adipozyten-Triglyzerid-Lipase (ATGL) in Lungentumorzellen durch die Aktivierung des Hypoxie-induzierten Faktors-1 (HIF-1). Das Ziel dieser Studie war es, den Einfluss von Hypoxie auf den zellulären Metabolismus sowie auf die Angiogenese in der ATGL-defizienten A549-Zellline zu untersuchen.

METHODEN: Die Lungenadenokarzinomzelllinie A549 Wildtyp (WT) und ATGL Knockout (KO) wurden in dreidimensionaler Zellkultur unter 21% oder 1% Sauerstoff kultiviert. An den gesammelten Sphäroiden von WT und ATGL-KO wurde die Proteinzusammensetzung analysiert. Überstände der Sphäroide wurden *in vivo* Angiogenese-Assay verwendet und neu gebildete Blutgefäße gezählt.

ERGEBNISSE: Unsere Studie zeigte eine Zunahme der Glykolyse sowie der Biosynthese von Lipiden und Proteinen in der ATGL-KO Gruppe im Vergleich zur WT Gruppe unter Normoxie. Darüber hinaus wurde ein Anstieg des Proteinstoffwechsels bei den normoxischen WT-Sphäroiden gegenüber den hypoxischen nachgewiesen. Zusätzlich wurde ein geringer Unterschied in der Proteinzusammensetzung zwischen WT und ATGL-KO unter Hypoxie und zwischen der normoxischen und hypoxischen ATGL-KO Gruppe beobachtet.
Im CAM-Assay sehen wir einen signifikanten Unterschied in der Angiogenese ausschließlich in der A549-WT Gruppe gegenüber ATGL-KO unter 21% O_2 (0,38 ± 0,03 gegenüber 0,29 ± 0,03) (p = 0,018).

SCHLUSSFOLGERUNG: Entsprechende frühere Studien zeigten unsere Ergebnisse, dass der Warburg-Effekt und Proliferation der Tumorzellen durch den Verlust von ATGL gefördert wird. Ganz im Gegenteil erwies sich ATGL im *in vivo* Assay als pro-angiogenetischer Faktor, ihr Signalweg ist jedoch unklar. Weiterhin zeigen ATGL-defiziente und hypoxische A549-Zellen einen ähnlichen Phänotyp.
Zusammenfassend spielt ATGL eine wichtige Rolle im Metabolismus von Lungenkarzinom und kann als potenzieller prognostischer und therapeutischer

Faktor verwendet werden. Die Funktion des ATGL-Verlustes könnte über den HIF-1-Signalweg vermittelt werden.

Abstract

BACKGROUND: Tumor cells perform angiogenesis and metabolic adjustments in response to their rapid growth and hypoxic microenvironment. Reduced levels of adipose triglyceride lipase (ATGL) - an enzyme involved in lipolysis - was reported in lung cancer cells and is associated with tumorigenesis, invasion and metastasis. Beside upregulation of angiogenesis and glycolysis, hypoxia lowers the expression of ATGL through activation of hypoxia inducible factor-1 (HIF-1).
The aim of this study was to investigate the effect of hypoxia on the metabolism and angiogenic properties in ATGL deficient A549 cell line.

METHODS: The lung adenocarcinoma cell line A549 wild type (WT) and ATGL knockout (KO) were cultivated in 3-dimensional cell culture under 21% or 1% oxygen. Label free quantitative (LFQ) proteomic analysis was performed on the collected spheroids of WT and ATGL-KO. Supernatants of the spheroids were used in the chorioallantoic membrane (CAM) angiogenesis assay and newly formed blood vessels were counted.

RESULTS: Our results from the proteomic analysis revealed an enhancement of glycolysis in the ATGL-KO than in WT cells under normoxia, following an increase in the anabolic reactions of lipid and protein. Furthermore, an increase of protein metabolism was seen in the normoxic compared to hypoxic WT spheroids. In addition, minor difference in the proteome composition was observed between WT and ATGL-KO under hypoxia and between normoxic and hypoxic ATGL-KO group. In the CAM assay, we observed significant angiogenic changes only in the A549-WT group versus ATGL-KO under 21% O_2 (0.38 ± 0.03 vs 0.29 ± 0.03) (p = 0.018).

CONCLUSION: Our results corresponded to previous studies, that loss of ATGL promotes Warburg effect, as well as induces proliferation of tumor cells. On the contrary, ATGL showed to be a proangiogenic factor in the *in vivo* assay, yet their signaling pathway is unclear. Further on, ATGL deficient and hypoxic A549 cells manifest similar phenotype.

In conclusion, ATGL plays a significant role in the metabolism of NSCLC and can be used as potential prognostic and therapeutic factor. The function of ATGL deficiency could be mediated via the HIF-1 signaling pathway.

1 Introduction

Worldwide, lung cancer is one of the most common cancers with an incidence rate of 11.6% (2.09 million cases) and a leading cause of cancer death with a mortality rate of 18.4% (1.76 million deaths) according to the data from Globocan 2018 by the International Agency for Research on Cancer (IARC) (Figure 1) (1). Smoking cigarettes is considered as the main risk factor causing about 80-85% of all lung cancer cases worldwide (2).

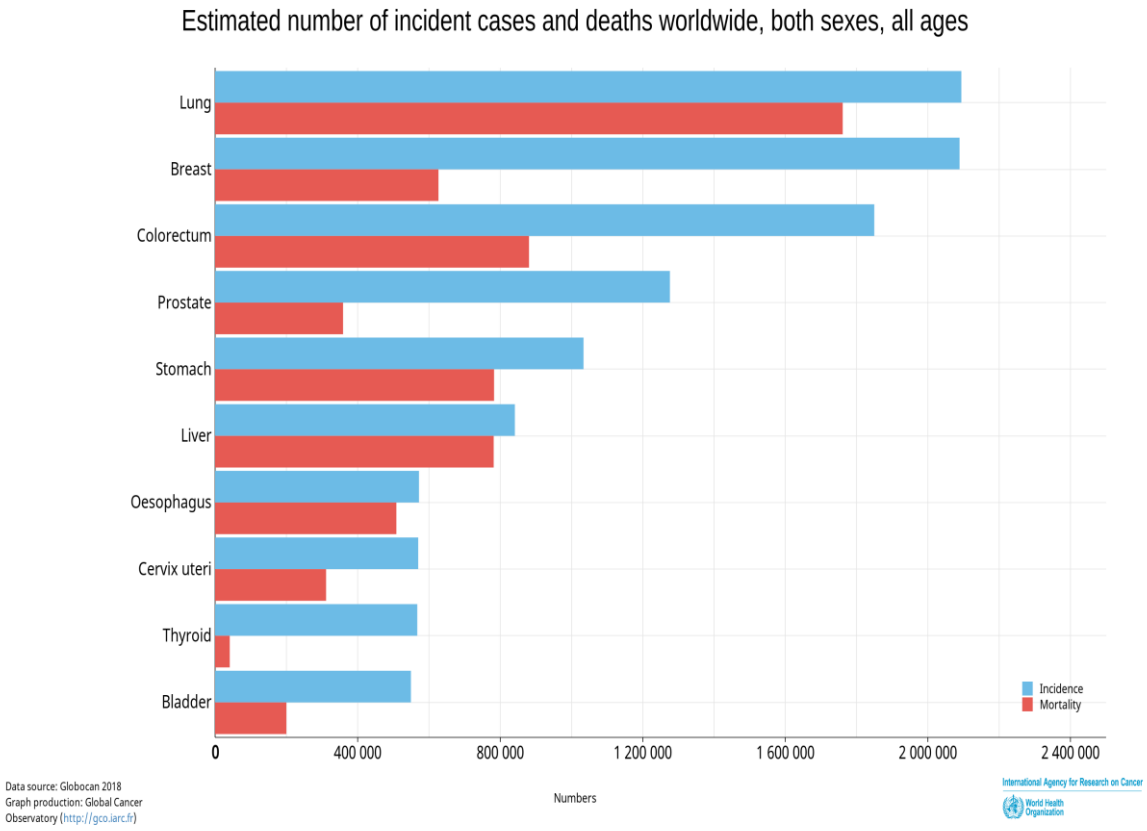

Figure 1. Number of incidence and mortality of the top ten tumors worldwide in both sexes and all ages in 2018 (3)

Lung cancer arising from the respiratory epithelium is categorized histologically into two main groups namely small cell lung carcinoma (SCLC) and non-small cell lung carcinoma (NSCLC) (4). The latter represents the majority of lung tumors and is then further differentiated into 3 main types: adenocarcinoma, squamous cell carcinoma and large cell carcinoma (4). Due to reducing tobacco consumption, the incidence rate of squamous cell carcinoma is beginning to decrease making adenocarcinoma recently the most common lung carcinoma type, that is seen more frequently in women and never-smokers (5, 6).

Even though cancer therapy has improved in recent years, lung carcinoma still has a poor prognosis with a 5-year survival rate of 10-20%, mainly due to the very late cancer diagnosis with distant metastases (2). Many studies are investing in understanding the biology of lung cancer in order to develop more effective and potent diagnostic and therapeutic modalities (7).

Tumor angiogenesis, one of the hallmarks of cancer (Figure 2), plays a central role in the tumor growth and progression (8, 9), and has been addressed in targeted drug therapy (10). Microenvironmental factors such as hypoxia has a massive impact on tumor angiogenesis through upregulation of hypoxia-inducible factor-1 (HIF-1) (11, 12).

Observations on tumor angiogenesis including NSCLC have been successfully performed with the chick embryo chorioallantoic membrane (CAM) model (10, 13), however, one of its difficulties lies in incubation of chick embryos at oxygen concentration lower than 15% over 1-3 days (14, 15).

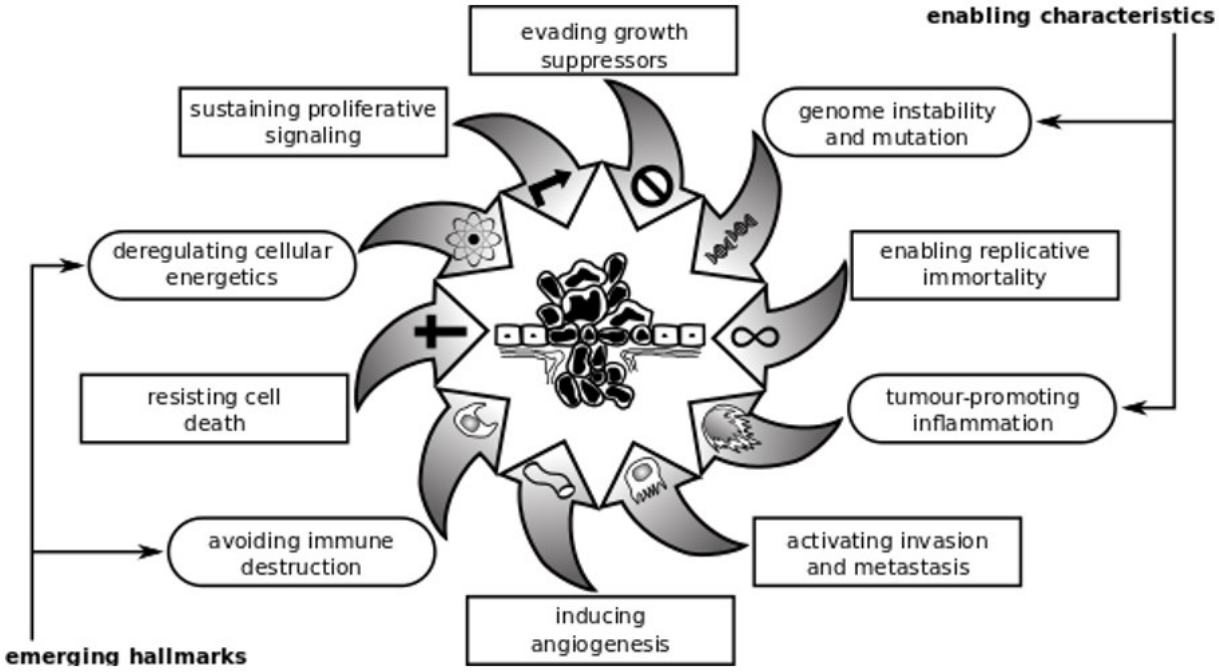

Figure 2. The hallmarks of cancer. In 2011 Hanahan and Weinberg have extended the hallmarks of cancer from 6 to 8 factors. Angiogenesis and reprogramming cellular energetics represent crucial factors in transformation of normal cells into malignant tumor cells (16).

In the past years, increasing attention has been dedicated to investigation of cancer metabolism as potential drug target, especially glucose metabolism (17). While disturbed glucose metabolism is a known cancer hallmark (9) (Figure 2), much less is known regarding the lipid metabolism, especially with regards to lung

cancer. Interestingly, a study carried by Al-Zoughbi *et al.* noticed deletion of adipose triglyceride lipase (ATGL) gene in 38% of lung cancer and a decrease in mRNA levels of ATGL was present especially in NSCLC (18) which could probably increase the cancer aggressiveness (19). ATGL seems to be particularly important in hypoxia, as the activation of HIF-1 leads to potent inhibition of ATGL enzyme (20, 21).

In the last decades, increasing studies are exploring the implication of lipogenesis on tumor biology, however, very few have approached on the role of lipolysis and ATGL in tumorigenesis. In addition to that, the involvement of lipolysis on tumor angiogenesis is still unclear.

Therefore, as part of this study we investigated the impact of ATGL deficiency on the proteome composition of spheroids of A549 lung carcinoma cell line, cultivated under normoxic or hypoxic conditions. In addition to that, the angiogenic response to ATGL and hypoxia in an *in vivo* model employing supernatants of the A549 spheroids was investigated.

1.1 Tumor Metabolism

One of the distinct traits of malignant tumor cells is their rapid continuous growth, thus they acquire a greater energy and nutrient requirement as to normal tissue cells (22, 23). In order to effectively compensate their increased mitotic activity and growth, tumor cells display alteration in cellular energy metabolism and increased biosynthesis of biomass (24). Otto Warburg first acknowledged the metabolic modifications in cancer cells (25). He described that tumor cells can reprogram their glucose metabolism and depend primarily on glycolysis for adenosine triphosphate (ATP) production, regardless of the environmental oxygen levels. This phenomenon was described as *aerobic glycolysis* or *Warburg effect* (25).

As is well known, glycolysis generates fewer ATP as the mitochondrial oxidative phosphorylation (17, 24). This triggers cancer cells to substantially elevate the glucose uptake by upregulation of glucose transporters in the plasma membrane of tumor cells (17, 24). The increased glucose uptake has been documented with nuclear medicine imaging, which has been useful in tumor diagnosis and monitoring of neoplastic development including lung cancer (17, 26).

Over the past decades, numerous studies have demonstrated the importance of reprogramming of the cellular energy metabolism in cancer development and was recognized in this decade by Hanahan and Weinberg as an emerging hallmark of cancer (9).

Despite the low efficiency of glycolysis in energy production, glycolytic intermediates are found to be necessary in assembling new cells, as they serve substrates for biosynthesis of nucleotides, proteins and lipids (25).

Latest studies have shown the contribution of microenvironmental changes, alongside to genomic alterations, in the metabolic switch (23, 26). Cancer cells are often exposed to oxygen-deficient surroundings. In response to the elevated levels of HIF-1α, cells switch to anerobic respiration and rely primarily on glycolysis in energy production (23, 27, 28).

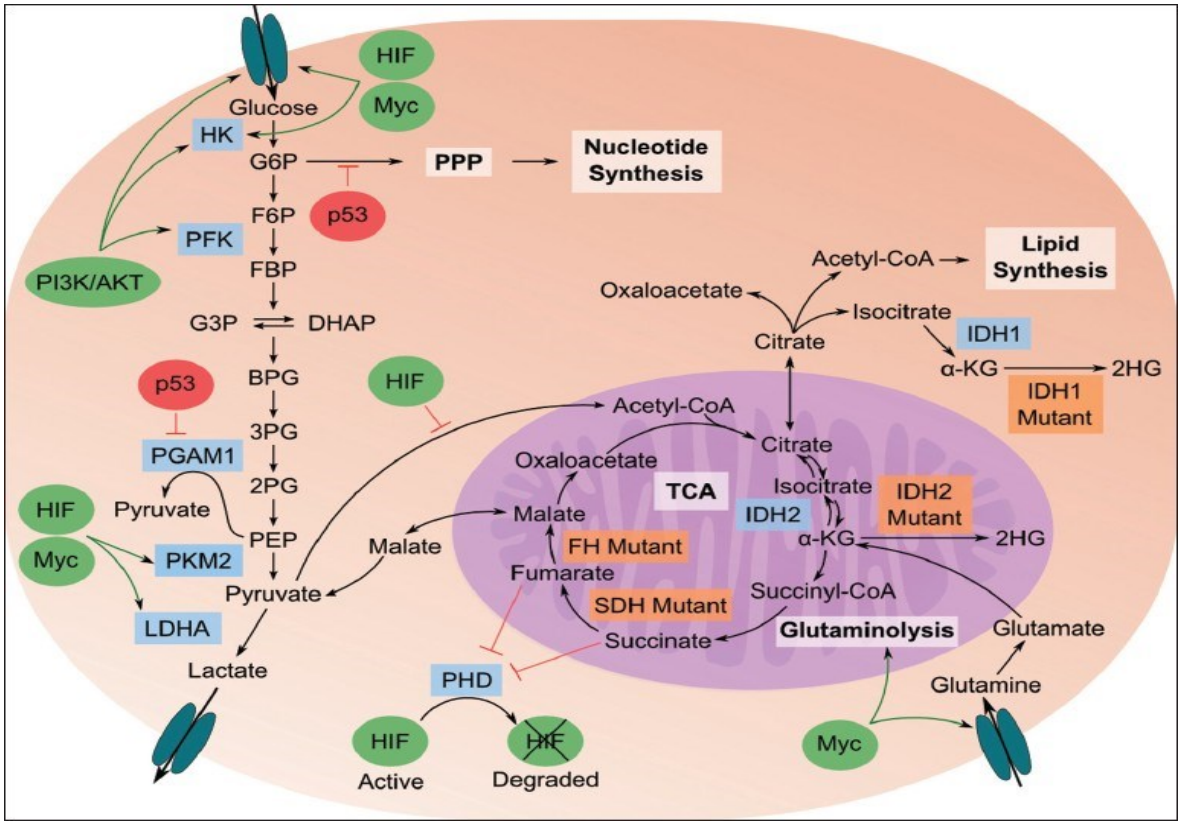

Figure 3. Overview of tumor metabolism (29)

Interestingly, researches are investigating the correlation of glucose metabolism to angiogenesis. It has been reported that succinate dehydrogenase and fumarase, enzymes involved in the tricarboxylic acid cycle (TAC), were found mutated in some types of cancer, leading to activation of HIF-1, consequently stimulating the

angiogenic pathway (30, 31). In addition, accumulation of lactate may have proangiogenic properties, through stabilization of HIF-1 in an oxygen-independent manner (32, 33).

Further modifications in the metabolic pathway to cope the rapid cellular growth and division is the enhanced mitochondrial biogenesis and biosynthesis of proteins, nucleotides and lipids (26). Carbon molecules for the macromolecular biogenesis yield excessively from glutamine and glucose metabolism (25). Studies have found that metabolic phenotypes differ depending on tissue type (34), as well as between tumor cells within a cancer type (9).

In the past years, increasing attention has been dedicated to investigation of cancer metabolism as a potential drug target, especially glucose metabolism (17). However, challenges can present with antineoplastic treatment targeting specific metabolic control points, in which cancer cells can provoke alternative metabolic pathways in order to compensate the targeted one, thereby weakening the effectiveness of the therapy (17, 26).

1.2 Lipid Metabolism

Recently, many studies are focusing on impairments of lipid metabolism in solid cancer cells. Lipids are generally necessary for the cell survival, as they are structural components of the biological membranes, function as signaling molecules and serve as primary energy reservoir (26). Although lipid metabolism is typically eminently manifested in adipose tissue and hepatocytes, upregulation of free fatty acid (FFA) and lipoprotein uptake and *de novo* lipogenesis have been viewed in tumor cells (24, 35). Main requirements of fatty acid (FA) synthesis are acetyl-coenzyme A (CoA) and nicotinamide adenine dinucleotide phosphate (NADPH), which arise from TCA and pentose phosphate pathway (PPP) respectively, and is controlled by transcription factor, sterol regulatory element-binding protein 1 (SREBP-1) (24), which was found in high levels in some types of cancers (35). The assembled FAs accumulate then in the cytoplasm of tumor cells as triacylglyceride (TAG) and cholesterol forming lipid droplets (LDs) (22). Lipid metabolism has been linked to tumor proliferation, invasion, metastasis and angiogenesis (35), as well it is associated with poor prognosis (36).

When synthesized FAs and cholesterol exceed the demands of cells, they are consumed in formation of TAG and cholesteryl ester catalyzed by enzymes localized in the endoplasmic reticulum (ER), afterwards they accumulate and store within LDs (37). LDs - subcellular organelles - are surrounded by a single biomembrane derived from ER and located in the cytoplasm of a cell and serve primarily as energy storage and lipid reservoir of biological membranes (37-39). LDs are seen in enormous amount in cells with high lipid metabolic activity such as fat and liver cells (40). Likewise, they were then spotted in most types of cells (40). As intense interest on lipid metabolism in cancer has grown, accumulation of LDs were recognized in various types of solid tumor cells (38, 41-43), following their aberrant lipid metabolic profile (44).

When cellular lipid needs for energy production and anabolic processes exceed the limited exogenous FAs and lipid delivery, mobilisation of LDs and lipolysis of stored TAGs are performed (39). TAG is hydrolyzed initially by ATGL into diacylglycerol (DAG) and one FA, then DAG is degraded by hormone-sensitive lipase (HSL) and monoacylglycerol lipase (MAGL) resulting glycerol and free fatty acids (Figure 4) (39).

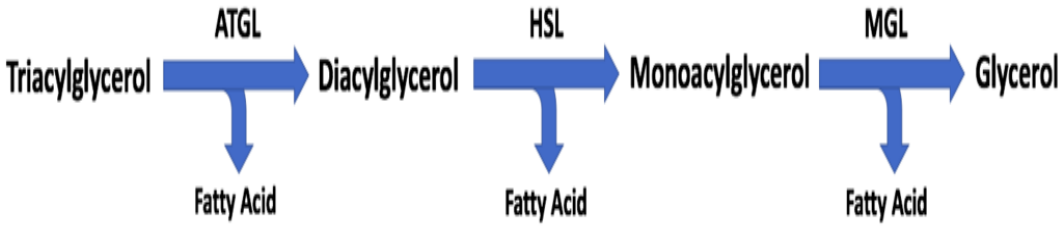

Figure 4. Lipolysis of TAG. Diagram shows hydrolytic cleavage of TAG into end-products of FA and glycerol (45).

1.3 Adipose Triglyceride Lipase (ATGL)

ATGLs play an essential role in energy homeostasis as they feature TAG-hydrolase activity (46). They are patatin domain-containing proteins, composed of 504 amino acids (47) and are localized in the cytoplasm and on the surface of LDs of both adipose and non-adipose tissues (46, 48). The ATGL activity is remarkably regulated by exogenous and endogenous molecules (47, 49).

Recently, several studies are showing large interest on contribution of ATGL in cancer, however, these findings were found controversial. A pervious study by Zagani *et al* showed that inactivation of ATGL leads to suppressing tumor growth and promoting apoptosis in NSCLC and hypothesized upregulation of ATGL owing to reduced expression of G0/G1 switch gene 2 (G0S2) in cancer (50). On the other side, other researchers observed mutation and depletion of ATGL mRNA and protein in various cancers linked with positive impact on neoplastic development (18, 51). Interestingly, a study carried by Al-Zoughbi *et al*. reported deletion of ATGL gene in 38% of lung cancer and decrease in mRNA levels of ATGL especially in NSCLC and a correlation with poor prognosis (18). Indeed, a review study suggested further implications of ATGL on other neoplastic processes including inflammation, autophagy and redox homeostasis (52).

ATGL and LDs seem to be particularly important in hypoxia, as the activation of HIF-1 leads to potent inhibition of ATGL enzyme (20, 21) contributed to an increased accumulation of LDs in the cytoplasm of hypoxic tumor cells (20, 53).

1.4 Hypoxia in Cancer

To present time, the role of hypoxia in tumorigenesis continues to receive an enormous interest in cancer studies. Tumor cells are chronically exposed to hypoxic surroundings owing to the limited oxygen supply in maintaining continuous cellular growth and proliferation (54).

Low oxygen levels signal multiple intracellular pathways to establish an adequate cellular adjustment, which are mediated predominantly by the overexpression of hypoxia inducible factors (HIFs) (55).

HIFs are a group of heterodimer transcription factors, composed of an oxygen-dependent α-subunit and an oxygen-independent β-subunit (56) (Figure 5). Each subunit is then divided into three isoforms (57). Regulation of hypoxia-induced alterations is performed chiefly by the isoform HIF-1α (58).

In the presence of oxygen, HIFs are usually inactivated by oxygen-sensitive prolyl-hydroxylase (57, 59). Prolyl hydroxylase adds hydroxy-groups on the α-subunits of HIFs, addressing them latterly for ubiquitination and proteasomal degradation (57, 59). In hypoxic conditions, prolyl hydroxylase is suppressed, allowing stabilization of HIF-1α (57, 59) (Figure 5).

HIF-1, through upregulation of numerous transcriptional genes, regulates a broad range of intracellular signaling pathways, which have a remarkable impact on tumor progression and survival among those energy metabolism and angiogenesis (55, 56) (Figure 5).

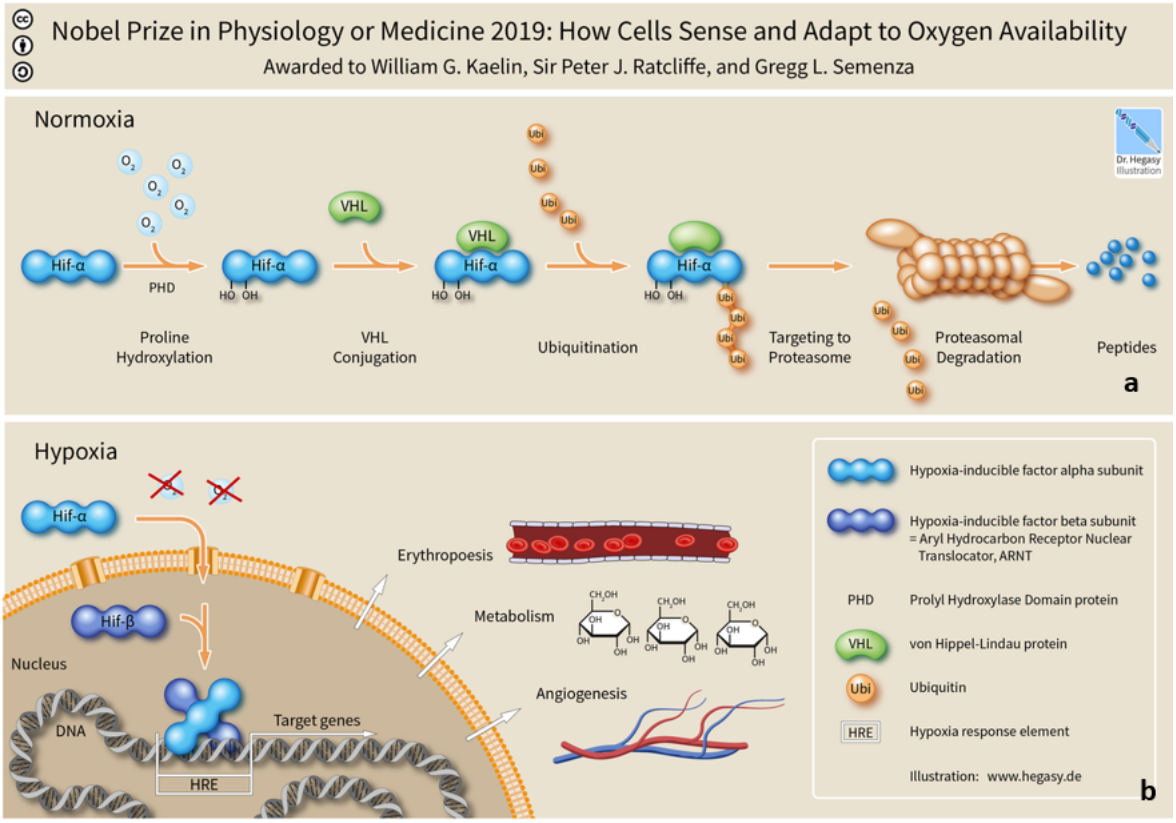

Figure 5. Structure, function and activation of HIF. a) In aerobic conditions, α-subunit of HIF is hydroxylated by prolyl hydroxylase, recognized by VHL for ubiquitination leading to proteasomal degradation. b) Under hypoxia, HIF is stabilized by inactivation of prolyl hydroxylase, then enters to nucleus and induces transcription of many proteins necessary for various cellular processes such as angiogenesis and energy metabolism (60).

Solid tumor cells undergo numerous gene expression changes in metabolic pathways mediated by HIF-1α, allowing them to grow and survive in a hypoxic environment (23). HIF-1 induces the catabolic pathway, glycolysis, by upregulating glucose transporter and glycolytic enzymes (23). Furthermore, HIF-1 shunts the glycolytic end-product pyruvate away from the TCA via activation of pyruvate dehydrogenase kinase (PDK) (27) and enzymatic reduction of pyruvate to lactate by activation of lactate dehydrogenase (LDH) (28). In addition, mitochondrial oxidative respiration is suppressed due to the oxygen deficiency (26, 56). As a

result, glycolysis is enhanced and delivers the main energy source to tumor cells under hypoxia (23, 26).

Moreover, HIF-1 has a positive impact on anabolic pathways. It upregulates biosynthesis of lipids (24, 53) and formation of LDs significantly (53, 61).

Further on, hypoxia or HIF-1α is one of the main triggers of the angiogenic switch in tumor cells, as elevated HIF-1α expression level induces upregulation of proangiogenic factors among those vascular endothelial growth factor (VEGF), which is the key mediator of neovascularization (54, 62).

Clinically, hypoxia or high levels of HIF-1 has seen to be associated with poor prognosis and low survival outcome in several human cancers including lung carcinoma (63).

1.5 Angiogenesis

Blood vessels supply tissues with oxygen (O_2) and nutrients and remove carbon dioxide (CO_2) and metabolic waste products (64). All types of blood vessels are composed of a single layer of endothelial cells (ECs), laying on a basement membrane (BM) (65). Larger blood vessels are surrounded additionally with layers of smooth muscle cells (SMCs) and connective tissues containing collagen and elastin fibers in variable amount and proportions (66-68). Whereas capillaries – the smallest blood vessels - contain pericytes surrounding the endothelium layer (67) (Figure 6). Among many functions of the mural cells (SMCs and pericytes), they are involved in formation of BM and extracellular matrix (ECM), perform supportive function and play a central role in maturation and stabilization of blood vessels during angiogenesis (9, 66, 69-72).

Formation of blood vessels occurs mainly through two distinct pathways, vasculogenesis and angiogenesis. Vasculogenesis refers to the *de novo* formation of blood vessels from mesodermal-derived endothelial precursors cells (angioblasts), typically seen during embryonic development, whereas angiogenesis is defined as sprouting newly blood vessels from pre-existing ones (73). Angiogenesis plays a vital role in physiological and pathological processes including endometrial proliferation, placental development, wound healing, inflammatory disorders and cancer (65, 74).

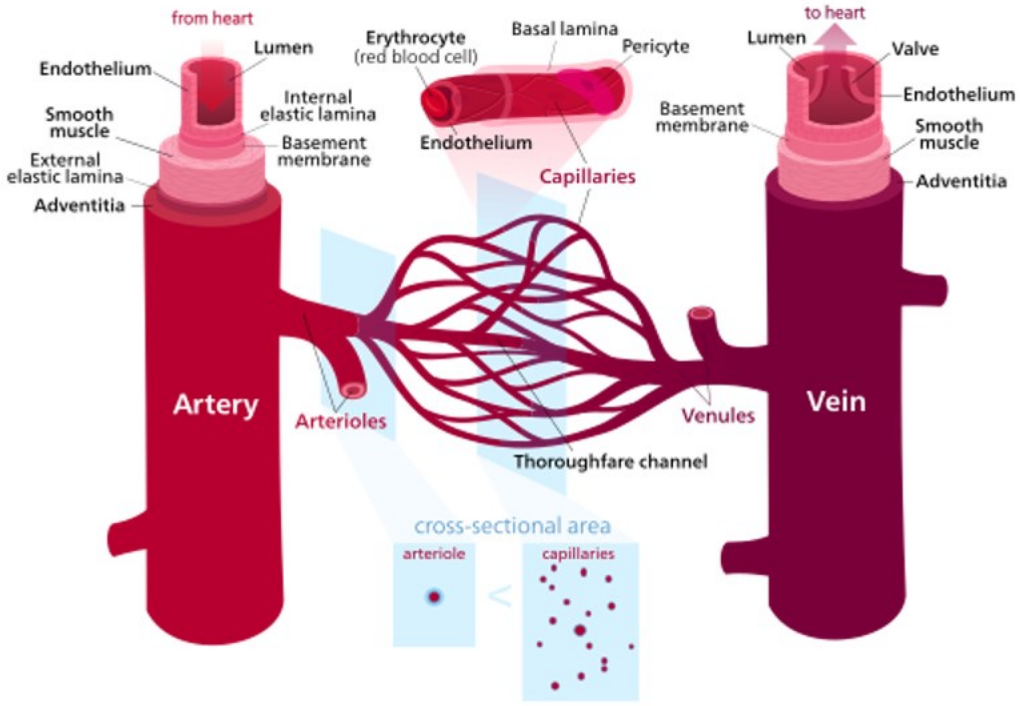

Figure 6. Structure of blood vessels. Classification of blood vessels in arteries, arterioles, veins, venules and capillaries. Diagram shows the basic histological structure of artery, vein and capillary (75).

The angiogenic process occurs in a series of consecutive steps regulated by various molecules acting as angiogenic stimulators or inhibitors (Figure 7) (76). These molecules are usually under physiological conditions in balance (12). One of the paramount angiogenic factors is VEGF (77). In response to an angiogenic stimulus, proangiogenic factors are remarkably upregulated (73). VEGF untightens the intercellular connection between the endothelial cells, thus increasing the vascular permeability (78-80). Afterwards proteolytic enzymes such as urokinase-type plasminogen activator (uPA) and matrix metalloproteinase (MMP) are activated and induce degradation of the BM and components of ECM, which enables lately migration of ECs (73, 81). Subsequently, numerous proangiogenic factors are released from the interstitial matrix (82). In response to the proangiogenic factors, endothelial cells are activated and transform into tip and stalk cells (64, 83). Tip cells form cytoplasmic projections known as filopodia and are able to migrate and invade in the surrounding ECM, whereas stalk cells undergo cell division forming new blood vessels (64, 83). Final stages of angiogenesis represent maturation and remodeling of newly formed vascular network (82). Stabilization of the vascular wall is provided by creation of

interendothelial junctions, production of basal lamina and recruitment of pericytes and SMCs (72, 73, 80). Furthermore, the ECs form the vascular lumen through intercellular junctions or intracellular vacuolation (84).

Endogenous anti-angiogenic factors play a critical role in inhibition of angiogenesis and prevent formation of unnecessary blood vessels (73). They regulate angiogenesis in various steps, for instance angiostatin inhibits proliferation of endothelial cells (85, 86) and thrombospondin-1 (TSP-1) hinders cellular migration and promotes apoptosis of ECs (87).

The understanding of angiogenesis has gain large interest in medicine in recent years. Development of drug therapy targeting angiogenic mediators has had benefits in treatment of cancer, inflammatory disorders and ocular diseases (77). In addition, stimulation of angiogenesis has been valued in revascularization of ischemic tissues (88, 89).

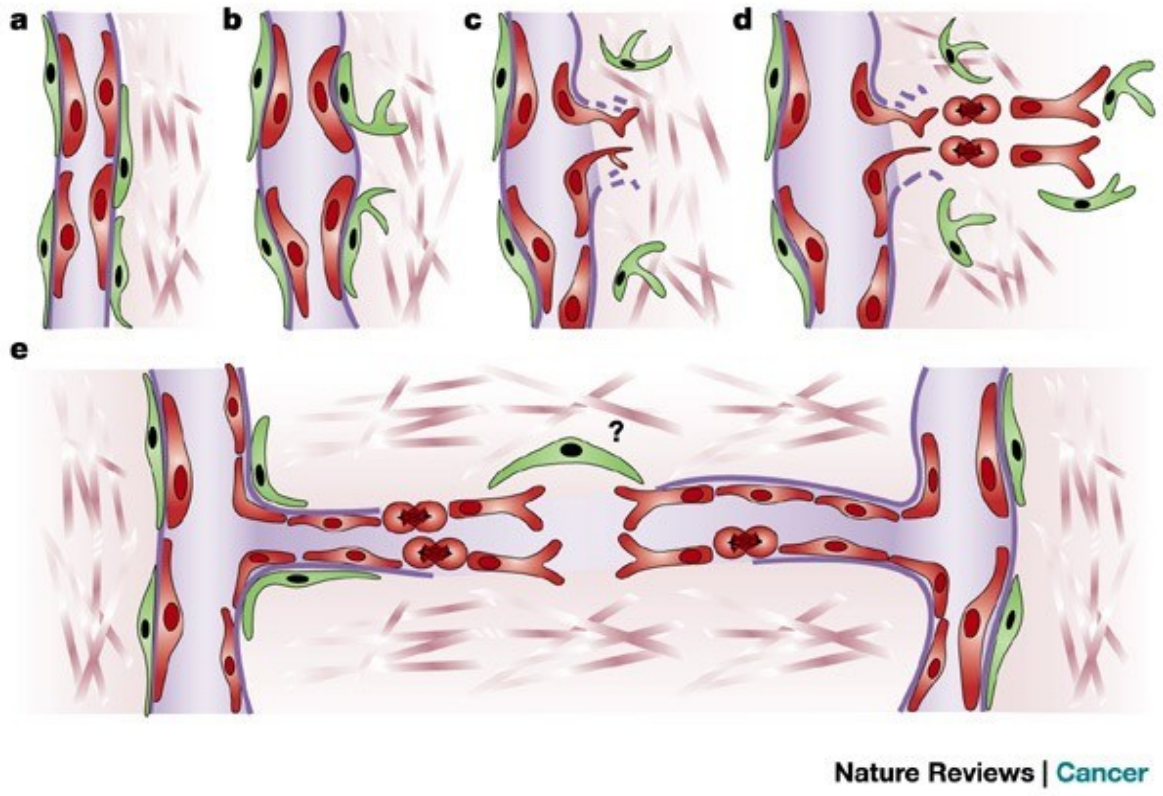

Figure 7. Mechanism of angiogenesis. Sprouting of new blood vessels from pre-existing ones occurs in several stages. a) Blood vessel, composed of ECs (red) and pericytes (green) and a basement membrane in between (purple), is found in quiescent state. b) In response to an angiogenic signal, angiogenesis is initiated with vascular dilation, loosening of adheres junctions between ECs, and detachment of pericytes. c) Afterwards, BM and ECM are degraded allowing migration of ECs. d) ECs undergo migration and proliferation forming a nascent blood vessel. e) Final stages of angiogenesis represent maturation and stabilization of newly formed blood vessels, which involves establishment of cell-cell junctions, formation of BM and recruitment of pericytes (76).

1.6 Tumor Angiogenesis

In initial stages of tumor development, nourishment of tumor cells is accomplished through diffusion, later on, an adequate vascular supply is required to cope with the rapid proliferation rate and high metabolic demands of tumor cells (76, 90). Genetic alterations in tumor cells or microenvironmental changes can disrupt the balance of angiogenic activators and inhibitors and therefore trigger the angiogenesis switch in favour of assembling of new aberrant vasculature (62, 76, 91). In addition, vascular enrichment in solid tumors enables tumor cells to metastasize to distant sites in the body, which is correlated with poor prognosis (92). As mentioned above, hypoxia is one of the main drivers of angiogenesis in cancer (62). The upregulation of HIF-1α induces overexpression of several proangiogenic factors, such as VEGF, basic fibroblast growth factor (bFGF), angiopoietin and others (54, 62). In comparison to normal tissue vessels, tumor vasculature is usually abnormal and characterized by morphological and functional defects (12, 72). Tumor vessels are found to be enlarged, highly permeable and form an instable, heterogenous, excessively branched vascular network (12, 72, 74, 93). As a result, tumor cells receive insufficient blood supply chiefly (12) due to the reduced and irregular blood flow leading in formation of hypoxic and hypoglycemic areas (93, 94). In addition, this could disrupt the distribution of medication to tumor cells thus diminishing the efficiency of cancer treatment (Figure 8) (72, 94).

Over the past decades, focus on tumor angiogenesis has had a large interest in cancer research. Identification of angiogenic factors has been addressed in targeted drug therapy (91, 95), providing beneficial outcomes particularly in combination with chemotherapy especially in patients with advanced lung adenocarcinoma (96, 97).

Remarkably, recent studies are evaluating the correlation of lipid metabolism and tumor angiogenesis. Seguin *et al.* observed a reduction of angiogenic and metastatic potency after inhibition of fatty acid synthase in melanoma (98).

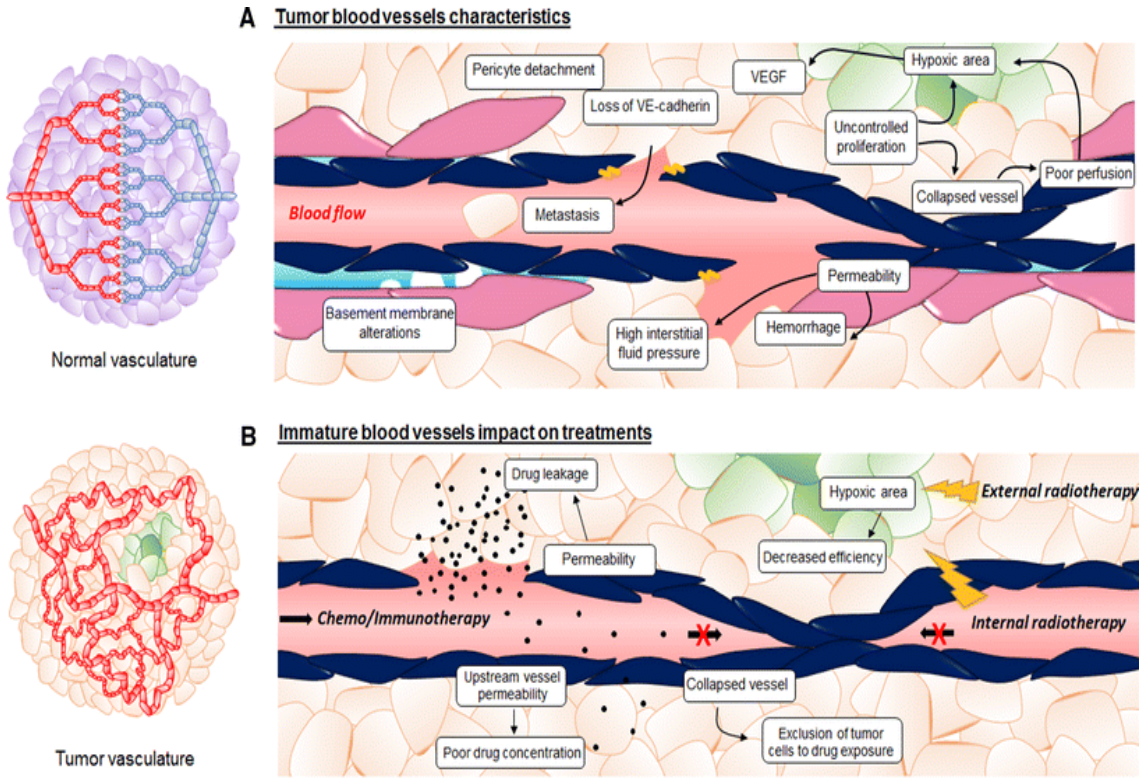

Figure 8. Structure and consequence of tumor vasculature. a) Contribution of structural abnormalities of tumor blood vessels in increased vascular permeability and decreased blood perfusion resulting hypoxic areas, hemorrhage and promoting metastasis. b) Functional irregularities of immature tumor blood vessels diminish the efficiency of cancer therapy (72).

1.7 Aim of Study

In the last decades, increasing studies are exploring the implication of lipogenesis on tumor biology, however, very few have approached the role of lipolysis and ATGL in tumorigenesis. In addition to that, the involvement of lipolysis on tumor angiogenesis is still under observation.

Recently in our group, we investigated the impact of ATGL-loss on the metabolic switch in the lung cancer cell line A549, cultivated in 2- and 3-dimensional (3D) cell culture (monolayer versus spheroids) (99, 100).

We could show an increased aggressive behavior of ATGL deficiency in A549 spheroids compared to A549 monolayers. 3D cultivated cells featured increased growth, attenuated apoptosis as well as enhancement of the glycolytic pathway (99).

In this context, the impact of hypoxia is the major question of my work. Therefore, the aim of this study was to investigate the impact of hypoxia on metabolic and angiogenic properties in ATGL-deficient A549 cell line.

Specific aim 1:

Does hypoxia cause alteration in the proteome composition of spheroids of A549 wildtype (WT) vs ATGL-knock out (KO) group?

Specific aim 2:

Does the loss of ATGL induce changes in the proteome composition of spheroids of ATGL cell line under normoxic vs hypoxic conditions?

Specific aim 3:

Does hypoxia induce angiogenesis in spheroids of A549 cell line (WT vs ATGL-KO)?

Specific aim 4:

Does ATGL deficiency influence the angiogenic properties of spheroid of A549 cell line under normoxic vs hypoxic environment?

Workplan:

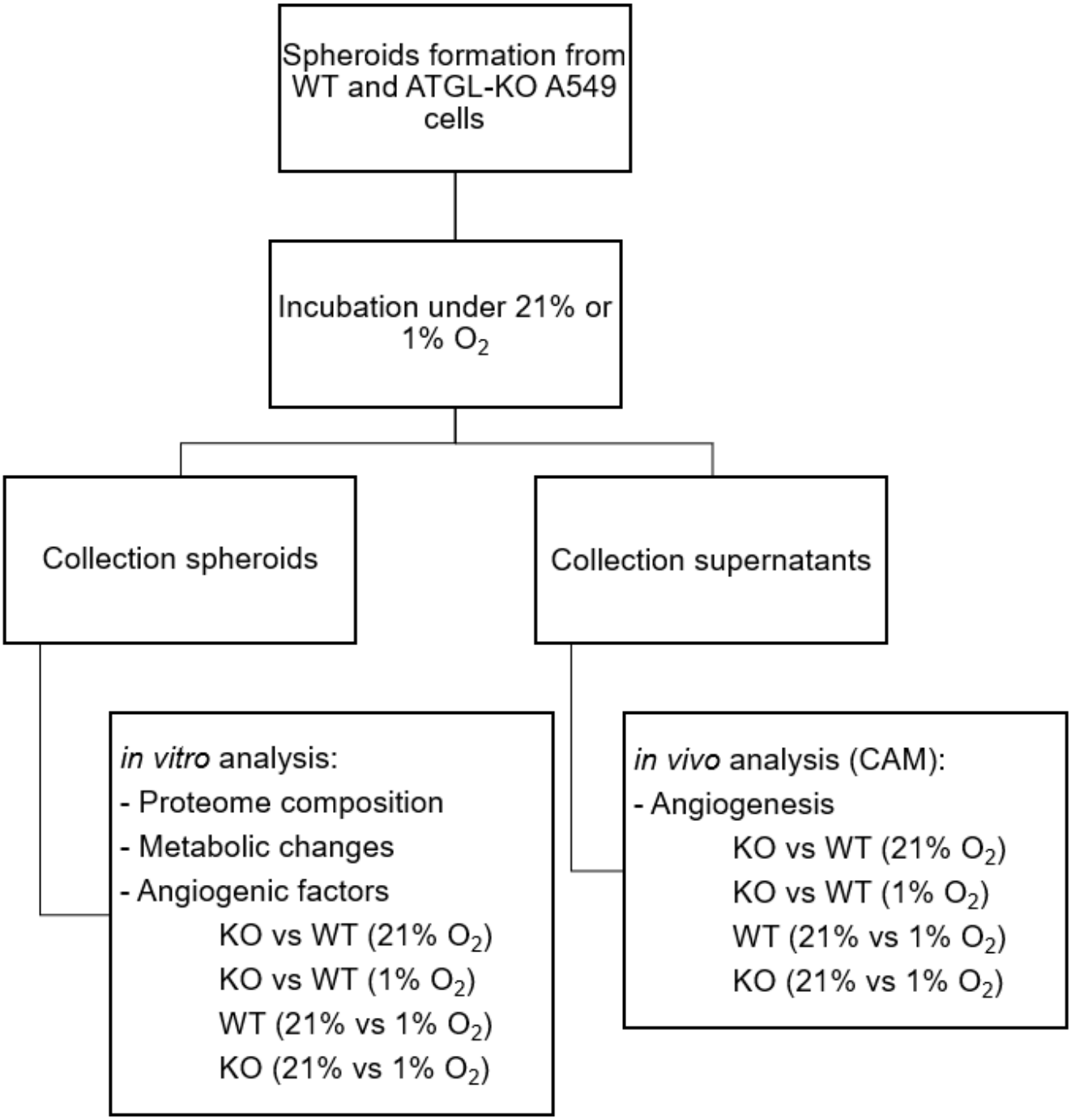
Spheroids formation from WT and ATGL-KO A549 cells
Incubation under 21% or 1% O_2
Collection spheroids
Collection supernatants
in vitro analysis:
- Proteome composition
- Metabolic changes
- Angiogenic factors
KO vs WT (21% O_2)
KO vs WT (1% O_2)
WT (21% vs 1% O_2)
KO (21% vs 1% O_2)
in vivo analysis (CAM):
- Angiogenesis
KO vs WT (21% O_2)
KO vs WT (1% O_2)
WT (21% vs 1% O_2)
KO (21% vs 1% O_2)

2 Materials and Methods

2.1 Cell Culture

For this experiment, lung adenocarcinoma cell line A549 was used. This cell line was obtained from the research group of Ruth Birner-Grünberger (Institute of Pathology, Medical University of Graz, Austria and Faculty of Technical Chemistry, Vienna University of Technology, Austria). The formation of the knockout group from A549 lung cancer cell line was done through deletion of ATGL-gene, PNPLA2, using CRISPR/Cas9 (19). The WT and ATGL-KO group of A549 cell line were cultivated in a medium composed of Rosswell Park Memorial Institute-1640 (RPMI-1640) (Sigma Aldrich, Austria) containing L-glutamine, sodium bicarbonate and phenol-red, 10% fetal bovine serum (FBS) (Gibco) and 1% penicillin/streptomycin antibiotics (P/S). They were cultivated under standard conditions at 37.5°C and 5% CO_2. Cell splitting was done twice a week.

The A549 cell line was first established back in 1971 by Giard *et al.* (101). These cells were acquired from human alveolar basal epithelial cells of lung adeno-carcinoma (101). They are characterized with epitheloid features with high levels of fatty acids and are able in *in vitro* cultivation to form a monolayer, adherently attached to the surface of the culture flask (101). They are widely used as well-established model in countless lung cancer studies (101).

2.2 Spheroids Formation and Hypoxic Incubation

For the *in vitro* and *in vivo* assay, 3D spheroids were created from WT and ATGL-KO A546 lung cancer cells using two ultra-low-adhesion 96-well microplates (Corning® Costar® Ultra-Low Attachment Multiple Well Plate). Each microplate carried 30 wells for A549-WT cells and 30 wells for the ATGL-KO group of A549 cell line with every well containing 10,000 cells in 100 µL of medium (RMPI + 10% FBS + 1% P/S). The microplates were centrifuged at 1200 rpm for 20 minutes at room temperature (RT). Afterwards, one microplate was incubated at 37.5°C under 21% O_2 and 5% CO_2 and the other one was cultivated at 37.5°C under 1% O_2 and 5% CO_2 each for 3 days. Centrifugation and incubation were carried out at the research laboratory of Ludwig Boltzmann Institute (LBI) supervised by the

research group of Andelko Hrzenjak (Division of Pulmonology, Department of Internal Medicine, Medical University of Graz, Austria).

One of the distinguishing features of the 3D cell culture model is providing a better resemblance to the *in situ* neoplastic microenvironment (102, 103). Similar to tumors *in situ,* gradients of oxygen and nutrients concentration are developed in the spheroids. This leads to formation a hypoxic core in the spheroids with limited nutrients availability (Figure 9), resulting in stimulation of angiogenesis (102, 103). Additionally, gene expression of 3D cell cultures preserve similarities to the genomic profile of the corresponding primary human tumor (103).

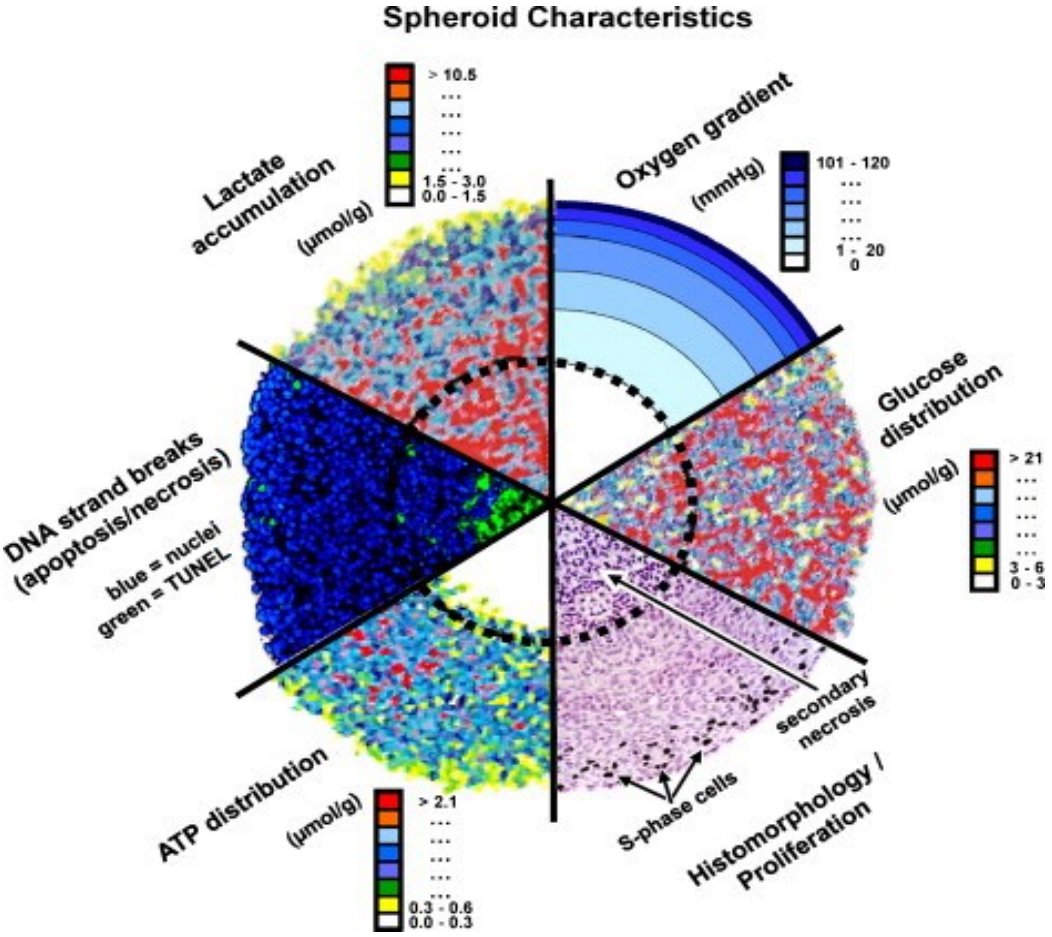

Figure 9. Overview of spheroids characteristics. Development of a decreasing concentration gradient of oxygen and nutrients gradient towards the core of the spheroids (103).

After 3 days of normoxic and hypoxic incubation, spheroids and supernatants of each group were collected separately, placed on ice and transported back to the laboratories at the Otto Loewi Research Center, Division of Immunology and Pathophysiology, Medical University of Graz. After centrifugation at 1200 rpm for 5

min at RT, spheroids were stored at -80°C, and were later used for the proteomic analysis, whereas the supernatants were directly used for the angiogenesis assay.

2.3 Proteomics Analysis

2.3.1 Proteomics sample preparation and analysis

Due to the extremely high content of proteins in the supernatants of each group of the A549 lung cancer cells, proteomics analysis was performed on the WT and ATGL-KO spheroids, cultivated under different oxygen levels. The whole experimental setup of the proteomic analysis (Figure 10) was taken place at the research laboratories of Center for Medical Research (ZMF), Graz, supervised by Tamara Tomin, a member of the research team of Ruth Birner-Grünberger (Institute of Pathology, Medical University of Graz, Austria and Faculty of Technical Chemistry, Vienna University of Technology, Austria).

Spheroids of each of the WT and ATGL-KO group, pre-incubated in hypoxia or normoxia, were well washed with phosphate-buffered saline (PBS) and then lysed in a lysis buffer composed of 100 mM Tris pH = 8, 1% sodium dodecyl sulfate (SDS), 10 mM tris(2-carboxyethyl)phosphine (TCEP), 40 mM chloroacetamide (CAA) in combination with several sonication cycles. Afterwards, the concentration of proteins in each sample were estimated colorimetric using bicinchoninic acid-reducing agent compatible (BCA-RAC) protein assay (Pierce™ BCA Protein Assay Kit, Thermo Scientific™, USA) and SPECTRAmax (Molecular Devices, USA), a microplate reader, at wavelength of 562 nm. Approximately 100 µg of protein of each sample was precipitated with acetone overnight, then re-dissolved in 25% trifluoroethanol (TFE) (in 100 mM Tris pH=8.5), diluted to 10% TFE with ammonium bicarbonate and digested with LysC (Thermo Scientific, USA) for 2 hours followed by overnight trypsin (Thermo Scientific, USA) treatment. Prior to measurement, further purification and desalting of the protein samples were achieved by using SDB-RPS STAGE tip, then the samples were diluted with running buffer A (0.1% formic acid, 5% acetonitrile; running buffer B was pure acetonitrile). 1µg of sample was used for liquid chromatography-tandem mass spectrometry (LC-MS/MS) analysis, which was performed during 2h by Ultimate 3000 RCS Nano Dionex system equipped with a Ionoptiks Aurora Series UHPLC

C18 column (250 mm x 75 µm, 1.6 µm) (Bruker Daltonics, Germany) coupled to a Orbitrap Velos Pro (Thermo Scientific, USA) operated in positive mode.
If not stated otherwise, all chemicals were purchased from Sigma Aldrich.

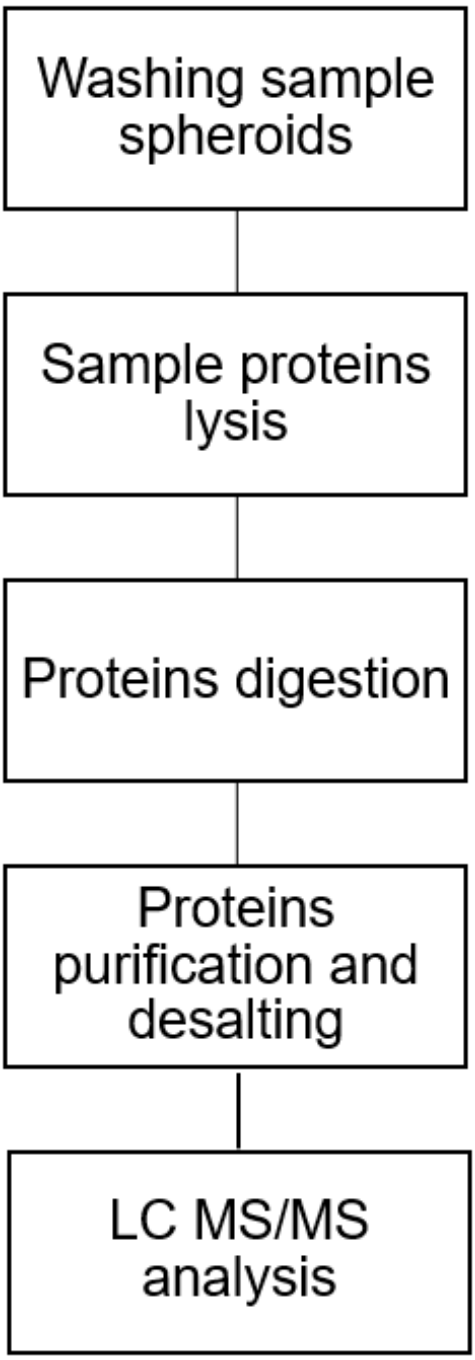

Figure 10. Summary of the proteomics sample preparation and analysis

2.3.2 Data and statistical analysis

Data analysis, database search and quantitation were carried out by MaxQuant (v1.6.1.0) software (104). SwissProt human fasta file was applied for database search, with false discovery rate (FDR) set to 1% and allowed number of trypsin miscleavages set to 2. Quantitation of proteins was based on label free quantitation (LFQ) approach, with minimum of 2 peptides per protein as quantitation requirement. Match between runs was enabled in the retention time window of 1 min (alignment window set to 20 min), allowing the software to match unidentified features between the runs.

A list of 2104 proteins with their corresponding LFQ values were identified by MaxQuant software, and this list was imported into Perseus (v1.6.5.0) (105) for statistical analysis. LFQ approach results in many missing values (proteins that did not fulfill 2 peptides requirement), therefore prior to statistical testing it was necessary to filter the matrix for proteins that had at least 3 valid values per group and impute remaining missing values from normal distribution. For this purpose, matrix was reduced to two sample types at the time (ATGL-WT vs KO in hypoxia, ATGL-WT vs KO in normoxia, ATGL-WT in normoxia vs ATGL-WT in hypoxia and ATGL-KO in normoxia vs ATGL-KO in hypoxia). Consequently, comparison of the reduced matrix sets was performed using student's *t*-test with the following criteria: p-value of at least 0.05, S0 of 0.1 and permutation-based FDR set to 5% or 1%. Interpretation, mapping and visualizing of protein-protein functional interaction of each group was provided from the online database STRING version 11 (106). Protein functions and their involvement in biological pathways were graphically presented using IBM SPSS Statistics version 25.

2.4 Angiogenesis CAM Assay

The angiogenic potential of each group of the A549 cell line was observed with an *ex ovo* CAM assay. The chorioallantoic membrane, a highly-vascularized membrane, is formed from fusion of the chorion with the allantois during chick embryogenesis and is histologically made of ectoderm, mesoderm and endoderm (Figure 11) (107-109). The vascular system of the CAM is normally fully developed at day 11 or 12 of incubation (109, 110), and is eminently sensitive to angiogenic molecules between days 8 and 10 of incubation (110). Avian embryos are natural immunodeficient, especially in the early stages of embryogenesis, which can prevent inflammation-induced angiogenesis (111).

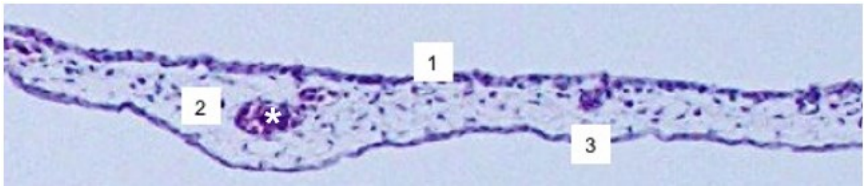

Figure 11. Micrograph of the chick embryo CAM tissue in cross section. The chorioallantoic membrane consist of 1) outer ectodermal chorionic layer, 2) intermediate mesodermal layer with stromal cells, collagen fibers and blood vessels [*] and 3) inner endodermal allantoic layer (99). *H&E stain.*

One the technical challenges of the CAM model system is the incapability of incubation of chick embryos under oxygen levels below 15% over 1-3 days (14, 15), therefore the supernatants of A549 spheroids, which were pre-incubated in hypoxia, were used instead of incubation of the cells on CAM under hypoxia.

Over the past decades, various reliable methods have been widely established regarding administration of testing factors onto the CAM (110). For this study, we used CAM collagen onplant model according to Deryugina and Quigley (110) and is summarized in Figure 13. With this model, distinguishing the angiogenic response from the pre-existing embryonic vasculature is achievable, providing a distinctive quantification of angiogenesis (110).

Fertilized white Lohmann chicken eggs (Schropper, Gloggnitz, Austria) were washed and incubated at 37.6°C and 60% humidity. After 3 days of incubation, the eggs were cracked, and the chick embryos were placed on a sterile dish and covered with square Petri dishes (Figure 12). In advance, the dishes were immersed with 75% ethanol and placed under ultraviolet (UV)-light (Light

Progress, Tuscany, Italy) for 16 min. Later, the *ex ovo* chick embryos were set back in the incubator (Incubator Easy200, J.Hemel Brutgeräte, Germany) at 37.6°C and 60% humidity. On day 10 of chick embryonic development, the angiogenic CAM assay was performed: the supernatants of all four conditions (normoxic WT, hypoxic WT, normoxic ATGL-KO and hypoxic ATGL-KO) were incorporated in the mastermix and then settled between two nylon grid meshes, forming a 3D graft (onplant). The mastermix was composed of 10X Minimum Essential Medium Eagle (MEM), type I rat tail collagen (Cornig), HEPES and sodium hydroxide. The preparation of the mastermix was done on ice, to prevent premature polymerization of the collagen (110). The nylon grids were then incubated at 37°C for 30 min allowing collagen polymerization, afterwards the grids were placed using forceps on the CAM (6 onplants/egg) (Figure 12). To provide enough data, 4-6 embryos each containing 6 onplants were used per group. Chick embryos with onplants were then incubated under the same conditions for another 3 days. On day 13 of chick embryonic development, newly formed blood vessels were counted manually with a stereomicroscope (Olympus, Japan) focusing on the upper grid with magnification of 6.3x and estimated with angiogenesis index (AI), which is the ratio of the number of squares with blood vessels over the total number of squares of each grid (110).

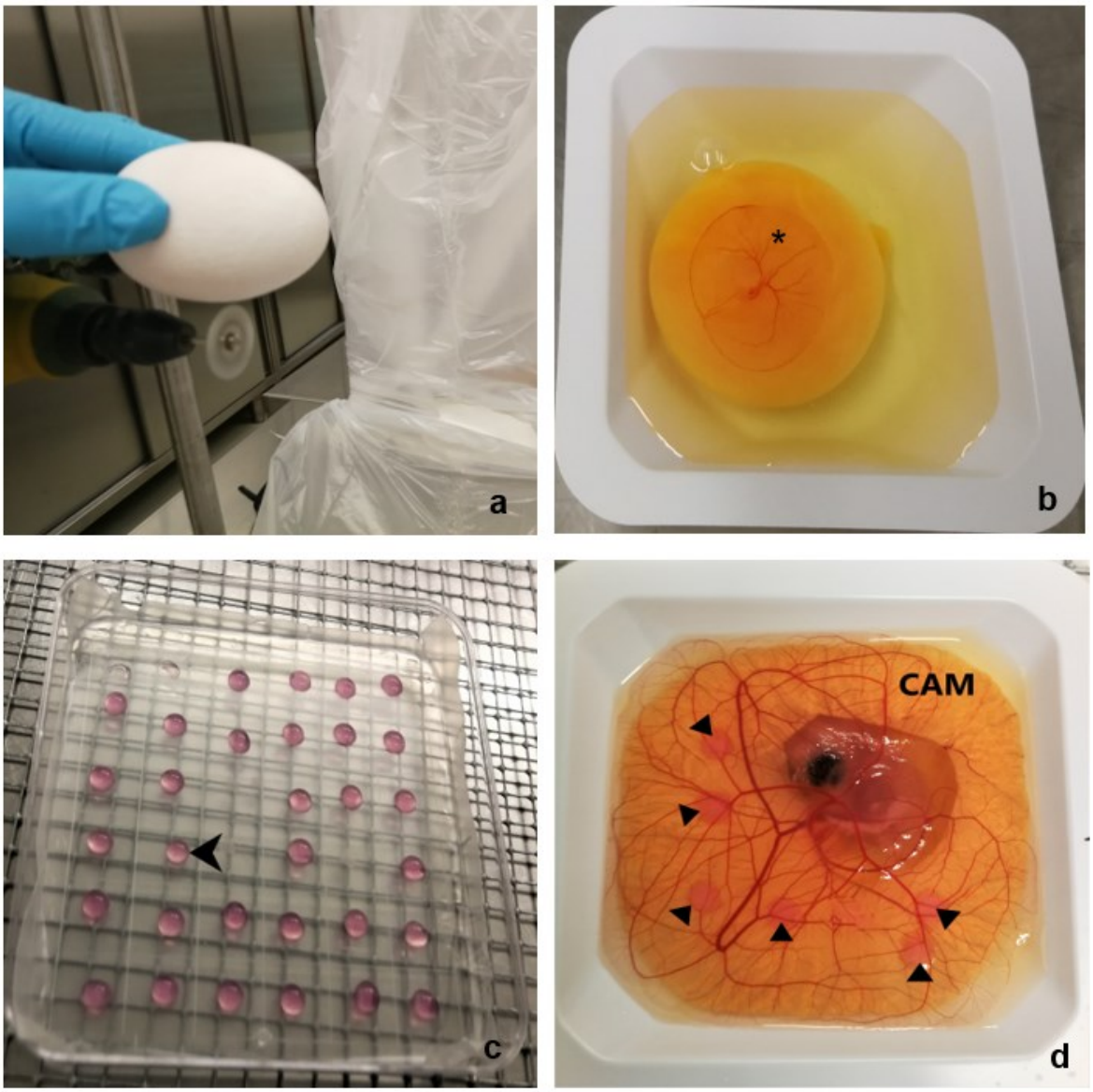

Figure 12. CAM collagen onplant assay. a) Cracking eggshell with a drill at day 3 of avian embryonic development. b) Chick embryo placed on a sterile dish, containing blood vessels from yolk membrane **[*]**. c) Onplants with collagen and supernatants **[➤]** of samples placed on a Petri dish. d) Transfer onplants **[▲]** on CAM at day 10 of embryonic development (6 grids/egg).

2.4.1 Statistical analysis

Data collection and entry was done with Microsoft Excel Office 365. Calculation of AI and mean and standard error (SE) of the AI, as well as graphing the data were carried out with the statistical software IBM SPSS Statistics version 25. Comparison of the independent samples was performed with Student's *t*-test.

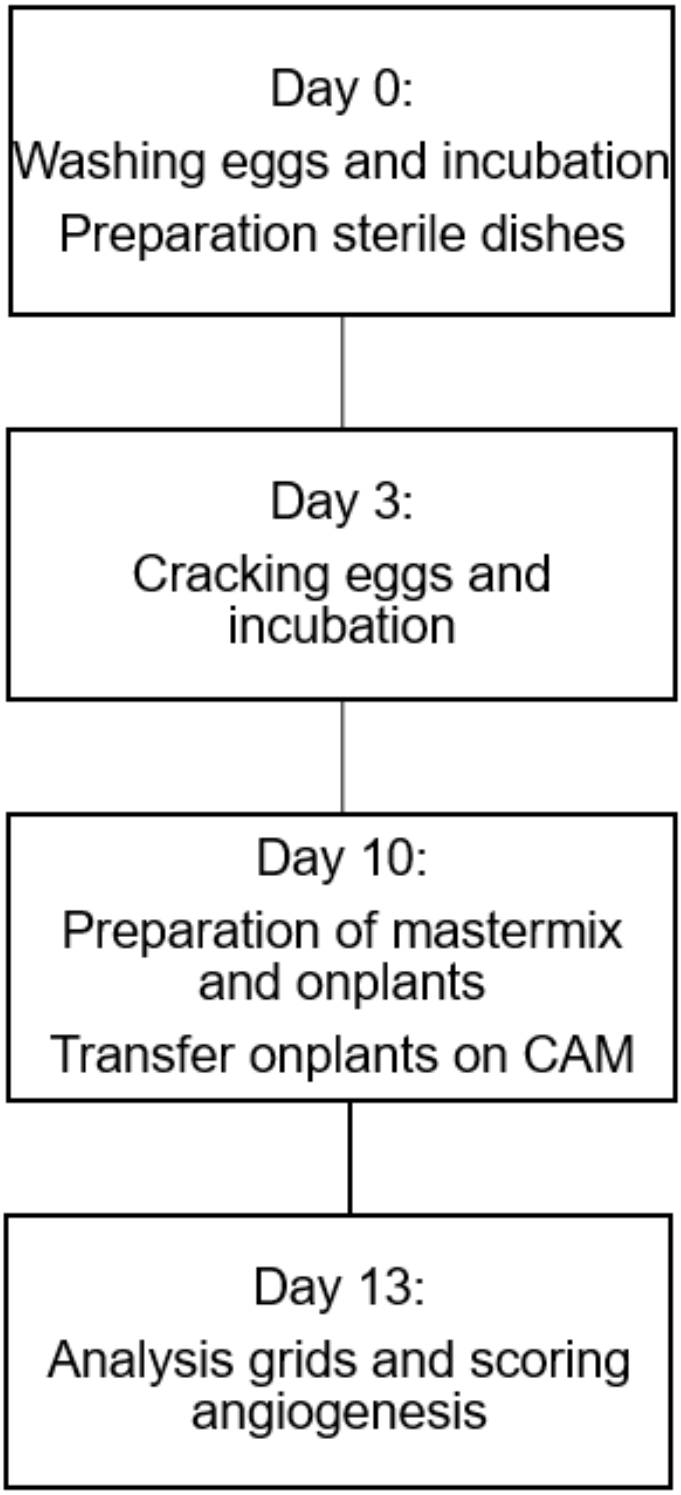

Figure 13. Summary of the angiogenesis CAM assay

3 Results

3.1 Proteomics Analysis

The normoxic and hypoxic pre-incubation and collection of A549 WT and ATGL-KO spheroids were repeated four times. In each replicate, 30 spheroids per group were collected and pooled in 16 samples for proteomics analysis.

All significantly differentially expressed proteins between the A549-WT and A549 ATGL-KO spheroids cultivated under particular oxygen levels (21% vs 1%) are listed in Supplementary table 1, Supplementary table 2 and Supplementary table 3 (see appendix).

Mapping of the protein-protein interactions in each group was done with the database STRING version 11 (106). Images to the protein networks of each group are found at the end of the thesis under appendix as well (Supplementary figure 7, Supplementary figure 8, Supplementary figure 9, Supplementary figure 10)

3.1.1 ATGL loss promotes aerobic glycolysis and macromolecular biosynthesis in normoxia

The label free quantification revealed a larger significant difference in the proteome composition between WT and ATGL-KO cells under normoxia (Figure 14) than under hypoxia (Figure 16).

Thirty-two proteins were significantly upregulated in the ATGL-KO group under normoxia and are listed in Supplementary table 2. Analysis of the potential protein-protein interactions of the significantly more abundant proteins using STRING database (106), revealed that several prominent upregulation of proteins in the normoxic ATGL-KO cells participate in the glycolytic pathway, particularly, fructose-bisphosphate aldolase C (ALDOC), ATP-dependent 6-phosphofructo-kinase (PFKP), alpha-enolase (ENO1) and pyruvate kinase (PKM) (17) (Table 1). This is further corroborated by gene ontology (GO) enrichment analysis of biological processes (GOBP) with proteins more expressed in the ATGL-KO as the input (Figure 15). In addition to core glycolytic enzymes, alteration in the lipid metabolism resulting from the absence of ATGL was also observed. High levels of ATP-citrate synthase (ACLY) was seen in the ATGL-KO group, which catalyzes the synthesis of cytosolic acetyl-CoA, a precursor in the *de novo* fatty acid

biosynthesis (35). Another identified protein in the ATGL-KO group was the annexin A2 (ANXA2), which inhibits the lysosomal degradation of low density lipoprotein (LDL) receptors by inactivating proprotein convertase subtilisin/kexin type 9 (PSCK9), therefore increasing the cellular uptake of lipids (112). Both proteins could imply an increase of lipogenesis and lipid droplet formation.

Furthermore, higher levels of factors catalyzing protein synthesis were found in the ATGL-KO spheroids, such as 40S ribosomal protein S15 (RPS15) (113), 40S ribosomal protein S17 (RPS17) (113) and complement component 1 Q subcomponent-binding protein (C1QBP) (114), as well as translation initiation proteins such as eukaryotic translation initiation factor 3 subunit A (EIF3A) (115) (Table 1), altogether indicating an increased protein production and cellular growth.

According to the UniProt database (116), six of the upregulated proteins in the normoxic ATGL-KO cells were characterized as secretory proteins present in the ECM, including programmed cell death protein 5 (PDCD5), CD166 antigen (ALCAM), C1QBP, ALDOC, peptidyl-prolyl cis-trans isomerase A (PPIA) and ANXA2. All these proteins, excluding ALCAM, do not participate in tumor angiogenesis. It has been reported, that ALCAM could induce angiogenesis by activation of proteolytic enzyme MMP (117). In addition to ALCAM, another proangiogenic factor was found expressed in the ATGL-KO group under 21% O_2, namely, reticulon-4 (RTN4), which regulates angiogenesis positively by chemotaxis and migration of the ECs (118).

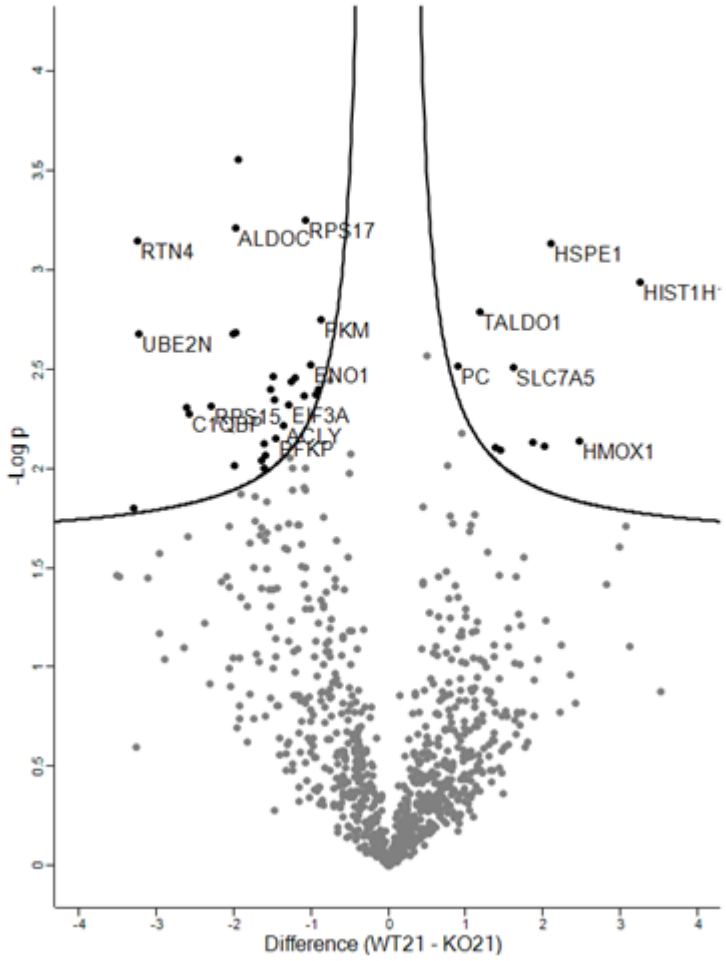

Figure 14. Volcano plot of LFQ proteomics screening of A549 ATGL-KO and WT spheroids in normoxia. Significant change in the protein composition in A549 cells cultivated in 21% oxygen as a result of ATGL loss. Upregulation of specific proteins in the ATGL-KO group are shown on the left upper side of the diagram (dark dots above the curve line, left) and on the right side higher expression levels of proteins in WT group (dark dots above the curve line, right).

Protein ID	Protein name	Gene name	Fold Change WT 21% to KO 21%
Q9NQC3	Reticulon-4	RTN4	0,104896471
Q13740	CD166 antigen	ALCAM	0,163286747
Q07021	Complement component 1 Q subcomponent-binding protein	C1QBP	0,166509338
P62841	40S ribosomal protein S15	RPS15	0,202464877
O14737	Programmed cell death protein 5	PDCD5	0,249976961
P09972	**Fructose-bisphosphate aldolase C**	**ALDOC**	**0,254148277**
P62937	Peptidyl-prolyl cis-trans isomerase A	PPIA	0,330906651
Q01813	**ATP-dependent 6-phosphofructokinase**	**PFKP**	**0,364585439**
P53396	ATP-citrate synthase	ACLY	0,387974698
Q14152	Eukaryotic translation initiation factor 3 subunit A	EIF3A	0,406655767
P08708	40S ribosomal protein S17	RPS17	0,471351125
P06733	**Alpha-enolase**	**ENO1**	**0,495313701**
P07355	Annexin A2	ANXA2	0,532440494
P14618	**Pyruvate kinase PKM**	**PKM**	**0,543196443**

Table 1. List of expressed proteins in the ATGL-KO group versus WT in 21% O_2 from the LFQ analysis. Fold change values less than one indicate overexpression of proteins in ATGL-KO cells, among those proteins involved in glycolysis (bald gene names).

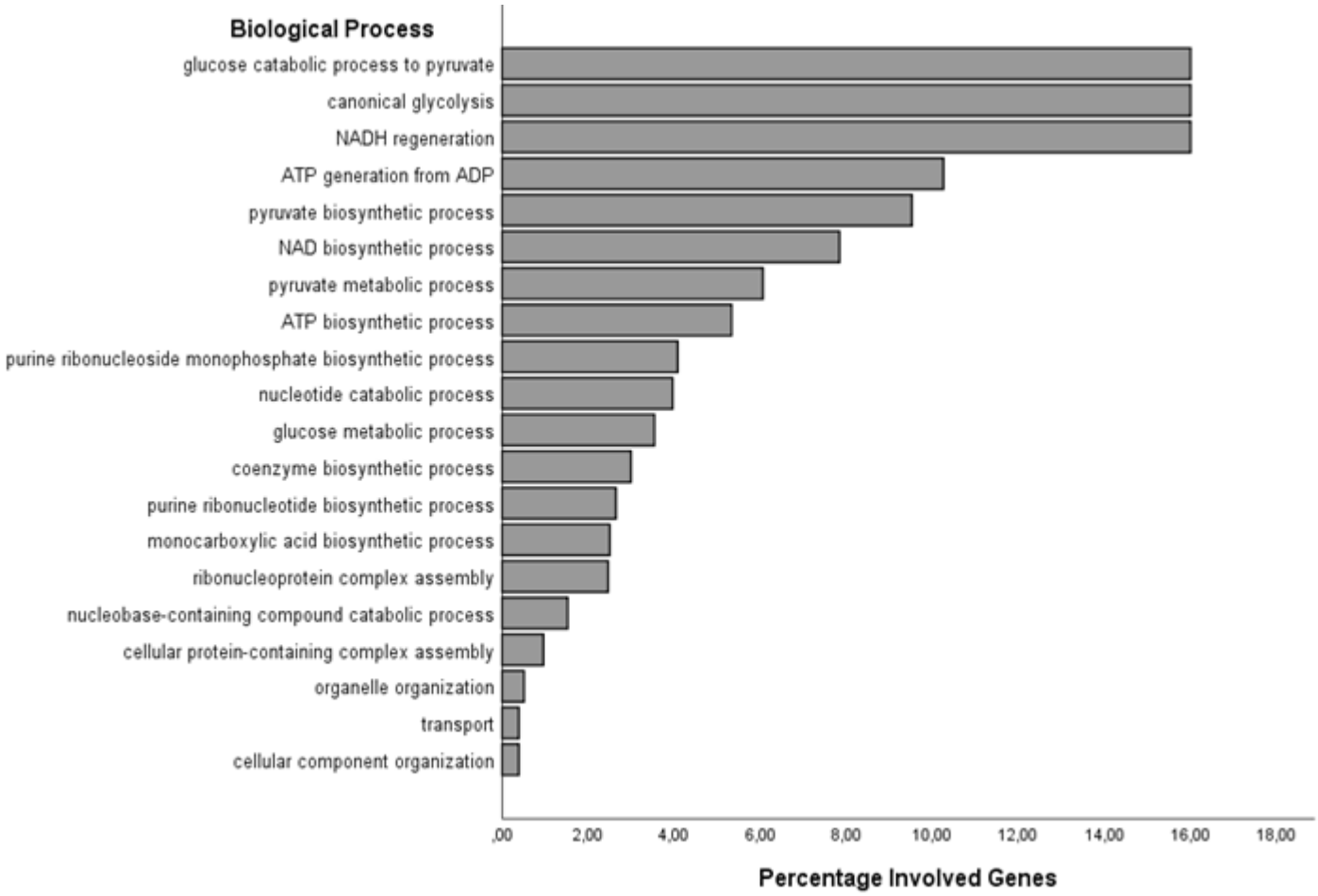

Figure 15. Significantly enriched biological processes in normoxic A549 ATGL-KO group. This figure presents the major biological processes, which the upregulated proteins in ATGL-KO group under normoxia compared to normoxic WT group are engaged. Carbohydrate metabolism especially glycolysis is highly enriched in the ATGL-KO group.

3.1.2 Proteomic alteration in A549 WT group vs ATGL-KO group under normoxia

Our analysis revealed significant expression of 10 proteins in the A549 WT spheroids versus the ATGL-KO cells, pre-incubated under normoxia and are listed in Table 2 and Figure 14. Interestingly, some of the overexpressed proteins in the normoxic WT cells were featured with proliferative and metastatic effect among those pyruvate carboxylase (PC) (119), heme oxygenase 1 (HMOX1) (120, 121) and large neutral amino acids transporter small subunit 1 (SLC7A5) (122-124). Furthermore, the LFQ analysis also displayed high levels of the protein Ras GTPase-activating-like protein IQGAP2 (IQGAP2), which has been reported to be linked to better cancer survival rates in patients with lung cancer (125).

The relationship of the proteins SLC7A5, a sodium-independent amino acid transporter and PC with neoplastic development was seen through regulating many anaplerotic reactions in tumor cells, particularly biogenesis of macromolecules (119, 126). Further to mention is the involvement of HMOX1 in tumor angiogenesis, as it is predicted as a potential proangiogenic factor. However, its mechanism is still unclear, as studies stated that HMOX1 may promote synthesis of VEGF and improve cellular sensibility to VEGF (65, 121, 127).

Protein ID	Protein name	Gene name	Fold Change WT 21% to KO 21%
P11498	Pyruvate carboxylase	PC	1,858139416
P37837	Transaldolase	TALDO1	2,254208205
Q13576	Ras GTPase-activating-like protein IQGAP2	IQGAP2	2,586294501
Q13045	Protein flightless-1 homolog	FLII	2,705999994
Q01650	Large neutral amino acids transporter small subunit 1	SLC7A5	3,043977776
P13533	Myosin-6	MYH6	3,645857224
Q9GZR7	ATP-dependent RNA helicase DDX24	DDX24	4,01330915
P61604	10 kDa heat shock protein	HSPE1	4,292311636
P09601	Heme oxygenase 1	HMOX1	5,513140973
P16401	Histone H1.5	HIST1H1B	9,514048935

Table 2. List of expressed proteins in the WT spheroids vs ATGL-KO in normoxia from the LFQ analysis. Fold change values higher than one imply upregulation of proteins in the WT group.

3.1.3 Minor changes in the protein profile between ATGL-KO and WT cells under anaerobic atmosphere

Overexpression of only four proteins was seen in the ATGL-KO spheroids compared to WT spheroids cultivated in hypoxia, namely high mobility group protein B3 (HMGB3), transmembrane emp24 domain-containing protein 2 (TMED2), translocon-associated protein subunit delta (SSR4) and solute carrier family 2, facilitated glucose transporter member 1 (GLUT1, SLC2A1) (Figure 16, Table **3**).

In this regard, glucose transporter GLUT1 and DNA binding protein HMGB3 are found to be involved in tumor invasion and metastasis and are linked to low survival rates in patients with lung cancers (128, 129).

In addition, higher GLUT1 expression indicates an increase in glucose metabolism (128) in the ATGL-KO under 1% O_2, as observed for normoxia.

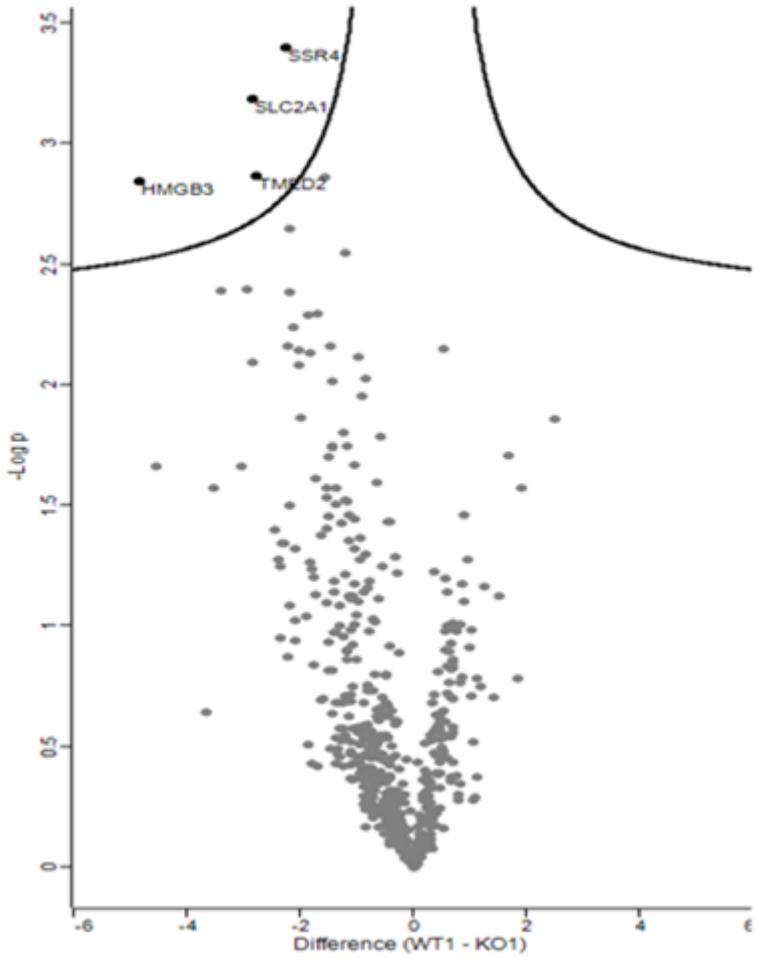

Figure 16. Volcano plot of LFQ proteomics screening of A549 ATGL-KO and WT cells in hypoxia. As shown on the left upper side, above the curve line, four specific proteins (SSR4, SLC2A1, TMED2, HMGB3) were significantly expressed in the ATGL-KO group versus WT group.

Protein ID	Protein name	Gene name	Fold Change WT 1% to KO 1%
O15347	High mobility group protein B3	HMGB3	0,0349964
P11166	Solute carrier family 2, facilitated glucose transporter member 1	SLC2A1	0,1378354
P51571	Translocon-associated protein subunit delta	SSR4	0,206441
Q15363	Transmembrane emp24 domain-containing protein 2	TMED2	0,1443175

Table 3. List of expressed proteins in the ATGL-KO group compared to WT under hypoxia from the LFQ analysis. Fold change values less than one point out upregulation of the proteins in the hypoxic ATGL-KO group.

3.1.4 A549 WT but not ATGL-KO spheroids have decreased protein translation under hypoxia compared to normoxia

Interestingly, changes in oxygen concentration affected the A549 WT-cells to a different extent. Significant upregulation of over 100 proteins in the WT under normoxia versus 32 proteins under hypoxia was revealed in the LFQ analysis (Supplementary table 1, Figure 17).

After retrieving functions of the expressed proteins with (GO) enrichment analysis of biological processes obtained from STRING database (106) and Uniprot database (116), numerous of the upregulated proteins in the normoxic WT group cells appeared to contribute in protein translation and synthesis. Among those were ribosomal proteins such as 40S ribosomal protein S11 (RPS11), 40S ribosomal protein S13 (RPS13), 40S ribosomal protein S14 (RPS14), 40S ribosomal protein S19 (RPS19), 40S ribosomal protein S21 (RPS21), 60S ribosomal protein L3 (RPL3), 60S ribosomal protein L21 (RPL21), 60S ribosomal protein L26 (RPL26), 60S ribosomal protein L28 (RPL28), as well as initiation translational proteins including eukaryotic translation initiation factor 3 subunit E (EIF3E), eukaryotic translation initiation factor 3 subunit (EIF3I), eukaryotic translation initiation factor 4B (EIF4B) and elongation factor 1-alpha 1 (EEF1A1) (Table 4, Figure 18). When protein profiles from ATGL-KO spheroids cultured under 21% to 1% O_2 were compared, no significant difference was observed (Supplementary figure 1).

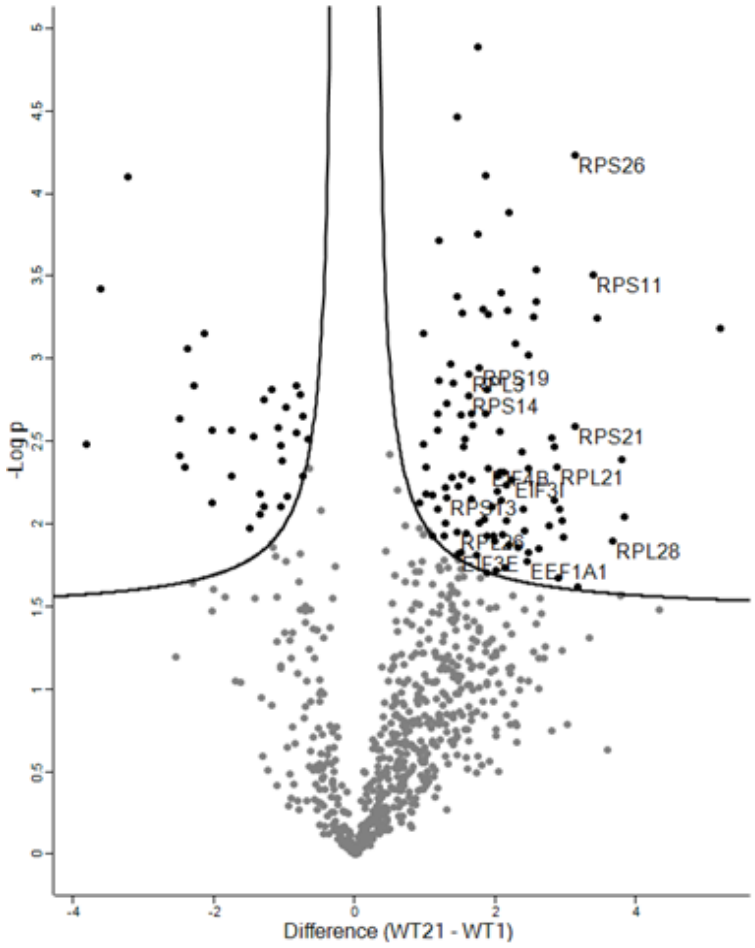

Figure 17. Volcano plot of LFQ proteomics screening of A549 WT cells in normoxia vs in hypoxia. On the left side, black dots above the curve shows the significant overexpression of proteins in the hypoxic WT group and on the right side upregulation of proteins in normoxic WT group.

Protein ID	Protein name	Gene name	Fold Change WT 21% to WT 1%
O60832	H/ACA ribonucleoprotein complex subunit 4	DKC1	2,020459461
P38919	Eukaryotic initiation factor 4A-III	EIF4A3	2,152307061
P62277	40S ribosomal protein S13	RPS13	2,459899275
P61254	60S ribosomal protein L26	RPL26	2,714671183
P60228	Eukaryotic translation initiation factor 3 subunit E	EIF3E	2,749597129
O60841	Eukaryotic translation initiation factor 5B	EIF5B	2,88358427
P62263	40S ribosomal protein S14	RPS14	3,071827902
P39023	60S ribosomal protein L3	RPL3	3,076348613
P39019	40S ribosomal protein S19	RPS19	3,391846717
P23588	Eukaryotic translation initiation factor 4B	EIF4B	3,691250117
Q15046	Lysine--tRNA ligase	KARS	4,211180722
Q13347	Eukaryotic translation initiation factor 3 subunit I	EIF3I	4,666715956
P62917	60S ribosomal protein L8	RPL8	5,290600839
P68104	Elongation factor 1-alpha 1	EEF1A1	5,440520414
Q14978	Nucleolar and coiled-body phosphoprotein 1	NOLC1	5,522234836
Q969Q0	60S ribosomal protein L36a-like	RPL36AL	6,926534159
P46778	60S ribosomal protein L21	RPL21	7,272359801
P62854	40S ribosomal protein S26	RPS26	8,708656644
P63220	40S ribosomal protein S21	RPS21	8,733896162
P62280	40S ribosomal protein S11	RPS11	10,47622689
P46779	60S ribosomal protein L28	RPL28	12,68915841
Q02878	60S ribosomal protein L6	RPL6	14,21317729

Table 4. List of some of the expressed proteins in the WT group, normoxia vs hypoxia from the LFQ analysis. The listed proteins are involved in protein translation and biosynthesis in the normoxic WT spheroids.

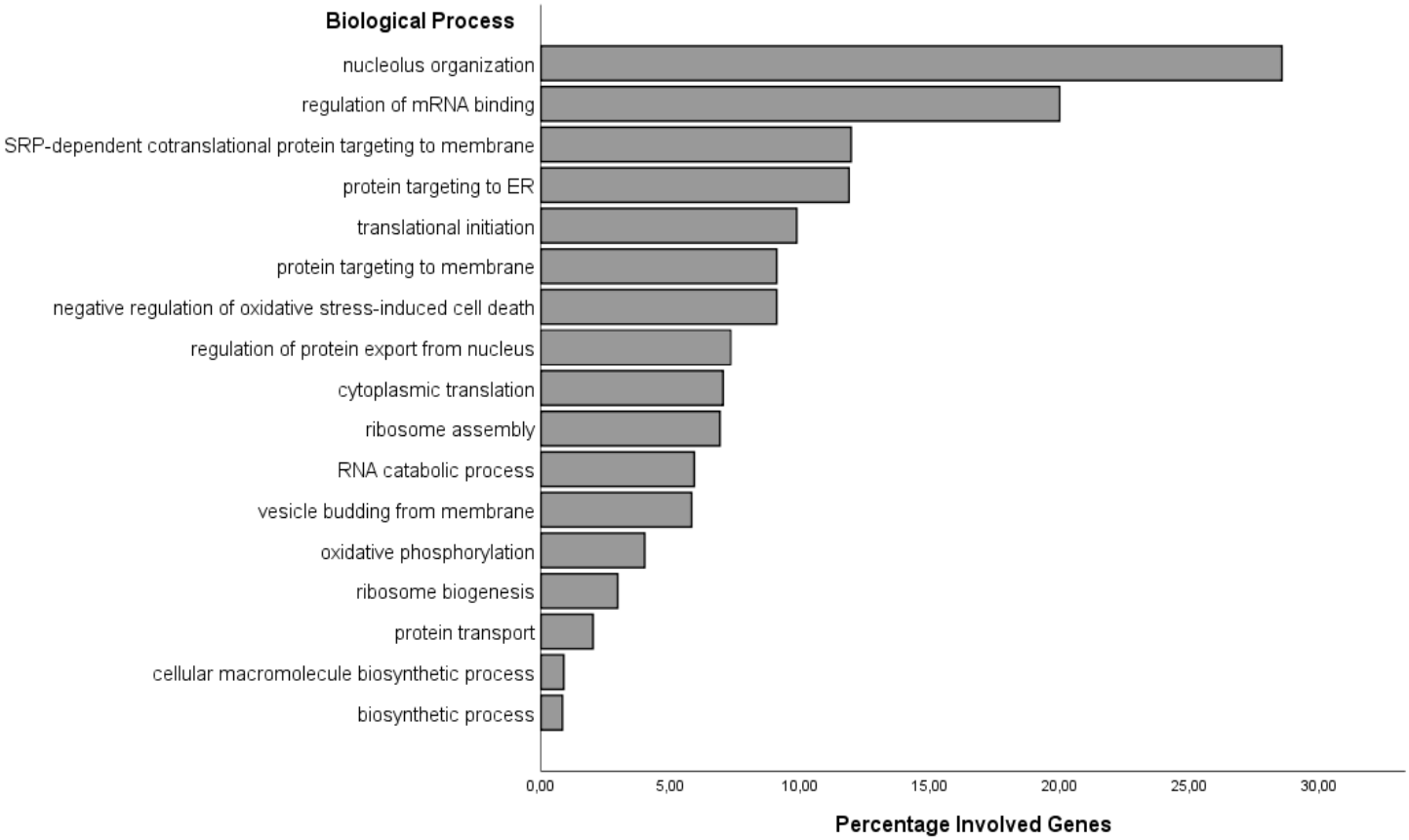

Figure 18. Significantly enriched biological processes performed by the upregulated proteins in the A549-WT group under 21% vs 1% O_2. Protein metabolism is highly enriched in the normoxic WT group.

3.1.5 A549 WT spheroids but not ATGL-KO seem to try to preserve mitochondrial activity under hypoxic conditions

From the LFQ analysis and functional analysis of proteins with enriched analysis of GOBP and UniProt database (116), high levels of a total of 10 mitochondrial proteins were presented in the hypoxic WT spheroids versus the normoxic WT cells. Those were cytochrome c oxidase subunit 2 (MT-CO2), complement component 1 Q subcomponent-binding protein (C1QBP), enoyl-CoA delta isomerase 1 (ECI1), mitochondrial import inner membrane translocase subunit Tim13 (TIMM13), ATP synthase subunit beta (ATP5B), citrate synthase (CS), malate dehydrogenase (MDH2), voltage-dependent anion-selective channel protein 1 (VDAC1), sideroflexin-1 (SFXN1) and 39S ribosomal protein L12 (MRPL12) (Table 5). Further to mention, MT-CO2, CS and MDH2 are enzymes of the aerobic cellular respiration. It is noteworthy to mention that many proteins of the oxidative phosphorylation was also found in high levels upon the normoxic WT spheroids including cytochrome c oxidase subunit 5A (COX5A), ATP synthase-coupling factor 6 (ATP5J), cytochrome b-c1 complex subunit 1 (UQCRC1) and ATP synthase subunit delta (ATP5D).

Interestingly, this does not seem to be the case for the ATGL-KO cells, as there was no difference observed in the protein profile under hypoxia versus normoxia (Supplementary figure 1, see appendix).

Protein ID	Protein name	Gene name	Fold Change WT 21% to WT 1%
P00403	**Cytochrome c oxidase subunit 2**	**MT-CO2**	**0,070942388**
Q07021	Complement component 1 Q subcomponent-binding protein	C1QBP	0,081220132
P42126	Enoyl-CoA delta isomerase 1	ECI1	0,17617855
P02751	Fibronectin	FN1	0,243357512
Q9Y5L4	Mitochondrial import inner membrane translocase subunit Tim13	TIMM13	0,295348193
P06576	ATP synthase subunit beta	ATP5B	0,368624671
O75390	**Citrate synthase**	**CS**	**0,393379479**
P52815	39S ribosomal protein L12	MRPL12	0,477429975
Q9H9B4	Sideroflexin-1	SFXN1	0,502273833
P08195	4F2 cell-surface antigen heavy chain	SLC3A2	0,558547751
P21796	Voltage-dependent anion-selective channel protein 1	VDAC1	0,560605876
P40926	**Malate dehydrogenase**	**MDH2**	**0,58216252**
P05387	60S acidic ribosomal protein P2	RPLP2	0,62626355

Table 5. Summarize of some of the significantly upregulated proteins in the A549-WT spheroids incubated under 1% O_2. Proteins engaged in the TCA and oxidative phosphorylation are written in bold.

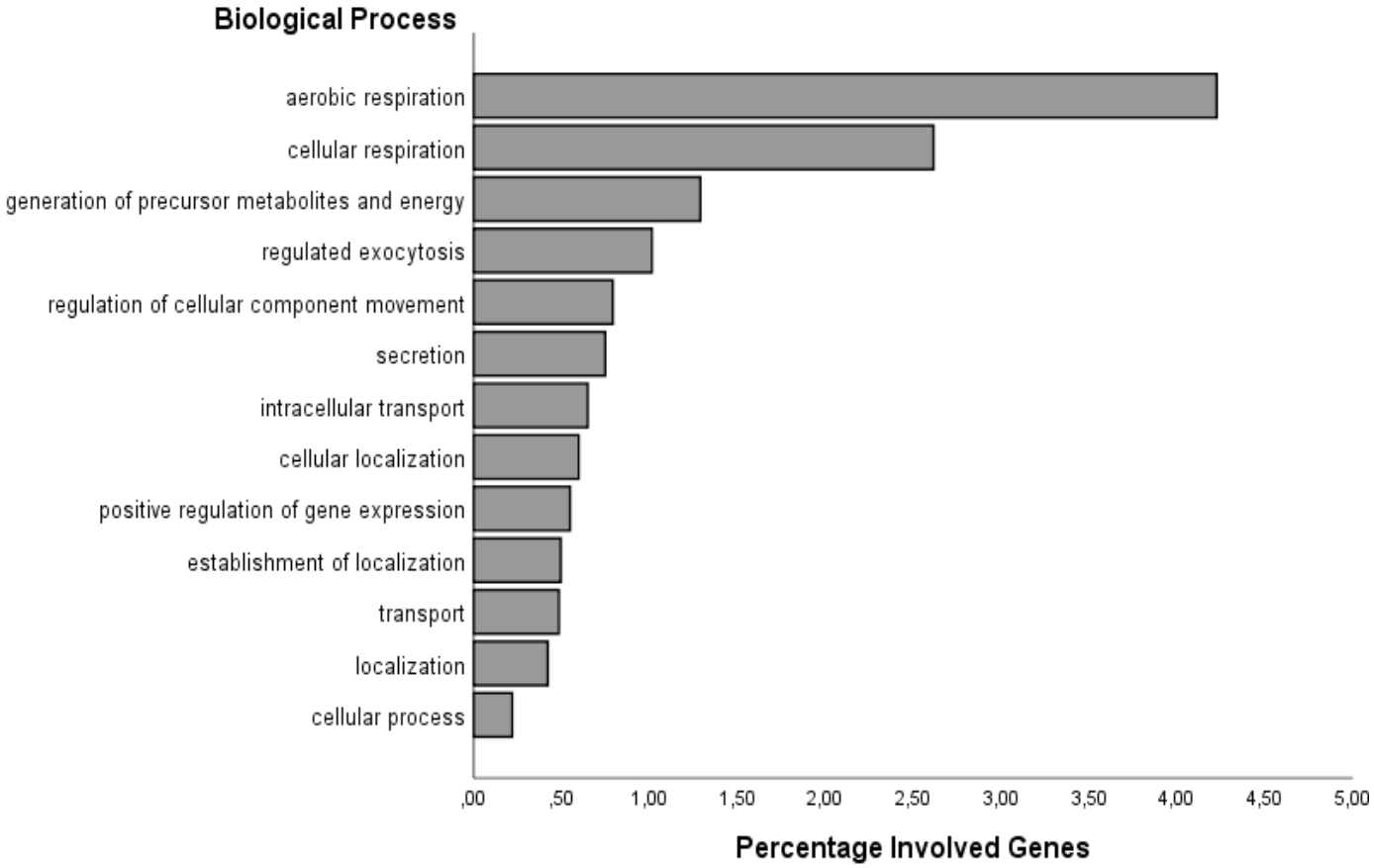

Figure 19. Enriched biological processes significantly performed by the upregulated proteins in the hypoxic A549-WT group compared to normoxic WT group.

3.1.6 Metabolic phenotype of ATGL-KO demonstrates similar phenotype under hypoxia

What was also interesting in the LFQ proteomics, was the expression of high levels of proteins in the ATGL-KO that are usually upregulated under hypoxia through the activation of HIFs. Among those were high levels of glycolytic enzymes and PPIA, a protein involved in protein folding (23, 130), these were seen in the ATGL-KO cells under 21% O_2. In addition, some proteins were found in abundance in both the normoxic ATGL-KO and hypoxic WT cells including RTN4, C1QBP and TMED10. This is further corroborated in the absent difference in the proteome composition in the ATGL-KO spheroids under normoxia versus hypoxia (Supplementary figure 1, see appendix). Altogether, this could indicate that the phenotype of ATGL-KO cells shares a high degree of similarity to the hypoxic phenotype.

3.2 Angiogenesis CAM Assay

This experimental setup was repeated four times, however one experiment was unfortunately not evaluable, as many chick embryos died before and during the assay and were not included into the analysis.

Died chick embryos during the experiments were removed and not evaluated. In addition, non-visible grids due to excessive polymerization of collagen, onplants containing only one grid or grids found upwards on the Petri dish covers were also excluded (Figure 20). The edges of the grids with squares surrounded by 3 borders were also not considered in counting.

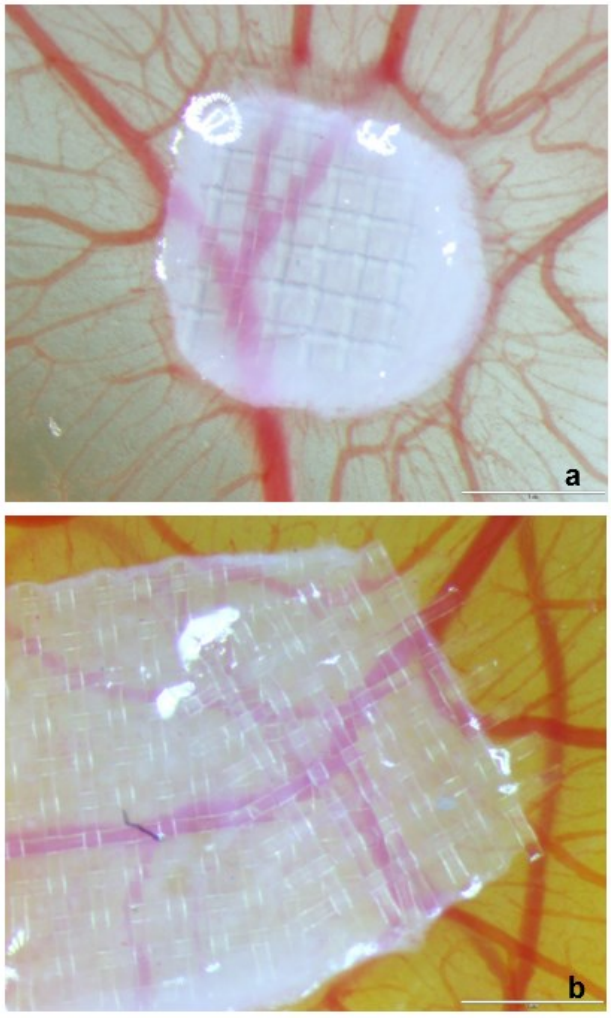

Figure 20. Micrographs showing examples of grids not valuable in scoring angiogenesis. a) Onplant contains only one nylon grid b) Upper grid lies at the side of the lower grid, not above it.

At the end, 77 out of 90 onplants for normoxic WT group, 65 out of 96 onplants for normoxic ATGL-KO group, 74 of 96 onplants for hypoxic WT group and 72 of 102 onplants for hypoxic ATGL-KO group were examined.

As mentioned above, newly formed blood vessels were counted with a stereomicroscope focusing on the upper grid with magnification of 6.3x and quantified with angiogenesis index (AI), which is the ratio of the number of squares with blood vessels over the total number of squares of each grid (Figure 21) (110). All angiogenesis values are presented as mean ± SE of AI. *P* values under 0.05 between the data sets were considered statistically significant.

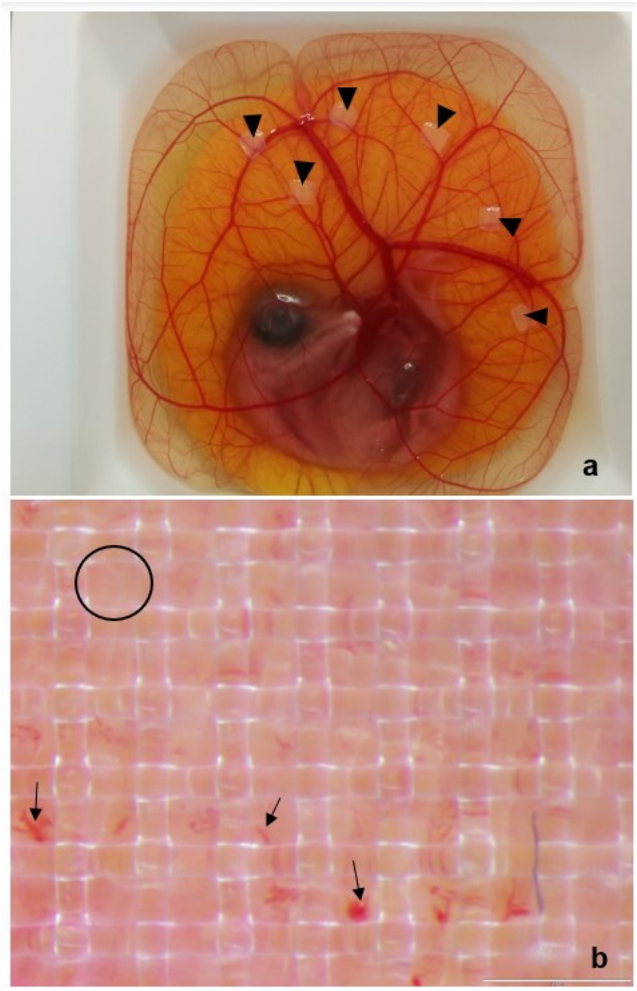

Figure 21.: Scoring angiogenesis. a) Chick embryo on day 13 of embryonic development with onplants [▲] on the CAM. b) Microscopic view of a grid at magnification of 4x. Arrows show squares with newly formed blood vessels. Not vasculated square marked with a circle.

3.2.1 Induced angiogenesis in the A549 WT group versus ATGL-KO group in normoxia but not in hypoxia

Angiogenic changes were only observed as significant when comparing the A549-WT group to the ATGL-KO group under normoxic conditions. An elevated neovascularization was identified in the WT group with an angiogenic index mean

of 0.38 ± 0.03 in comparison to ATGL-KO group (0.29 ± 0.03) under atmospheric oxygen levels (p = 0.018) (Figure 22).

Under hypoxic conditions, there was no statistically significant difference between the WT and ATGL-KO groups (0.35 ± 0.03 vs. 0.3 ± 0.02) with a p-value of 0.179.

3.2.2 Hypoxia-induced angiogenesis was not observed

Hypoxia-induced angiogenesis was not observed in this study. No angiogenic difference was shown between normoxic and hypoxic WT groups (0.38 ± 0.03 vs 0.35 ± 0.03) (p = 0.440). The same was true for the ATGL-KO group (0.29 ± 0.03 vs. 0.3 ± 0.02 in 21% vs 1% O_2 respectively) (p = 0.820).

All data are presented in a bar graph (Figure 22).

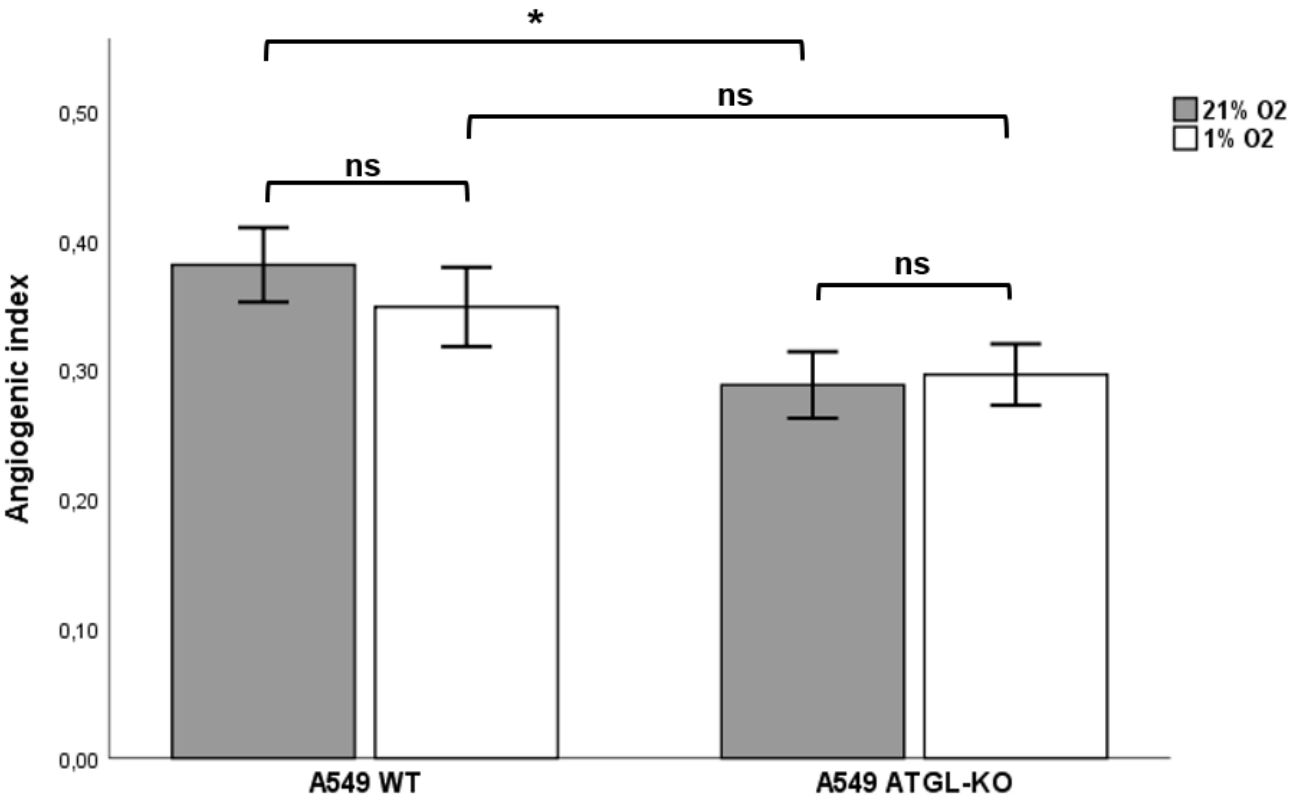

Figure 22. Comparison the angiogenic properties of A549 WT and A549 ATGL-KO groups under normoxic and hypoxic conditions. Quantification angiogenesis via the angiogenic index from the CAM angiogenesis assay using supernatants of A549-WT and ATGL-KO spheroids, which were pre-incubated for 3 days in normoxia or hypoxia. A significant increase of angiogenesis was only observed in the WT group to the ATGL-KO group under 21% O_2. Diagram presents mean of angiogenic index ± SE.* *p < 0.05; ns non-significance.*

4 Discussion

Angiogenesis and adjustment in metabolism are well-known hallmarks of cancer, which result from the rapid growth of tumor cells and the hypoxic microenvironment (9). ATGL, a key enzyme for hydrolysis of TAG, was found deficient in 38% of patients with lung cancer (18). The loss of ATGL was reported to be linked with tumor growth, aggressive behavior, metabolic reprogramming and low survival rate (18, 19, 99, 100). Further on, ATGL was found in reduced levels under hypoxia through activation of HIF-1 (20). In this study, we wanted to investigate the impact of hypoxia on the metabolism and angiogenic properties in ATGL deficient A549 cell line, cultivated in 3D cell cultures to obtain a better mimicry of the tumor microenvironment.

Recently colleagues of our research group have reported the impact of ATGL on the cellular metabolic modification in the A549 cell line. They observed a metabolic switch towards a glycolytic phenotype following the loss of ATGL (100). Our findings corresponded to their results, as we observed the beginning of metabolic changes towards glycolysis in ATGL-KO spheroids at the exponential phase of tumor cell growth, thus promoting the Warburg effect, which facilitates cancer cell survival in hypoxic surrounding. This was not the case in the WT group. Furthermore, an increase in glycolysis could indicate the reliance of ATGL-KO cells on glucose more than glutamine as a source for the biosynthesis of proteins and lipids. The observed adjustments in the lipid metabolism in the ATGL-KO cells under normoxia, upregulated by the ACLY and ANXA2 (35, 112), could be a consequence of the impaired lipolysis followed by the loss of ATGL, forcing the cells to depend on other metabolic pathways rather than lipolysis for FAs supply (61). Alongside the increased macromolecular biosynthesis, ATGL-KO spheroids displayed a 3-fold higher protein content as to the control group (WT), proposing an increase in production of biomass and faster growth rate. This finding was also consistent with the results from our colleagues (100).

Interestingly, the normoxic WT spheroids displayed a glucose related enzyme as well, namely pyruvate carboxylase (PC), which is a mitochondrial enzyme, that converts pyruvate into oxaloacetate and serves an anaplerotic role in the TCA (119). This could hint that the main glucose-pathway in the WT goes towards TCA and oxidative phosphorylation, whereas the ATGL-KO cells process glucose

molecules primarily through glycolysis. This finding was further seen in the LFQ proteomic analysis between the hypoxic and normoxic WT, as in both atmospheric surrounding, the WT spheroids displayed higher levels of different types of enzymes of oxidative phosphorylation. A preliminary study revealed an enhancement of PC levels and activity in NSCLC and serve as the major anaplerotic substance for TCA (119).

Furthermore, we noticed high levels of the amino acid transporter SLC7A5 in the normoxic WT spheroids, which mediates the transport of large neutral amino acids including histidine, leucin, methionine and tyrosine in a sodium-independent mechanism (126, 131). Beside the involvement of amino acids in protein biosynthesis, this may suggest that the WT cells depend more on amino acids in replenishment of the TCA intermediates and other metabolic pathways under normoxia. Interestingly, our colleagues have also detected an increase in glutamine consumption in the WT spheroids (100), further corroborating this hypothesis.

Despite the development of a hypoxic core in 3D cell culture (102, 103), the A549 cells were subjected to low oxygen concentration, in order to gain a better understanding of the influence of hypoxia on ATGL deficient lung cancer cells. In line with previously published data (20, 21), we believe, we observed hypoxia-induced inhibition of ATGL in our study, since the changes in the protein profile between the ATGL-KO and WT cells exposed to hypoxia were minimal, suggesting that the hypoxic WT spheroids possess similar phenotype of the ATGL-KO group. Nevertheless, an increase of glucose uptake was also recognized upon the hypoxic ATGL-KO spheroids as a consequence of the elevated expression of GLUT1 (128), which further corroborates the enhanced Warburg effect following the loss of ATGL. Alongside the identification of GLUT1, HMGGB was found in abundant levels in the hypoxic ATGL-KO. Both are found to be oncogenes and are linked to tumorigenesis, invasion and metastasis (128, 129), which may show that ATGL-KO cells tend to be more aggressive than the WT in hypoxia.

One of the major phenotypic changes in tumor cells under hypoxia is the metabolic switch to glycolysis, which was not viewed neither in the hypoxic WT nor in the hypoxic ATGL-KO spheroids compared to the normoxic groups. This could be due

to the performed analysis during the early phase of tumor growth, as they may be still small in size and are well nourished from the surrounding media.
Further observed changes following the low oxygen levels in the WT group was the increased mitochondrial activity as well the upregulation of enzymes of TCA including citrate synthase (CS) and malate dehydrogenase (MDH2). This emphasizes the statement, that mitochondrial activity remains preserved under hypoxia, especially in the WT cells. The increased mitochondrial activity could be explained as first cellular adaptive reaction to low oxygen levels. In addition, our results presented a 3-fold-increase in protein synthesis in the normoxic WT spheroids compared to the hypoxic WT. This could indicate a higher production of biomass and growth rate in the normoxic WT spheroids. This finding corresponds the principle, that early response of tumor cells exposed to hypoxia is reducing their overall protein biosynthesis, before the activation of HIF-1 (63).
What was also interesting in the LFQ proteomics analysis was the similar influence of hypoxia and the absence of ATGL on the cellular metabolism. We have noticed in the ATGL-KO spheroids high levels of proteins, which are usually upregulated under hypoxia through activation of HIFs. Among those were glycolytic enzymes, GLUT1 and PPIA (23, 130). In addition, some proteins were found present in both the normoxic ATGL-KO and hypoxic WT cells such as RTN4, C1QBP and TMED10. This is then corroborated in the absent difference of the proteome composition in the ATGL-KO spheroids under normoxia versus hypoxia. Altogether, this could indicate that the phenotype of ATGL-KO cells shares a high degree of similarity to the hypoxic phenotype. Moreover, this may also imply, that the function of the ATGL-deficiency could be mediated via the HIF-1 signaling pathway.

The next topic of our study was to observe the impact of hypoxia and ATGL on angiogenesis. In recent years, many researches are investigating the role of lipogenesis in angiogenesis, however the association of ATGL or lipolysis and angiogenesis is still elusive, and most studies where done on adipocyte tissues. The CAM assay was used in this work to study the angiogenic properties in company with the proteomics analysis to identify any pro- or antiangiogenic factors. As we have observed, the loss of ATGL upregulates the glycolytic pathway in the cell. Glycolytic intermediates and enzymes can induce

angiogenesis by stabilisation HIF-1 in an oxygen independent pathway (30-33). On the contrary, our results from the CAM assay revealed a significant induced angiogenesis in the WT compared to the ATGL-KO under normoxia. Even though, the key angiogenic factors were not expressed in neither groups, the LFQ proteomics displayed an overexpression of the proangiogenic factor, HMOX1, in the WT spheroids, which may promote the production of VEGF and improve cellular sensibility to VEGF (65, 121, 127). Interestingly, proangiogenic mediators were also found in the ATGL-KO cells under normoxia, namely ALCAM and RTN4. However, both factors show more supporting function of angiogenesis rather than initiation of angiogenesis (117, 118). Furthermore, this could also suggest, that HMOX1 has a stronger proangiogenic effect than RTN4 and ALCAM. This was not the case under hypoxia, as there was no angiogenic difference between the WT and ATGL-KO cells under hypoxia, probably due the inactivation of ATGL in the WT under hypoxia (21, 61), therefore preserving similar phenotype.

It is well known that hypoxia is the main trigger of angiogenesis in solid tumors via stabilization of HIF-1 (62). Nevertheless, a hypoxia-induced angiogenesis was also not observed in the CAM assay nor in the proteomics analysis. This may imply a sufficient supply of nutrients via diffusion from the medium allowing the neoplastic progression even under hypoxia. The switch to the proangiogenic phenotype occurs in solid tumors, when they increase in size over 2 mm^3, following the limited oxygen and nutrients supply (90). This may further indicate that the spheroids, regardless to the oxygen level, where smaller than 2 mm^3. Other possible reasons for missing difference in the angiogenesis, is using the supernatants instead of the cells, which contain other molecules that could interact with each other, diminishing their effectiveness. The lack of interaction between tumor cells and surrounding cells from ECs and stromal cells may also be an explanation to our results.

As a conclusion, this study further highlights the role of ATGL in regulating the metabolism in lung cancer cells. The loss of ATGL enhances lung cancer cell survival in hypoxia, as they feature a similar phenotype to hypoxia. We propose ATGL as a potential targeted therapeutic approach for cancer. The role of ATGL in tumor angiogenesis as well its molecular pathway is still unclear and requires further investigation.

For further improvement in this study, observation and understanding of metabolic and angiogenic phenotype alteration would be preferred later between day 7-10 of spheroids cultivation. In addition, a more precise and accurate measurement of angiogenesis could be done with a reliable tool. Recently, in cooperation with KML VISION, we developed a machine-learning program to quantitatively analyse the neoangiogenesis from obtained images of the collagen grids (132). This program can collect several parameters such as diameter, length, density and overall surface area of the newly formed blood vessels, which could provide us a better evaluation on angiogenesis.

5 References

1. Cancer fact sheets [Internet].; 2018 [cited June 20, 2020]. Available from: http://gco.iarc.fr/today/home.

2. Wild CP, Weiderpass E, Stewart BW. World cancer report: Cancer Research for Cancer Prevention. Lyon, France: International Agency for Research on Cancer; 2020.

3. Cancer Today [Internet].: International Agency for Research on Cancer; 2018 [cited Sep 3, 2020]. Available from: http://gco.iarc.fr/today/home.

4. Dela Cruz CS, Tanoue LT, Matthay RA. Lung cancer: epidemiology, etiology, and prevention. Clin Chest Med. 2011 Dec;32(4):605-44.

5. Sun S, Schiller JH, Gazdar AF. Lung cancer in never smokers--a different disease. Nat Rev Cancer. 2007 October 01;7(10):778-90.

6. Jameson J, Fauci A, Kasper D, Hauser S, Longo D, Loscalzo J. Harrison's Principles of Internal Medicine. 20th ed. New York: McGraw-Hill Education; 2018.

7. Lemjabbar-Alaoui H, Hassan OU, Yang YW, Buchanan P. Lung cancer: Biology and treatment options. Biochim Biophys Acta. 2015 December 01;1856(2):189-210.

8. Hanahan D, Weinberg RA. The hallmarks of cancer. Cell. 2000 January 07;100(1):57-70.

9. Hanahan D, Weinberg RA. Hallmarks of cancer: the next generation. Cell. 2011 March 04;144(5):646-74.

10. He RQ, Li XJ, Liang L, Xie Y, Luo DZ, Ma J, et al. The suppressive role of miR-542-5p in NSCLC: the evidence from clinical data and in vivo validation using a chick chorioallantoic membrane model. BMC Cancer. 2017 September 19;17(1):655-1.

11. Carmeliet P. Angiogenesis in health and disease. Nat Med. 2003 June 01;9(6):653-60.

12. Carmeliet P, Jain RK. Angiogenesis in cancer and other diseases. Nature. 2000 September 14;407(6801):249-57.

13. Soto-Pantoja DR, Menon J, Gallagher PE, Tallant EA. Angiotensin-(1-7) inhibits tumor angiogenesis in human lung cancer xenografts with a reduction in vascular endothelial growth factor. Mol Cancer Ther. 2009 June 01;8(6):1676-83.

14. Taylor LW, Kreutziger GO. The gaseous environment of the chick embryo in relation to its development and hatchability. 4. Effect of carbon dioxide and oxygen levels during the period of the thirteenth through the sixteenth days of incubation. Poult Sci. 1969 May 01;48(3):871-7.

15. Barott HG. Effect of temperature, humidity, and other factors on hatch of hens' eggs and on energy metabolism of chick embryos. U S D A Tech Bull. 1937(553).

16. File:Hallmarks of cancer.svg [Internet].: Wikimedia Commons, the free media repository; 2020 [updated 7 January 13:58 UTC; cited Sep 3, 2020]. Available from: https://commons.wikimedia.org/w/index.php?title=File:Hallmarks_of_cancer.svg&oldid=385986409.

17. Vanhove K, Graulus GJ, Mesotten L, Thomeer M, Derveaux E, Noben JP, et al. The Metabolic Landscape of Lung Cancer: New Insights in a Disturbed Glucose Metabolism. Front Oncol. 2019 November 15;9:1215.

18. Al-Zoughbi W, Pichler M, Gorkiewicz G, Guertl-Lackner B, Haybaeck J, Jahn SW, et al. Loss of adipose triglyceride lipase is associated with human cancer and induces mouse pulmonary neoplasia. Oncotarget. 2016 June 07;7(23):33832-40.

19. Tomin T, Fritz K, Gindlhuber J, Waldherr L, Pucher B, Thallinger GG, et al. Deletion of Adipose Triglyceride Lipase Links Triacylglycerol Accumulation to a More-Aggressive Phenotype in A549 Lung Carcinoma Cells. J Proteome Res. 2018 April 06;17(4):1415-25.

20. Zhang X, Saarinen AM, Hitosugi T, Wang Z, Wang L, Ho TH, et al. Inhibition of intracellular lipolysis promotes human cancer cell adaptation to hypoxia. Elife. 2017 December 19;6:10.7554/eLife.31132.

21. Padmanabha Das KM, Wechselberger L, Liziczai M, De la Rosa Rodriguez, M, Grabner GF, Heier C, et al. Hypoxia-inducible lipid droplet-associated protein inhibits adipose triglyceride lipase. J Lipid Res. 2018 March 01;59(3):531-41.

22. Beloribi-Djefaflia S, Vasseur S, Guillaumond F. Lipid metabolic reprogramming in cancer cells. Oncogenesis. 2016 January 25;5:e189.

23. Cairns RA, Harris IS, Mak TW. Regulation of cancer cell metabolism. Nat Rev Cancer. 2011 February 01;11(2):85-95.

24. DeBerardinis RJ, Chandel NS. Fundamentals of cancer metabolism. Sci Adv. 2016 May 27;2(5):e1600200.

25. Vander Heiden MG, Cantley LC, Thompson CB. Understanding the Warburg effect: the metabolic requirements of cell proliferation. Science. 2009 May 22;324(5930):1029-33.

26. Schulze A, Harris AL. How cancer metabolism is tuned for proliferation and vulnerable to disruption. Nature. 2012 November 15;491(7424):364-73.

27. Kim JW, Tchernyshyov I, Semenza GL, Dang CV. HIF-1-mediated expression of pyruvate dehydrogenase kinase: a metabolic switch required for cellular adaptation to hypoxia. Cell Metab. 2006 March 01;3(3):177-85.

28. Semenza GL, Jiang BH, Leung SW, Passantino R, Concordet JP, Maire P, et al. Hypoxia response elements in the aldolase A, enolase 1, and lactate dehydrogenase A gene promoters contain essential binding sites for hypoxia-inducible factor 1. J Biol Chem. 1996 December 20;271(51):32529-37.

29. File:TumorMetabolome.jpg [Internet].: Wikimedia Commons, the free media repository; 2020 [updated 27 April; cited 12 September 2020]. Available from: https://commons.wikimedia.org/w/index.php?title=File:TumorMetabolome.jpg&oldid=415274189.

30. King A, Selak MA, Gottlieb E. Succinate dehydrogenase and fumarate hydratase: linking mitochondrial dysfunction and cancer. Oncogene. 2006 August 07;25(34):4675-82.

31. Selak MA, Armour SM, MacKenzie ED, Boulahbel H, Watson DG, Mansfield KD, et al. Succinate links TCA cycle dysfunction to oncogenesis by inhibiting HIF-alpha prolyl hydroxylase. Cancer Cell. 2005 January 01;7(1):77-85.

32. Polet F, Feron O. Endothelial cell metabolism and tumour angiogenesis: glucose and glutamine as essential fuels and lactate as the driving force. J Intern Med. 2013 February 01;273(2):156-65.

33. Fraisl P, Mazzone M, Schmidt T, Carmeliet P. Regulation of angiogenesis by oxygen and metabolism. Dev Cell. 2009 February 01;16(2):167-79.

34. Yuneva MO, Fan TW, Allen TD, Higashi RM, Ferraris DV, Tsukamoto T, et al. The metabolic profile of tumors depends on both the responsible genetic lesion and tissue type. Cell Metab. 2012 February 08;15(2):157-70.

35. Baenke F, Peck B, Miess H, Schulze A. Hooked on fat: the role of lipid synthesis in cancer metabolism and tumour development. Dis Model Mech. 2013 November 01;6(6):1353-63.

36. Kuhajda FP. Fatty acid synthase and cancer: new application of an old pathway. Cancer Res. 2006 June 15;66(12):5977-80.

37. Walther TC, Farese RV. The life of lipid droplets. Biochim Biophys Acta. 2009 June 01;1791(6):459-66.

38. Geng F, Guo D. Lipid droplets, potential biomarker and metabolic target in glioblastoma. Intern Med Rev (Wash D C). 2017 May 01;3(5):10.18103/imr.v3i5.443.

39. Farese RV, Walther TC. Lipid droplets finally get a little R-E-S-P-E-C-T. Cell. 2009 November 25;139(5):855-60.

40. Walther TC, Farese RV. Lipid droplets and cellular lipid metabolism. Annu Rev Biochem. 2012;81:687-714.

41. Accioly MT, Pacheco P, Maya-Monteiro CM, Carrossini N, Robbs BK, Oliveira SS, et al. Lipid bodies are reservoirs of cyclooxygenase-2 and sites of prostaglandin-E2 synthesis in colon cancer cells. Cancer Res. 2008 March 15;68(6):1732-40.

42. Yue S, Li J, Lee SY, Lee HJ, Shao T, Song B, et al. Cholesteryl ester accumulation induced by PTEN loss and PI3K/AKT activation underlies human prostate cancer aggressiveness. Cell Metab. 2014 March 04;19(3):393-406.

43. Petan T, Jarc E, Jusovic M. Lipid Droplets in Cancer: Guardians of Fat in a Stressful World. Molecules. 2018 August 03;23(8):10.3390/molecules23081941.

44. Dalhaimer P. Lipid Droplets in Disease. Cells. 2019 August 26;8(9):10.3390/cells8090974.

45. File:Lipolysis Mechanism.png [Internet].: Wikimedia Commons, the free media repository; 2017 [updated 29 November; cited 15 September 2020]. Available from: https://commons.wikimedia.org/w/index.php?title=File:Lipolysis_Mechanism.png&oldid=269924311.

46. Zimmermann R, Strauss JG, Haemmerle G, Schoiswohl G, Birner-Gruenberger R, Riederer M, et al. Fat mobilization in adipose tissue is promoted by adipose triglyceride lipase. Science. 2004 November 19;306(5700):1383-6.

47. Zechner R, Zimmermann R, Eichmann TO, Kohlwein SD, Haemmerle G, Lass A, et al. FAT SIGNALS--lipases and lipolysis in lipid metabolism and signaling. Cell Metab. 2012 March 07;15(3):279-91.

48. Smirnova E, Goldberg EB, Makarova KS, Lin L, Brown WJ, Jackson CL. ATGL has a key role in lipid droplet/adiposome degradation in mammalian cells. EMBO Rep. 2006 January 01;7(1):106-13.

49. Lass A, Zimmermann R, Oberer M, Zechner R. Lipolysis - a highly regulated multi-enzyme complex mediates the catabolism of cellular fat stores. Prog Lipid Res. 2011 January 01;50(1):14-27.

50. Zagani R, El-Assaad W, Gamache I, Teodoro JG. Inhibition of adipose triglyceride lipase (ATGL) by the putative tumor suppressor G0S2 or a small molecule inhibitor attenuates the growth of cancer cells. Oncotarget. 2015 September 29;6(29):28282-95.

51. Ou J, Miao H, Ma Y, Guo F, Wei X, Zhou J, et al. Loss of Abhd5 Promotes Colorectal Tumor Development and Progression by Inducing Aerobic Glycolysis and Epithelial-Mesenchymal Transition. Cell Rep. 2018 September 04;24(10):2795-7.

52. Vegliante R, Di Leo L, Ciccarone F, Ciriolo MR. Hints on ATGL implications in cancer: beyond bioenergetic clues. Cell Death Dis. 2018 February 22;9(3):316-z.

53. Santos CR, Schulze A. Lipid metabolism in cancer. FEBS J. 2012 August 01;279(15):2610-23.

54. Pugh CW, Ratcliffe PJ. Regulation of angiogenesis by hypoxia: role of the HIF system. Nat Med. 2003 June 01;9(6):677-84.

55. Semenza GL. Defining the role of hypoxia-inducible factor 1 in cancer biology and therapeutics. Oncogene. 2010 February 04;29(5):625-34.

56. Lv X, Li J, Zhang C, Hu T, Li S, He S, et al. The role of hypoxia-inducible factors in tumor angiogenesis and cell metabolism. Genes Dis. 2016 December 14;4(1):19-24.

57. Gruber M, Simon MC. Hypoxia-inducible factors, hypoxia, and tumor angiogenesis. Curr Opin Hematol. 2006 May 01;13(3):169-74.

58. Diaz-Gonzalez JA, Russell J, Rouzaut A, Gil-Bazo I, Montuenga L. Targeting hypoxia and angiogenesis through HIF-1alpha inhibition. Cancer Biol Ther. 2005 October 01;4(10):1055-62.

59. Harris AL. Hypoxia--a key regulatory factor in tumour growth. Nat Rev Cancer. 2002 January 01;2(1):38-47.

60. File:HIF Nobel Prize Physiology Medicine 2019 Hegasy ENG.png [Internet].: Wikimedia Commons, the free media repository; 2020 [updated 3 April; cited 16 September 2020]. Available from: https://commons.wikimedia.org/w/index.php?title=File:HIF_Nobel_Prize_Physiology_Medicine_2019_Hegasy_ENG.png&oldid=408924022.

61. Zhang X, Saarinen AM, Hitosugi T, Wang Z, Wang L, Ho TH, et al. Inhibition of intracellular lipolysis promotes human cancer cell adaptation to hypoxia. Elife. 2017 December 19;6:10.7554/eLife.31132.

62. Carmeliet P, Jain RK. Angiogenesis in cancer and other diseases. Nature. 2000 September 14;407(6801):249-57.

63. Vaupel P, Mayer A. Hypoxia in cancer: significance and impact on clinical outcome. Cancer Metastasis Rev. 2007 June 01;26(2):225-39.

64. Potente M, Gerhardt H, Carmeliet P. Basic and therapeutic aspects of angiogenesis. Cell. 2011 September 16;146(6):873-87.

65. Dulak J, Deshane J, Jozkowicz A, Agarwal A. Heme oxygenase-1 and carbon monoxide in vascular pathobiology: focus on angiogenesis. Circulation. 2008 January 15;117(2):231-41.

66. Ovalle W, Nahirney P. Netter's Essential Histology. 2nd ed. Philadelphia: Elsevier; 2013.

67. Mescher A. Junqueira's Basic Histology. 15th ed. New York: McGraw-Hill Education LLC; 2018.

68. Peckham M. Histology at a Glance. Chichester, West Sussex, UK: Wiley-Blackwell; 2011.

69. Xu L, Nirwane A, Yao Y. Basement membrane and blood-brain barrier. Stroke Vasc Neurol. 2018 December 05;4(2):78-82.

70. Bergers G, Song S. The role of pericytes in blood-vessel formation and maintenance. Neuro Oncol. 2005 October 01;7(4):452-64.

71. Carmeliet P. Angiogenesis in life, disease and medicine. Nature. 2005 December 15;438(7070):932-6.

72. Viallard C, Larrivee B. Tumor angiogenesis and vascular normalization: alternative therapeutic targets. Angiogenesis. 2017 November 01;20(4):409-26.

73. Carmeliet P. Angiogenesis in health and disease. Nat Med. 2003 June 01;9(6):653-60.

74. Alison M. The Cancer Handbook. 2nd ed. Chichester, West Sussex, England: John Wiley & Sons; 2007.

75. File:Blood vessels (retouched) -en.svg [Internet].: Wikimedia Commons, the free media repository; 2018 [updated 10 August 18:34 UTC; cited Sep 3, 2020]. Available from: https://commons.wikimedia.org/w/index.php?title=File:Blood_vessels_(retouched)_-en.svg&oldid=314342386.

76. Bergers G, Benjamin LE. Tumorigenesis and the angiogenic switch. Nat Rev Cancer. 2003 June 01;3(6):401-10.

77. Ferrara N, Gerber HP, LeCouter J. The biology of VEGF and its receptors. Nat Med. 2003 June 01;9(6):669-76.

78. Dejana E, Orsenigo F, Lampugnani MG. The role of adherens junctions and VE-cadherin in the control of vascular permeability. J Cell Sci. 2008 July 01;121(Pt 13):2115-22.

79. Gavard J, Gutkind JS. VEGF controls endothelial-cell permeability by promoting the beta-arrestin-dependent endocytosis of VE-cadherin. Nat Cell Biol. 2006 November 01;8(11):1223-34.

80. Carmeliet P. Mechanisms of angiogenesis and arteriogenesis. Nat Med. 2000 April 01;6(4):389-95.

81. Luttun A, Dewerchin M, Collen D, Carmeliet P. The role of proteinases in angiogenesis, heart development, restenosis, atherosclerosis, myocardial ischemia, and stroke: insights from genetic studies. Curr Atheroscler Rep. 2000 September 01;2(5):407-16.

82. Carmeliet P, Jain RK. Molecular mechanisms and clinical applications of angiogenesis. Nature. 2011 May 19;473(7347):298-307.

83. Gerhardt H, Golding M, Fruttiger M, Ruhrberg C, Lundkvist A, Abramsson A, et al. VEGF guides angiogenic sprouting utilizing endothelial tip cell filopodia. J Cell Biol. 2003 June 23;161(6):1163-77.

84. Iruela-Arispe ML, Davis GE. Cellular and molecular mechanisms of vascular lumen formation. Dev Cell. 2009 February 01;16(2):222-31.

85. O'Reilly MS, Holmgren L, Shing Y, Chen C, Rosenthal RA, Moses M, et al. Angiostatin: a novel angiogenesis inhibitor that mediates the suppression of metastases by a Lewis lung carcinoma. Cell. 1994 October 21;79(2):315-28.

86. Nyberg P, Xie L, Kalluri R. Endogenous inhibitors of angiogenesis. Cancer Res. 2005 May 15;65(10):3967-79.

87. Lawler J. Thrombospondin-1 as an endogenous inhibitor of angiogenesis and tumor growth. J Cell Mol Med. 2002 March 01;6(1):1-12.

88. Luttun A, Tjwa M, Moons L, Wu Y, Angelillo-Scherrer A, Liao F, et al. Revascularization of ischemic tissues by PlGF treatment, and inhibition of tumor angiogenesis, arthritis and atherosclerosis by anti-Flt1. Nat Med. 2002 August 01;8(8):831-40.

89. Johnson T, Zhao L, Manuel G, Taylor H, Liu D. Approaches to therapeutic angiogenesis for ischemic heart disease. J Mol Med (Berl). 2019 February 01;97(2):141-51.

90. Nishida N, Yano H, Nishida T, Kamura T, Kojiro M. Angiogenesis in cancer. Vasc Health Risk Manag. 2006;2(3):213-9.

91. Folkman J, Shing Y. Angiogenesis. J Biol Chem. 1992 Jun 5;267(16):10931-4.

92. Paduch R. The role of lymphangiogenesis and angiogenesis in tumor metastasis. Cell Oncol (Dordr). 2016 Oct;39(5):397-410.

93. Nagy JA, Chang SH, Shih SC, Dvorak AM, Dvorak HF. Heterogeneity of the tumor vasculature. Semin Thromb Hemost. 2010 April 01;36(3):321-31.

94. Jain RK. The next frontier of molecular medicine: delivery of therapeutics. Nat Med. 1998 June 01;4(6):655-7.

95. Marme D. Tumor Angiogenesis: A Key Target for Cancer Therapy. Oncol Res Treat. 2018;41(4):164.

96. Soria JC, Mauguen A, Reck M, Sandler AB, Saijo N, Johnson DH, et al. Systematic review and meta-analysis of randomised, phase II/III trials adding bevacizumab to platinum-based chemotherapy as first-line treatment in patients with advanced non-small-cell lung cancer. Ann Oncol. 2013 January 01;24(1):20-30.

97. Sandler A, Yi J, Dahlberg S, Kolb MM, Wang L, Hambleton J, et al. Treatment outcomes by tumor histology in Eastern Cooperative Group Study E4599 of bevacizumab with paclitaxel/carboplatin for advanced non-small cell lung cancer. J Thorac Oncol. 2010 September 01;5(9):1416-23.

98. Seguin F, Carvalho MA, Bastos DC, Agostini M, Zecchin KG, Alvarez-Flores MP, et al. The fatty acid synthase inhibitor orlistat reduces experimental metastases and angiogenesis in B16-F10 melanomas. Br J Cancer. 2012 September 04;107(6):977-87.

99. Nebel LM, Ghaffari Tabrizi-Wizsy N. Behaviour of ATGL deficient A549 lung carcinoma cells cultivated in 3D and on CAM. In press 2018.

100. Honeder S, Tomin T, Nebel L, Gindlhuber J, Fritz-Wallace K, Schinagl M, et al. Adipose Triglyceride Lipase (ATGL) Knockout Promotes Metabolic Switch in Non-Small Cell Lung Cancer (NSCLC) Spheroids. In press .

101. A549 CELL LINE: CELL CULTURE AND TRANSFECTION PROTOCOL [Internet]. [cited 21 Sept 2020]. Available from: http://www.a549.com/.

102. Nyga A, Cheema U, Loizidou M. 3D tumour models: novel in vitro approaches to cancer studies. J Cell Commun Signal. 2011 August 01;5(3):239-48.

103. Hirschhaeuser F, Menne H, Dittfeld C, West J, Mueller-Klieser W, Kunz-Schughart LA. Multicellular tumor spheroids: an underestimated tool is catching up again. J Biotechnol. 2010 Jul 1;148(1):3-15.

104. Cox J, Mann M. MaxQuant enables high peptide identification rates, individualized p.p.b.-range mass accuracies and proteome-wide protein quantification. Nat Biotechnol. 2008 December 01;26(12):1367-72.

105. Tyanova S, Temu T, Sinitcyn P, Carlson A, Hein MY, Geiger T, et al. The Perseus computational platform for comprehensive analysis of (prote)omics data. Nat Methods. 2016 September 01;13(9):731-40.

106. Szklarczyk D, Gable AL, Lyon D, Junge A, Wyder S, Huerta-Cepas J, et al. STRING v11: protein-protein association networks with increased coverage, supporting functional discovery in genome-wide experimental datasets. Nucleic Acids Res. 2019 January 08;47(D1):D607-13.

107. Tufan AC, Satiroglu-Tufan NL. The chick embryo chorioallantoic membrane as a model system for the study of tumor angiogenesis, invasion and development of anti-angiogenic agents. Curr Cancer Drug Targets. 2005 June 01;5(4):249-66.

108. Nowak-Sliwinska P, Segura T, Iruela-Arispe ML. The chicken chorioallantoic membrane model in biology, medicine and bioengineering. Angiogenesis. 2014 October 01;17(4):779-804.

109. Gabrielli MG, Accili D. The chick chorioallantoic membrane: a model of molecular, structural, and functional adaptation to transepithelial ion transport and barrier function during embryonic development. J Biomed Biotechnol. 2010;2010:940741.

110. Deryugina EI, Quigley JP. Chapter 2. Chick embryo chorioallantoic membrane models to quantify angiogenesis induced by inflammatory and tumor cells or purified effector molecules. Methods Enzymol. 2008;444:21-41.

111. Ribatti D. The chick embryo chorioallantoic membrane (CAM). A multifaceted experimental model. Mech Dev. 2016 August 01;141:70-7.

112. Seidah NG, Poirier S, Denis M, Parker R, Miao B, Mapelli C, et al. Annexin A2 is a natural extrahepatic inhibitor of the PCSK9-induced LDL receptor degradation. PLoS One. 2012;7(7):e41865.

113. Eukaryotic small ribosomal subunit (40S) [Internet].: Wikipedia, The Free Encyclopedia; 2020 [updated 29 June; cited 4 October 2020]. Available from: https://en.wikipedia.org/w/index.php?title=Eukaryotic_small_ribosomal_subunit_(40S)&oldid=965135511.

114. Yoshikawa H, Komatsu W, Hayano T, Miura Y, Homma K, Izumikawa K, et al. Splicing factor 2-associated protein p32 participates in ribosome biogenesis by regulating the binding of Nop52 and fibrillarin to preribosome particles. Mol Cell Proteomics. 2011 August 01;10(8):M110.006148.

115. Martineau Y, Muller D, Pyronnet S. Targeting protein synthesis in cancer cells. Oncoscience. 2014 July 04;1(7):484-5.

116. UniProt Consortium. UniProt: a worldwide hub of protein knowledge. Nucleic Acids Res. 2019 January 08;47(D1):D506-15.

117. Darvishi B, Boroumandieh S, Majidzadeh-A K, Salehi M, Jafari F, Farahmand L. The role of activated leukocyte cell adhesion molecule (ALCAM) in cancer progression, invasion, metastasis and recurrence: A novel cancer stem cell marker and tumor-specific prognostic marker. Exp Mol Pathol. 2020 August 01;115:104443.

118. Acevedo L, Yu J, Erdjument-Bromage H, Miao RQ, Kim JE, Fulton D, et al. A new role for Nogo as a regulator of vascular remodeling. Nat Med. 2004 April 01;10(4):382-8.

119. Sellers K, Fox MP, Bousamra M, Slone SP, Higashi RM, Miller DM, et al. Pyruvate carboxylase is critical for non-small-cell lung cancer proliferation. J Clin Invest. 2015 February 01;125(2):687-98.

120. Hirai K, Sasahira T, Ohmori H, Fujii K, Kuniyasu H. Inhibition of heme oxygenase-1 by zinc protoporphyrin IX reduces tumor growth of LL/2 lung cancer in C57BL mice. Int J Cancer. 2007 February 01;120(3):500-5.

121. Tsai JR, Wang HM, Liu PL, Chen YH, Yang MC, Chou SH, et al. High expression of heme oxygenase-1 is associated with tumor invasiveness and poor clinical outcome in non-small cell lung cancer patients. Cell Oncol (Dordr). 2012 December 01;35(6):461-71.

122. Hayashi K, Anzai N. Novel therapeutic approaches targeting L-type amino acid transporters for cancer treatment. World J Gastrointest Oncol. 2017 January 15;9(1):21-9.

123. Kaira K, Oriuchi N, Imai H, Shimizu K, Yanagitani N, Sunaga N, et al. Prognostic significance of L-type amino acid transporter 1 expression in resectable stage I-III nonsmall cell lung cancer. Br J Cancer. 2008 February 26;98(4):742-8.

124. Kaira K, Oriuchi N, Imai H, Shimizu K, Yanagitani N, Sunaga N, et al. Prognostic significance of L-type amino acid transporter 1 (LAT1) and 4F2 heavy chain (CD98) expression in surgically resectable stage III non-small cell lung cancer. Exp Ther Med. 2010 September 01;1(5):799-808.

125. Kumar D, Hassan MK, Pattnaik N, Mohapatra N, Dixit M. Reduced expression of IQGAP2 and higher expression of IQGAP3 correlates with poor prognosis in cancers. PLOS ONE. 2017;12(10):e0186977.

126. Scalise M, Galluccio M, Console L, Pochini L, Indiveri C. The Human SLC7A5 (LAT1): The Intriguing Histidine/Large Neutral Amino Acid Transporter and Its Relevance to Human Health. Front Chem. 2018 June 22;6:243.

127. Was H, Cichon T, Smolarczyk R, Rudnicka D, Stopa M, Chevalier C, et al. Overexpression of heme oxygenase-1 in murine melanoma: increased

proliferation and viability of tumor cells, decreased survival of mice. Am J Pathol. 2006 December 01;169(6):2181-98.

128. Pezzuto A, D'Ascanio M, Ricci A, Pagliuca A, Carico E. Expression and role of p16 and GLUT1 in malignant diseases and lung cancer: A review. Thorac Cancer. 2020 September 18.

129. Zhou GH, Lu YY, Xie JL, Gao ZK, Wu XB, Yao WS, et al. Overexpression of miR-758 inhibited proliferation, migration, invasion, and promoted apoptosis of non-small cell lung cancer cells by negatively regulating HMGB. Biosci Rep. 2019 January 18;39(1):10.1042/BSR20180855. Print 2019 Jan 31.

130. Choi KJ, Piao YJ, Lim MJ, Kim JH, Ha J, Choe W, et al. Overexpressed cyclophilin A in cancer cells renders resistance to hypoxia- and cisplatin-induced cell death. Cancer Res. 2007 April 15;67(8):3654-62.

131. Biochemie-Poster [Internet]. [cited 19 October 2020]. Available from: https://www.medi-learn.de/examen/BiochemiePoster/index.php.

132. KML Vision [Internet].; 2016 [cited 23 October 2020]. Available from: https://www.kmlvision.com/.

6 Appendix

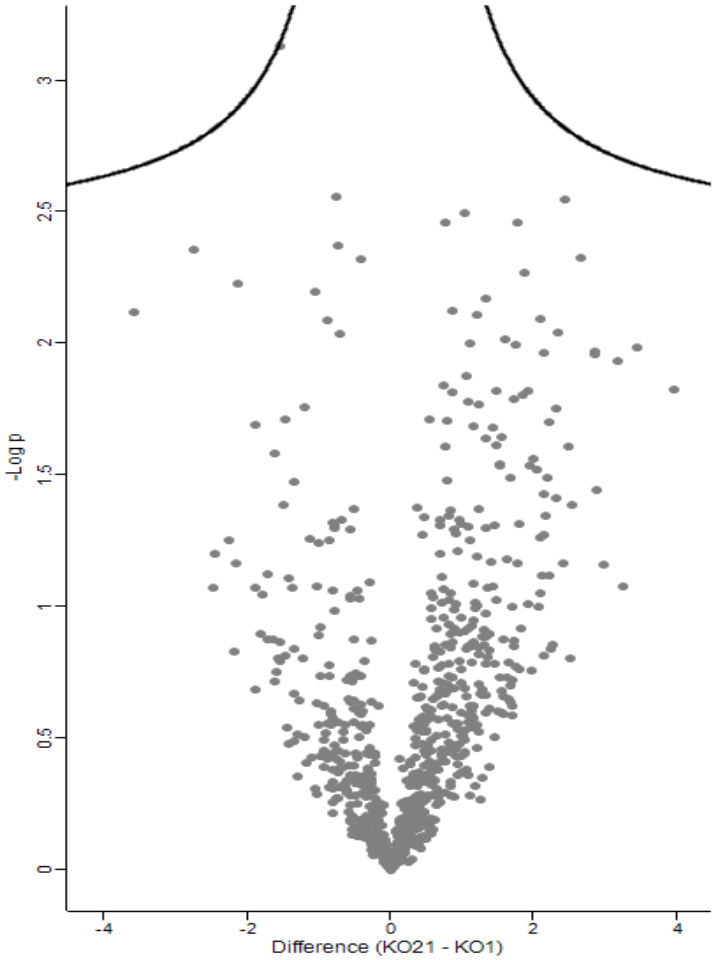

Supplementary figure 1. Volcano plot of label free quantitative proteomics screening of A549 ATGL-KO in hypoxia vs in normoxia. The dots under the curve lines indicate no significant difference in the protein composition of the ATGL-KO group in different oxygen concentration (- log $p > 2.5$).

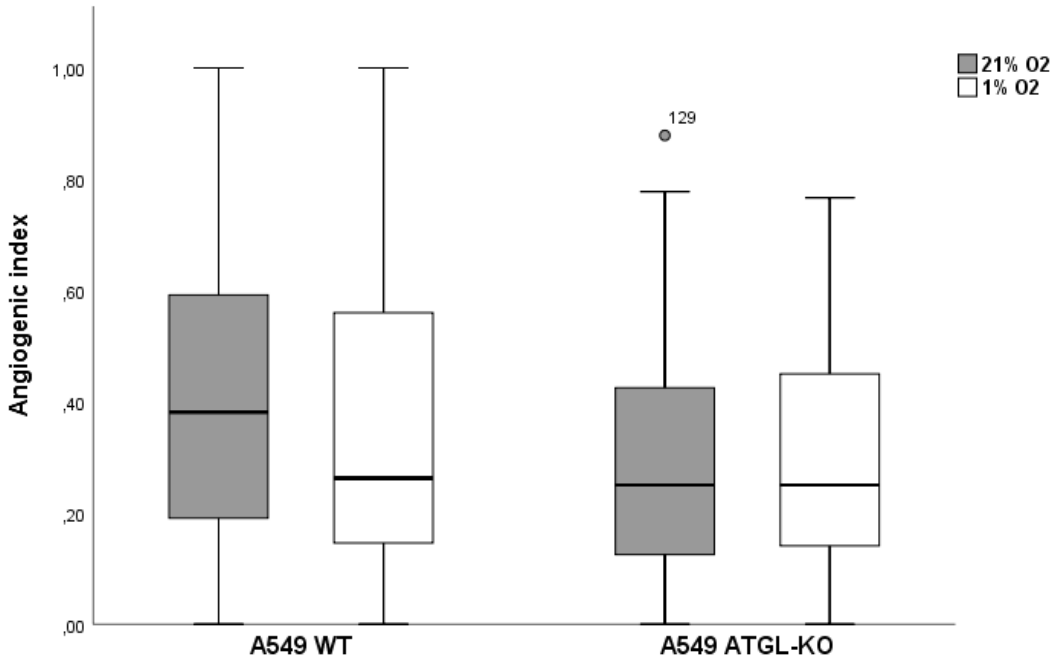

Supplementary figure 2. Boxplot diagram of the data from the angiogenesis CAM assay.

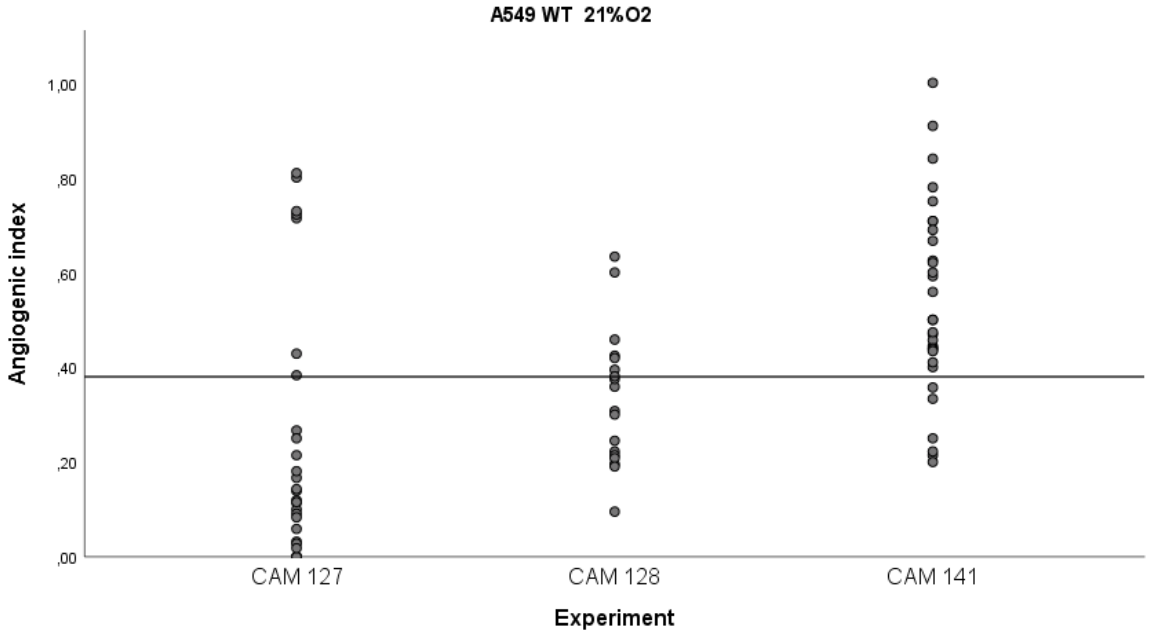

Supplementary figure 3. Scatter plot of angiogenic indices in A549 WT pre-incubated under 21% O_2 in each experimental replicate (n=3). Horizontal line through the dots represents the mean.

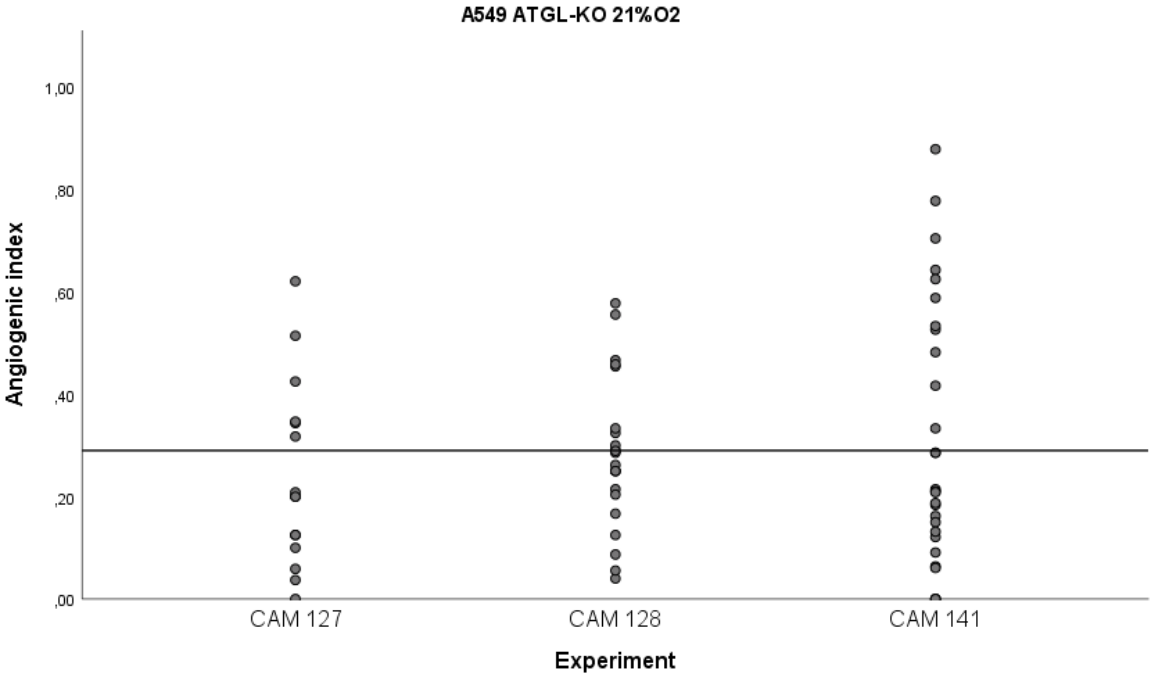

Supplementary figure 4. Scatter plot of angiogenic indices in A549 ATGL-KO pre-incubated under 21% O_2 in each experimental replicate (n=3). Horizontal line represents the mean value.

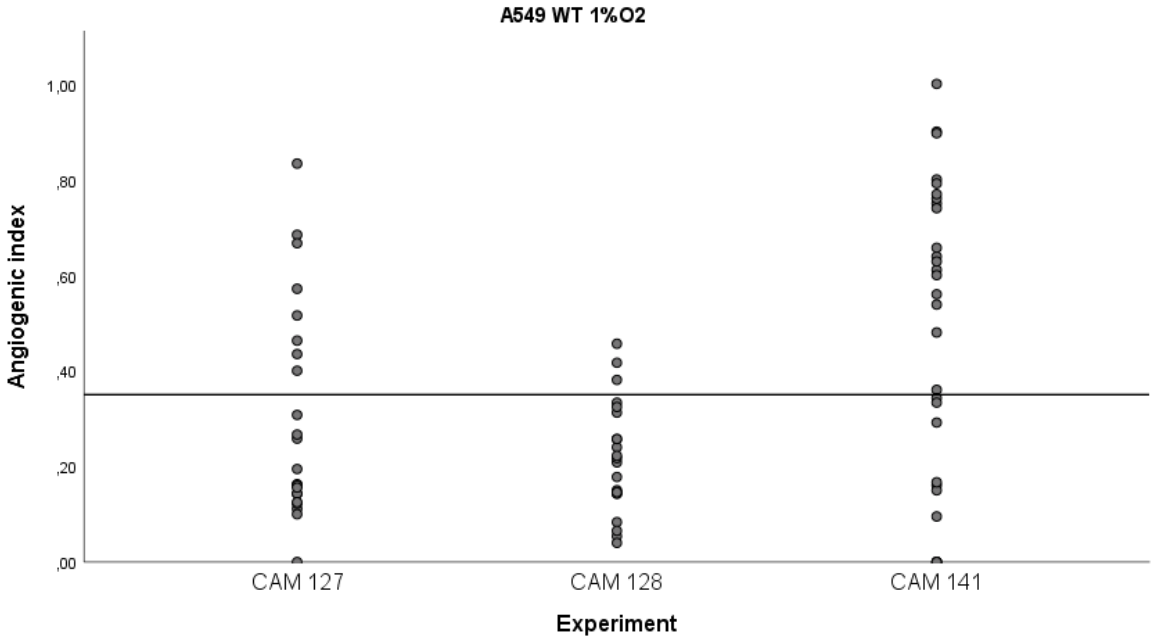

Supplementary figure 5. Scatter plot of angiogenic indices in A549 WT pre-incubated under 1% O_2 in each experimental replicate (n=3). Transversal line represents the mean.

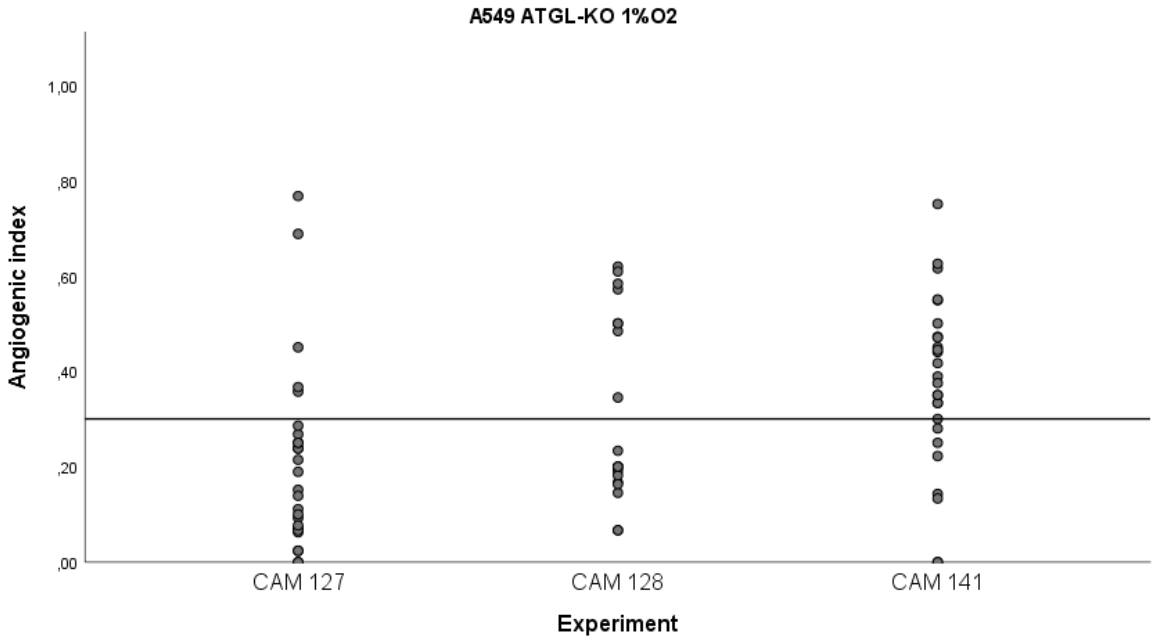

Supplementary figure 6. Scatter plot of angiogenic indices in A549 ATGL-KO pre-incubated under 1% O_2 in each experimental replicate (n=3). Transversal line represents the mean.

Protein ID	Protein name	Gene name	Fold Change WT 21% to WT 1%
P00403	Cytochrome c oxidase subunit 2	MT-CO2	0,070942388
Q07021	Complement component 1 Q subcomponent-binding protein	C1QBP	0,081220132
Q9NQC3	Reticulon-4	RTN4	0,10591394
P42126	Enoyl-CoA delta isomerase 1	ECI1	0,17617855
Q12905	Interleukin enhancer-binding factor 2	ILF2	0,176495919
P32969	60S ribosomal protein L9	RPL9	0,186361081
Q86V81	THO complex subunit 4	ALYREF	0,191075754
P68366	Tubulin alpha-4A chain	TUBA4A	0,203367336
P07437	Tubulin beta chain	TUBB	0,22538378
P02751	Fibronectin	FN1	0,243357512
P49755	Transmembrane emp24 domain-containing protein 10	TMED10	0,244439874
Q9NZI8	Insulin-like growth factor 2 mRNA-binding protein 1	IGF2BP1	0,293530435
Q9Y5L4	Mitochondrial import inner membrane translocase subunit Tim13	TIMM13	0,295348193
Q9BQG0	Myb-binding protein 1A	MYBBP1A	0,354555562
P06576	ATP synthase subunit beta	ATP5B	0,368624671
P52597	Heterogeneous nuclear ribonucleoprotein F	HNRNPF	0,392384101
O75390	Citrate synthase	CS	0,393379479
Q12906	Interleukin enhancer-binding factor 3	ILF3	0,407766633
P16615	Sarcoplasmic/endoplasmic reticulum calcium ATPase 2	ATP2A2	0,409003037
O75367	Core histone macro-H2A.1	H2AFY	0,436704933
P12814	Alpha-actinin-1	ACTN1	0,467463044
P52815	39S ribosomal protein L12	MRPL12	0,477429975
Q09666	Neuroblast differentiation-associated protein AHNAK	AHNAK	0,482371135
Q15393	Splicing factor 3B subunit 3	SF3B3	0,488282039
Q9H9B4	Sideroflexin-1	SFXN1	0,502273833
P55072	Transitional endoplasmic reticulum ATPase	VCP	0,509863955
P08195	4F2 cell-surface antigen heavy chain	SLC3A2	0,558547751
P21796	Voltage-dependent anion-selective channel protein 1	VDAC1	0,560605876
P40926	Malate dehydrogenase	MDH2	0,58216252
Q9BSJ8	Extended synaptotagmin-1	ESYT1	0,592850241
P11021	78 kDa glucose-regulated protein	HSPA5	0,599437497

P05387	60S acidic ribosomal protein P2	RPLP2	0,62626355
P07686	Beta-hexosaminidase subunit beta	HEXB	1,874965651
Q32MZ4	Leucine-rich repeat flightless-interacting protein 1	LRRFIP1	1,953298587
Q9BY43	Charged multivesicular body protein 4a	CHMP4A	1,970261168
P35222	Catenin beta-1	CTNNB1	2,00562848
O60832	H/ACA ribonucleoprotein complex subunit 4	DKC1	2,020459461
O43175	D-3-phosphoglycerate dehydrogenase	PHGDH	2,139182499
P38919	Eukaryotic initiation factor 4A-III	EIF4A3	2,152307061
Q15233	Non-POU domain-containing octamer-binding protein	NONO	2,243127225
P08758	Annexin A5	ANXA5	2,260706505
O00429	Dynamin-1-like protein	DNM1L	2,261994056
Q9P2E9	Ribosome-binding protein 1	RRBP1	2,26788107
P49419	Alpha-aminoadipic semialdehyde dehydrogenase	ALDH7A1	2,294699326
Q04917	14-3-3 protein eta	YWHAH	2,408603204
P17980	26S protease regulatory subunit 6A	PSMC3	2,424847503
P28070	Proteasome subunit beta type-4	PSMB4	2,441122825
P62277	40S ribosomal protein S13	RPS13	2,459899275
Q14697	Neutral alpha-glucosidase AB	GANAB	2,463122114
P40939	Trifunctional enzyme subunit alpha	HADHA	2,566998809
P50402	Emerin	EMD	2,603338352
P61803	Dolichyl-diphosphooligosaccharide--protein glycosyltransferase subunit DAD1	DAD1	2,640469844
P61254	60S ribosomal protein L26	RPL26	2,714671183
Q8N1F7	Nuclear pore complex protein Nup93	NUP93	2,717925359
P46459	Vesicle-fusing ATPase	NSF	2,726592405
P60228	Eukaryotic translation initiation factor 3 subunit E	EIF3E	2,749597129
P42704	Leucine-rich PPR motif-containing protein	LRPPRC	2,765509296
Q9BRP8	Partner of Y14 and mago	WIBG	2,8471998
P08134	Rho-related GTP-binding protein RhoC	RHOC	2,850162517
P61981	14-3-3 protein gamma	YWHAG	2,88296166

O60841	Eukaryotic translation initiation factor 5B	EIF5B	2,88358427
P60468	Protein transport protein Sec61 subunit beta	SEC61B	2,92083463
Q9H3P7	Golgi resident protein GCP60	ACBD3	2,943069371
O00232	26S proteasome non-ATPase regulatory subunit 12	PSMD12	2,995883961
P62263	40S ribosomal protein S14	RPS14	3,071827902
P39023	60S ribosomal protein L3	RPL3	3,076348613
P39748	Flap endonuclease 1	FEN1	3,141150611
Q99426	Tubulin-folding cofactor B	TBCB	3,151568616
Q9H910	Hematological and neurological expressed 1-like protein	HN1L	3,155046176
Q9Y266	Nuclear migration protein nudC	NUDC	3,187366397
P31937	3-hydroxyisobutyrate dehydrogenase	HIBADH	3,296184283
Q13596	Sorting nexin-1	SNX1	3,334342445
Q99623	Prohibitin-2	PHB2	3,349589318
P13533	Myosin-6	MYH6	3,379562683
P39019	40S ribosomal protein S19	RPS19	3,391846717
P46060	Ran GTPase-activating protein 1	RANGAP1	3,530426928
P10412	Histone H1.4	HIST1H1E	3,566268772
P28074	Proteasome subunit beta type-5	PSMB5	3,626675499
P52594	Arf-GAP domain and FG repeat-containing protein 1	AGFG1	3,633084519
Q13435	Splicing factor 3B subunit 2	SF3B2	3,662180542
P31948	Stress-induced-phosphoprotein 1	STIP1	3,670254039
Q7Z2W4	Zinc finger CCCH-type antiviral protein 1	ZC3HAV1	3,684329306
P23588	Eukaryotic translation initiation factor 4B	EIF4B	3,691250117
P82979	SAP domain-containing ribonucleoprotein	SARNP	3,699534428
P25788	Proteasome subunit alpha type-3	PSMA3	3,866992401
Q15758	Neutral amino acid transporter B(0)	SLC1A5	3,922070513
Q92598	Heat shock protein 105 kDa	HSPH1	3,954320779
Q14247	Src substrate cortactin	CTTN	3,991304933
Q9BXP5	Serrate RNA effector molecule homolog	SRRT	4,043381625
O60763	General vesicular transport factor p115	USO1	4,060546299
P09496	Clathrin light chain A	CLTA	4,140097705

Q9H3N1	Thioredoxin-related transmembrane protein 1	TMX1	4,184967394
Q15046	Lysine--tRNA ligase	KARS	4,211180722
O95292	Vesicle-associated membrane protein-associated protein B/C	VAPB	4,239115052
P49321	Nuclear autoantigenic sperm protein	NASP	4,282688604
Q9HDC9	Adipocyte plasma membrane-associated protein	APMAP	4,308203804
P30740	Leukocyte elastase inhibitor	SERPINB1	4,376478845
P18859	ATP synthase-coupling factor 6	ATP5J	4,408815279
P27216	Annexin A13	ANXA13	4,441345619
P28072	Proteasome subunit beta type-6	PSMB6	4,467231169
Q6PUV4	Complexin-2	CPLX2	4,535521283
P30049	ATP synthase subunit delta	ATP5D	4,575599647
Q13347	Eukaryotic translation initiation factor 3 subunit I	EIF3I	4,666715956
P62995	Transformer-2 protein homolog beta	TRA2B	4,85341733
Q14683	Structural maintenance of chromosomes protein 1A	SMC1A	4,989451938
P78347	General transcription factor II-I	GTF2I	5,144344293
Q9Y383	Putative RNA-binding protein Luc7-like 2	LUC7L2	5,25971708
P62917	60S ribosomal protein L8	RPL8	5,290600839
P68104	Elongation factor 1-alpha 1	EEF1A1	5,440520414
Q16658	Fascin	FSCN1	5,496091911
Q14978	Nucleolar and coiled-body phosphoprotein 1	NOLC1	5,522234836
Q96FQ6	Protein S100-A16	S100A16	5,524555761
P60900	Proteasome subunit alpha type-6	PSMA6	5,792364332
Q92688	Acidic leucine-rich nuclear phosphoprotein 32 family member B	ANP32B	5,94713856
P25786	Proteasome subunit alpha type-1	PSMA1	5,983678877
P31930	Cytochrome b-c1 complex subunit 1	UQCRC1	6,090204916
P09012	U1 small nuclear ribonucleoprotein A	SNRPA	6,792166518
Q969Q0	60S ribosomal protein L36a-like	RPL36AL	6,926534159
Q14914	Prostaglandin reductase 1	PTGR1	7,101834583
P20674	Cytochrome c oxidase subunit 5A	COX5A	7,123949084
P46778	60S ribosomal protein L21	RPL21	7,272359801

P05114	Non-histone chromosomal protein HMG-14	HMGN1	7,414738434
Q9UKM9	RNA-binding protein Raly	RALY	7,510990939
O15143	Actin-related protein 2/3 complex subunit 1B	ARPC1B	7,716805636
Q15363	Transmembrane emp24 domain-containing protein 2	TMED2	7,811170007
P62854	40S ribosomal protein S26	RPS26	8,708656644
P63220	40S ribosomal protein S21	RPS21	8,733896162
Q8N684	Cleavage and polyadenylation specificity factor subunit 7	CPSF7	8,998661828
P62280	40S ribosomal protein S11	RPS11	10,47622689
P61956	Small ubiquitin-related modifier 2	SUMO2	10,91196323
P46779	60S ribosomal protein L28	RPL28	12,68915841
P61026	Ras-related protein Rab-10	RAB10	13,89482164
Q02878	60S ribosomal protein L6	RPL6	14,21317729
P25815	Protein S100-P	S100P	36,35481931

Supplementary table 1. Complete list of expressed proteins in the normoxic WT vs hypoxic WT cells from the LFQ analysis. Fold change values under one indicates proteins highly upregulated in the WT cultivated in 1% oxygen, while over one implies significant protein component in WT in normoxia.

Protein ID	Protein name	Gene name	Fold Change WT 21% to KO 21%
P05141	ADP/ATP translocase 2	SLC25A5	0,018297881
P68133	Actin	ACTA1	0,021476194
P35637	RNA-binding protein FUS	FUS	0,039895543
Q9BQE3	Tubulin alpha-1C chain	TUBA1C	0,101687555
Q9NQC3	Reticulon-4	RTN4	0,104896471
P61088	Ubiquitin-conjugating enzyme E2 N	UBE2N	0,106262981
Q13740	CD166 antigen	ALCAM	0,163286747
Q07021	Complement component 1 Q subcomponent-binding protein	C1QBP	0,166509338
P62841	40S ribosomal protein S15	RPS15	0,202464877
Q9UPQ0	LIM and calponin homology domains-containing protein 1	LIMCH1	0,246778632
O14737	Programmed cell death protein 5	PDCD5	0,249976961
P09972	Fructose-bisphosphate aldolase C	ALDOC	0,254148277
P68363	Tubulin alpha-1B chain	TUBA1B	0,254680222
P35659	Protein DEK	DEK	0,259605035
Q13561	Dynactin subunit 2	DCTN2	0,320590396
Q8TCJ2	Dolichyl-diphosphooligosaccharide--protein glycosyltransferase subunit STT3B	STT3B	0,325882072
Q14011	Cold-inducible RNA-binding protein	CIRBP	0,328946577
P62937	Peptidyl-prolyl cis-trans isomerase A	PPIA	0,330906651
O15344	E3 ubiquitin-protein ligase Midline-1	MID1	0,347947394
Q9Y3Y2	Chromatin target of PRMT1 protein	CHTOP	0,35442094
P49755	Transmembrane emp24 domain-containing protein 10	TMED10	0,358516218
Q01813	ATP-dependent 6-phosphofructokinase	PFKP	0,364585439
P53396	ATP-citrate synthase	ACLY	0,387974698
Q14152	Eukaryotic translation initiation factor 3 subunit A	EIF3A	0,406655767
P27824	Calnexin	CANX	0,416878867
P17987	T-complex protein 1 subunit alpha	TCP1	0,434391363
P12814	Alpha-actinin-1	ACTN1	0,470368284
P08708	40S ribosomal protein S17	RPS17	0,471351125
P06733	Alpha-enolase	ENO1	0,495313701
P15311	Ezrin	EZR	0,520481986

P07355	Annexin A2	ANXA2	0,532440494
P14618	Pyruvate kinase PKM	PKM	0,543196443
P11498	Pyruvate carboxylase	PC	1,858139416
P37837	Transaldolase	TALDO1	2,254208205
Q13576	Ras GTPase-activating-like protein IQGAP2	IQGAP2	2,586294501
Q13045	Protein flightless-1 homolog	FLII	2,705999994
Q01650	Large neutral amino acids transporter small subunit 1	SLC7A5	3,043977776
P13533	Myosin-6	MYH6	3,645857224
Q9GZR7	ATP-dependent RNA helicase DDX24	DDX24	4,01330915
P61604	10 kDa heat shock protein	HSPE1	4,292311636
P09601	Heme oxygenase 1	HMOX1	5,513140973
P16401	Histone H1.5	HIST1H1B	9,514048935

Supplementary table 2. List of expressed proteins in the ATGL-KO group compared to WT in normoxia from the LFQ analysis. Fold change values less than one indicate overexpression of proteins in the ATGL-KO, while values higher than one refer to significant protein composition in the WT cells.

Protein ID	Protein name	Gene name	Fold Change WT 21% to KO21%
O15347	High mobility group protein B3	HMGB3	0,0349964
P11166	Solute carrier family 2, facilitated glucose transporter member 1	SLC2A1	0,1378354
P51571	Translocon-associated protein subunit delta	SSR4	0,206441
Q15363	Transmembrane emp24 domain-containing protein 2	TMED2	0,1443175

Supplementary table 3. List of expressed proteins in the ATGL-KO group compared to WT in hypoxia from the LFQ analysis. Fold change values are under one meaning proteins are mainly upregulated in the ATGL-KO group.

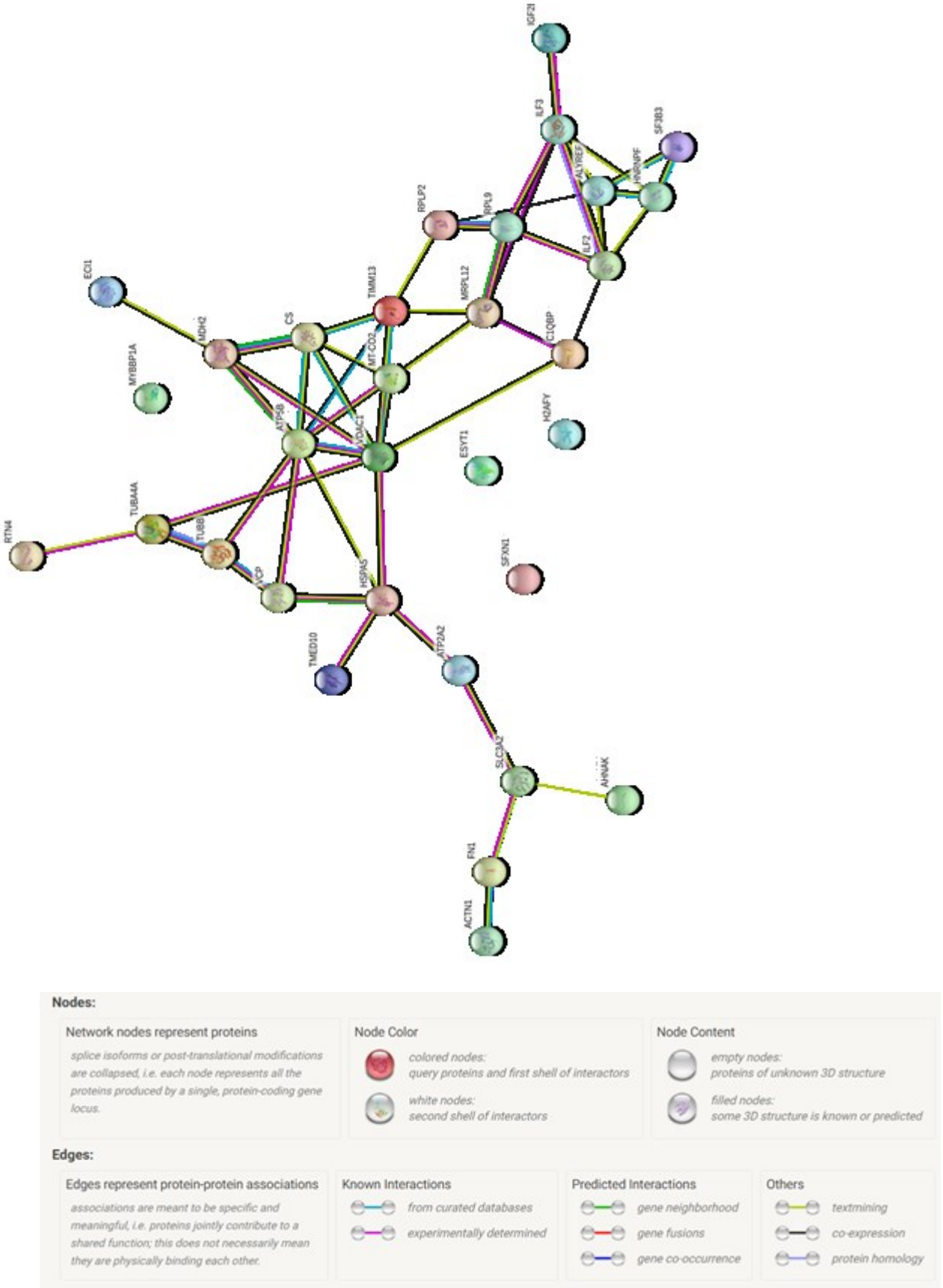

Supplementary figure 7. Bitmap of association network of the upregulated proteins in the hypoxic A549-WT spheroids versus normoxic WT group. Obtained from STRING at https://string-db.org (106).

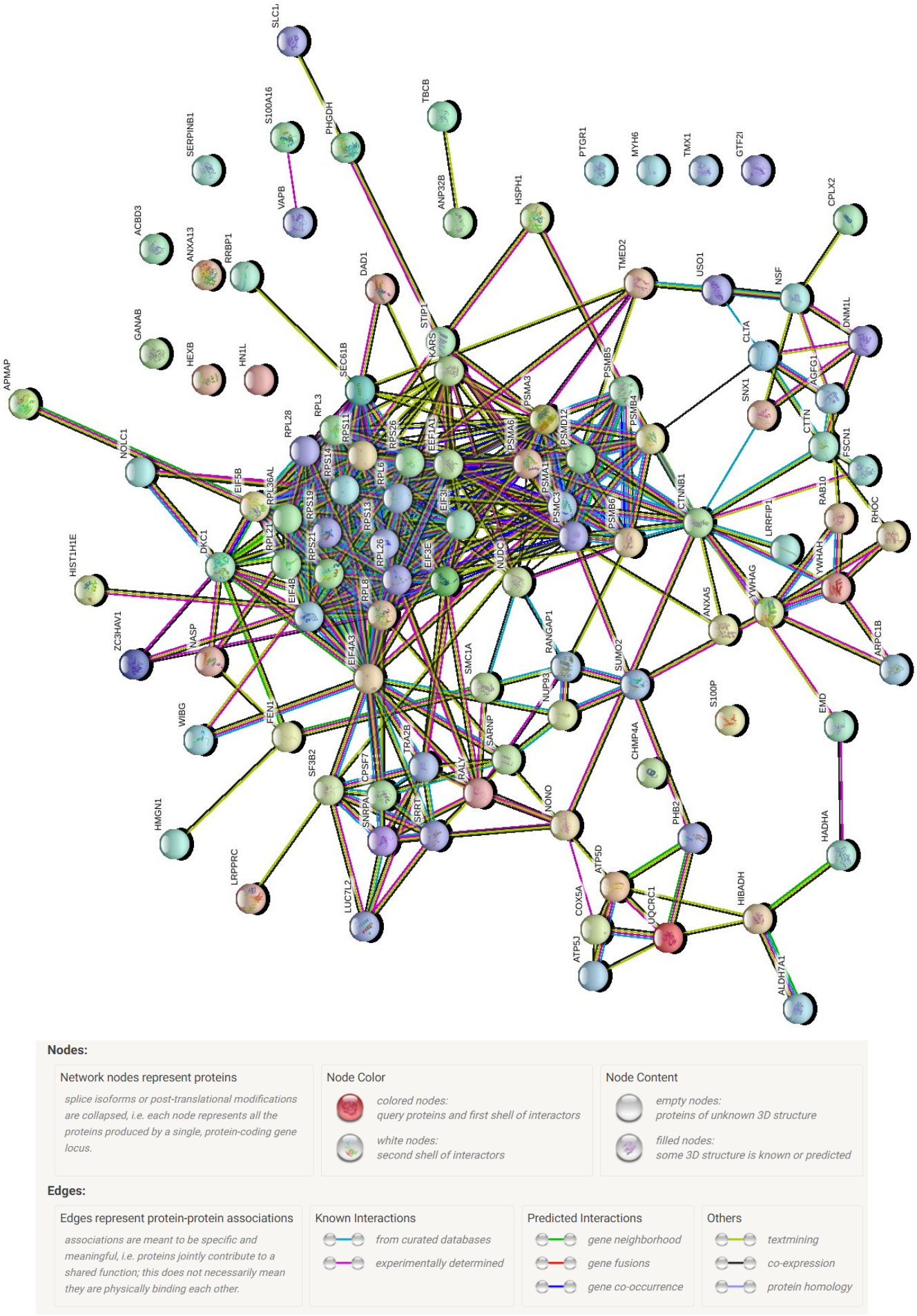

Supplementary figure 8. Bitmap of association network of the upregulated proteins in the normoxic A549-WT spheroids compared to hypoxic WT group**.** Obtained from STRING at https://string-db.org (106)**.**

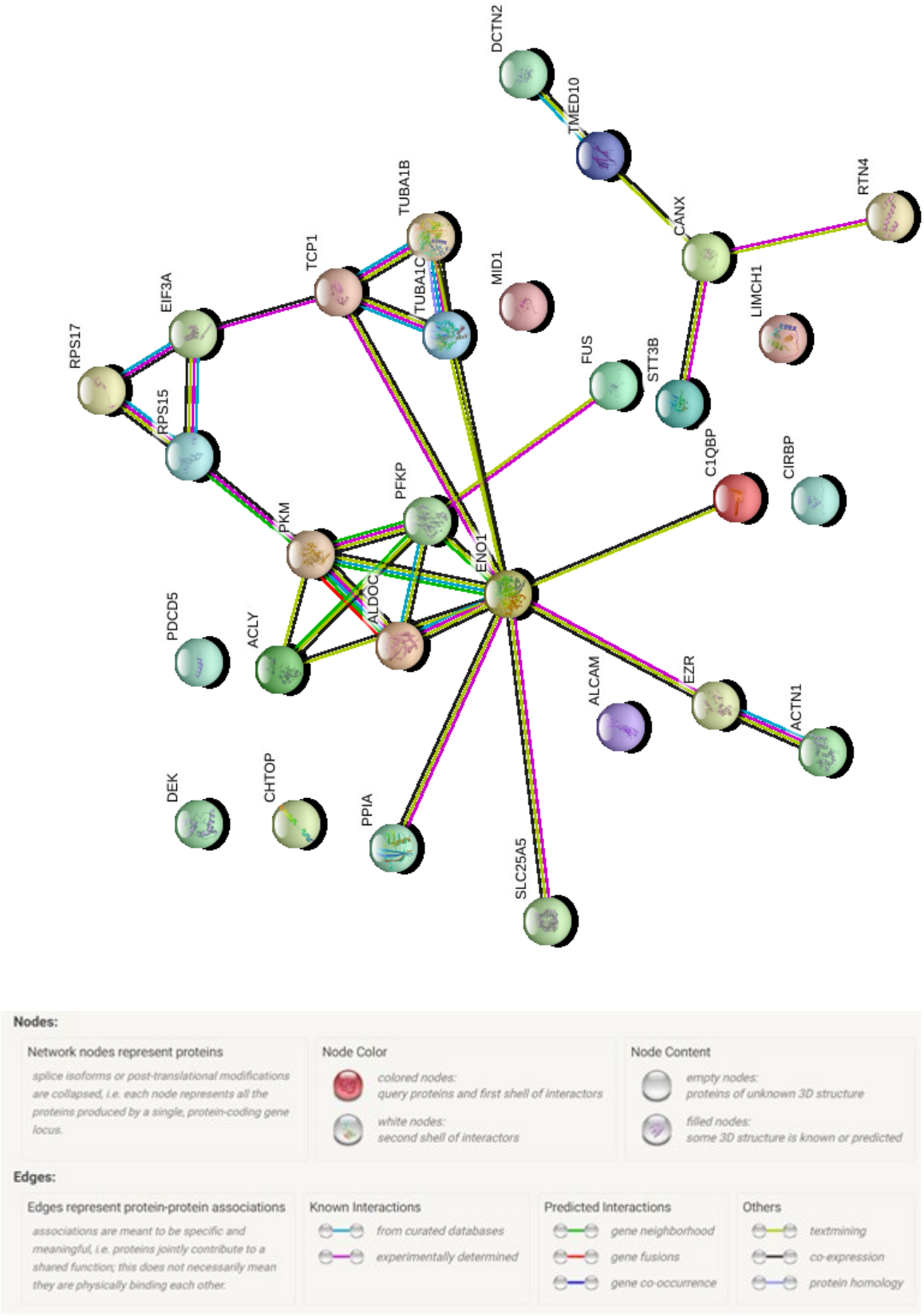

Supplementary figure 9. Bitmap of protein-protein interaction network in A549 ATGL-KO spheroids compared to WT group under normoxia**.** Obtained from STRING at https://string-db.org (106)**.**

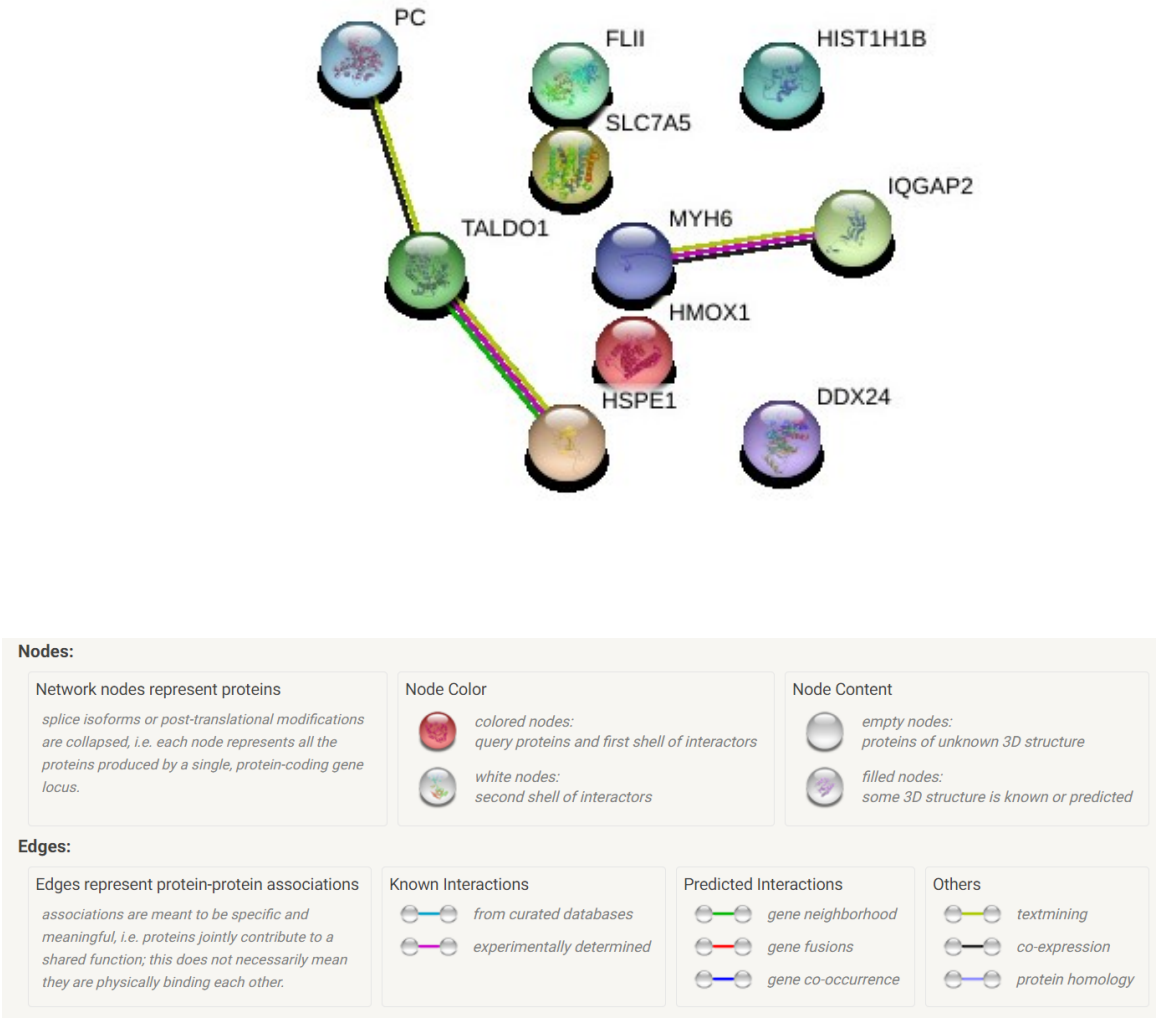

Supplementary figure 10. Bitmap of protein-protein interaction network in A549 WT spheroids compared to ATGL-KO cells under normoxia. Obtained from STRING at https://string-db.org (106).

Splitting and cultivation of A549 WT and ATGL-KO cells

1. Cells are subcultured at a confluency of 70% in T75 flask
2. For A549 WT cells → splitting 2:10, for ATGL-KO cells: splitting 1:10
3. Remove media and wash flask with 5 mL sterile PBS
4. Remove PBS and add 1 mL TrypLE Express (Thermo Fisher Scientific, USA), incubation for 2-3 minutes at 37°C, 5% CO_2
5. Control cells under light microscope if cells are detached completely
6. Add 9 mL pre-warmed, fresh medium (RPMI-1640 + 10% FBS + 1% P/S) and resuspend the cells to get single cell suspension (A549 cells tend to form clusters)
7. For subcultivation of A549 WT 2 ml of the single cell suspension and 8 mL new fresh media were used. For A549 ATGL-KO subcultivation 1 mL of the single cell suspension and 9 mL new media were used
8. Incubation the cells under 37°C, 5% CO_2

3-dimensional cell culture/spheroid formation

1. For 3D cell culture of A549 cell line, 10.000 cells in 100 µL medium are used per well
2. Cells are harvested as described above
3. Cell number from remaining cell suspension after splitting is determined by CASY cell counting (50µL of cell suspension in 10 ml of CASYton)
4. A single cell suspension with $1x10^5$ cells/mL is required
5. Pipette the calculated and required volume of single cell suspension in a centrifuge tube and centrifuge it for 5 min at 1200 rpm, RT
6. Remove the supernatant and dissolve the cell pellet in the necessary amount (100 µL for 1 well) of pre-warmed media
7. Pipette 200 µL PBS in each well at the edge of the Ultra-Low Attachment 96-well Plate (Corning) (in total 36 wells; to prevent evaporation of the cell suspension)
8. Pipette 100 µL of the single cell suspension ($1x10^5$ cells/mL) in each of the inner 60 wells. Make sure that the single cell suspension is mixed well so that the cell number is equal for each well
9. Centrifuge the plate for 20 min at 1200 rpm, RT

10. Control cell number with an aliquot of the cell suspension by CASY cell counting
11. Control spheroid formation with the microscope, each well should contain a dense, round shaped spheroid
12. Incubation 30 wells of the WT and 30 wells of ATGL-KO under standard conditions (21% O_2, 5% CO_2, 37°C) and incubation another 30 wells each of the WT and ATGL-KO under 1% O_2, 5% CO_2 and 37°C
13. After 3 days of incubation, collection and transfer the supernatants from 30 wells of each group into 2 mL microcentrifuge tubes separately (4 tubes used, 1x WT 21%O_2, 1x KO 21% O_2, 1x WT 1% O_2, 1x KO 1% O_2)
14. Collection and transfer the spheroids from the 30 wells into 1.5 mL microcentrifuge tubes separately using adjustable micropipette (4 tubes used)
15. Centrifuge all tubes (containing spheroids or supernatant) at 1200 rpm, RT for 5 min
16. Transfer 1 ml of the supernatants into new 1.5 mL microcentrifuge tubes separately (4 tubes altogether) and use them directly for the angiogenesis CAM assay
17. Remove remaining supernatants from the tubes containing spheroids and store the cell pellets at -80°C. They will then be used for the proteomics analysis

Proteomics sample preparation and analysis

1. Warm up the frozen cell pellets and remove remaining media
2. Wash cells 3 times with PBS (200 µL), then centrifuge in between at 4°C, 600 rcf for 5 min
3. Preparation lysis buffer of 5 ml

	Final concentration	Required volume
100 mM Tris HCL 8.5%	100 mM	4.25 ml
20% SDS	1% SDS	250 µL
10mM TCEP	10 mM	100 µL
40 mM CAA	40 mM	400 µL
Lysis buffer Σ		5 ml

4. Add 80µL of lysis buffer in each sample tube
5. Sonicate 1 kJ until pellet dissolved and solution is clear
6. Centrifuge the sample tubes at 15,000 g, RT for 5 min
7. Transfer supernatant of each sample to new eppis
8. Sample tubes on thermoshaker at 95°C for 10 min
9. Determine protein concentration with bicinchoninic acid-reducing agent compatible (BCA-RAC) protein assay:
    - Preparation of Diluted Albumin (BSA) Standards:
        - Pipette the required volume of Diluent and BSA (Bovine Serum Albumin) in 9 microcentrifuge tubes as the following schema:

Vial	Volume of Diluent (µL)	Volume of BSA (µL)	Final conc. (µg/ml)
A	0	300 of stock	2000
B	125	375 of stock	1500
C	325	325 of stock	1000
D	175	175 of B dilution	750
E	325	325 of C dilution	500
F	325	325 of E dilution	250
G	325	325 of F dilution	125
H	400	100 of G dilution	25
I (blank)	400	0	0

- Preparation the testing samples for the BCA assay:
    - Pipette 54 µL of H_2O and 6 µL of testing samples in new microcentrifuge tubes → to get a diluted solution of the samples in 60 µL with concentration of 1:10
    - Add 25 µL of each of standards, testing samples and blank into 2 wells of a 96-wells microplate
    - Then add each well 200 µL of BCA
    - Mix plate on a thermoshaker for 30 sec
    - Cover plate and incubate at 37°C for 30 min
    - Measure the light absorbance of each of the blank, standards and samples using a SPECTRAmax at wavelength 562 nm
    - Calculation the protein concentration of the testing samples using a standard curve diagram by plotting the absorbance of the standards vs its concentration in µg/mL

10. Dilute the samples with H_2O to get a volume of 100 µL
11. Protein precipitation with 500 µL of acetone overnight at -20°C
12. Next day → centrifuge the samples at 13000 rpm, 4°C for 10 min
13. Remove supernatant
14. Dissolve the pellet in a 50 µL buffer solution composed of 12.5 µL of 25% trifluoroethanol (TFE) and 37.5 µL of 100 mM Tris pH=8.5
15. Sonicate the solution with 1 kJ, until pellet is dissolved
16. Add 62.5 µL of ammonium bicarbonate to each sample to dilute TFE to 10%
17. Digest samples with 1 µL of LysC (1:100) for 2h, placed on a thermoshaker at 37°C
18. Then add 1 µL of Trypsin (1:100) and leave sample digestion at thermoshaker at 37°C overnight
19. Next day → transfer 8 µL of samples in new microcentrifuge tubes, then add 192 µL of 1% TFE → end volume 200 µL
20. Purification and desalting of the testing proteins using SDB-RPS STAGE tip:
    - Load the samples with trifluoracetic acid (TFA) into SDB-RPS Stage tip (200 µL tip packed with 2 layers of SDB-RPS material)
    - Place the tips onto a 2 ml tube attached with a red adapter

- Centrifuge the tips with sample at 1500 rcf for 5-10 min → until no liquid remains in the tip
- Wash tips with 200 µL of 0.2% TFA
- Centrifuge tips at 1500 rcf for 5-10 min → until no liquid remains in the tip
- Attach the tips onto a new 2 ml tube containing a glass vial insert with a red adapter
- Elute the peptides in the tips with 200 µL of 5% ammonium hydroxide in 80% acetonitrile (ACN)
- Centrifuge the tips at 1500 rcf for 5-10 min, until no liquid remains in the tip
- Detach the tips and adapter from the tube with glass vial insert

21. Dry down the samples in the vial inserts in a speed vac for 1-2 h
22. Freeze the samples at -20°C overnight
23. Next day → dilute and dissolve the samples with running buffer A (ACN and 0.1% formic acid)
24. 1 µg of sample was used for LC-MS/MS analysis:
    - Measurement done in 2h by Ultimate 3000 RCS Nano Dionex system equipped with a Ionoptiks Aurora Series UHPLC C18 column (250 mm x 75 µm, 1.6 µm) (Bruker Daltonics, Germany) coupled to a Orbitrap Velos Pro (Thermo Scientific, USA)

Chorioallantoic membrane collagen assay

Preparation of eggs:

1. Clean incubator (Incubator Easy200, J.Hemel Brutgeräte, Germany) and trays with water and soap, then with 75% ethanol
2. Fertilized white Leghorn eggs are cleaned with warm water (not hot!!), using toothbrush to remove dirt
3. Put the eggs on racks and let them dry
4. Dry eggs are sprayed with 75% ethanol and let them dry
5. Make sure that the eggs are preferably placed in front of tray, because it makes taking out the eggs easier later on
6. Eggs are incubated at 37.6 °C and 60% humidity, make sure water bath is filled
7. Incubate eggs for 3 days

Preparation of sterile dishes:

1. Spread some paper tissues on surface of table
2. Put 75% ethanol in a big beaker
3. Immerse plastic dishes (85x85x24 mm, PS, medium, white) in 75% ethanol in beaker
4. Ethanol can be reused, store in a flask
5. Lay the dishes upside down on a paper tissue, till they dry
6. Then lay the dishes in a UV machine (UV-BOX-E2/40H-NX-R, Light Progress, Tuscany, Italy) for at least 16 minutes
7. Cover the dishes with sterile square Petri dishes (Barelt/Simport) covers
8. Store the dishes in a box covered with aluminium foil to keep them sterile and clean
9. During the whole process don't touch the inside part of the dishes → keep them sterile, always hold the dishes on the edge or bottom
10. Preparation of dishes should be done at least one day before egg cracking
11. Always prepare more than required

Cracking eggs:

1. After 3 days of incubation, eggs are cracked using a drill
2. Place chick embryo in sterilized dishes and cover them with a lid of a square Petri dish
3. *Ex ovo* cultivation is carried out at 37.6 °C and 60% humidity

Preparation of grids:

1. Cut nylon material (Nitex nylon mesh with 180 µm grid size from Sefar America, Inc., Kansas City, MO) into 2 and 3 mm thick stripes and then into 2x2 & 3x3 mm squares using a cutter
2. Place the grids in a Petri dish and sterilize the grids with UV (UV-BOX-E2/40H-NX-R, Light Progress, Tuscany, Italy) for 16 minutes
3. Prepare more grids then necessary
4. Sterile a square Petri dish
5. Lay a Parafilm on the inside of the Petri dish and spray 75% ethanol on the Parafilm
6. Lay 3x3 mm squares on the Parafilm using sterile forceps (→ it works better if the forceps are wetted previously with ethanol)
7. Put 2x2 mm squares on top of the 3x3 mm grids
8. Recommended using a light microscope to see the grids
9. Let grids dry
10. Important: don't move the petri dish fast or handle it too harshly, as the arrangement of the grids will be destroyed and therefore must start all over again

Preparation of mastermix and onplants:

1. Whole process must be performed on ice, to prevent premature polymerization of collagen
2. Pipette tips should also be kept in freezer at least a day before
3. 30 µL of the mastermix is required for 1 onplant
4. For this experiment 36 onplants per group were used → i.e. formation of 1080 µL of mastermix for each group

5. Add required volume of 10X Minimum Essential Medium Eagle (MEM) (Sigma-Aldrich, Austria) into a 2 ml microcentrifuge tube
6. Add required collagen (Rat Tail, Corning) (pay attention to the concentration) and 4-(2-hydroxyethyl)-1-piperazineethanesulfonic acid (HEPES) (Sigma-Aldich, Austria) into the tube, mix well
7. The formed liquid is yellow and has an acidic pH
8. Add NaOH dropwise (10-30 µL/drop) until color of mixture changes and becomes pink
9. Add the required volume of supernatant in the mastermix
10. Pipette 30 µL mastermix on the previously prepared grids → 1 onplant
11. Incubate the grids with mastermix at 37°C for at least 30 min (CO_2 Incubator, Binder, Germany)
12. Transfer the onplants with sterile forceps on the eggs → max. 6 onplants on 1 egg
13. 5-6 eggs were used for each group, important to label on the cover the number of egg and grids, also the testing group
14. Incubate the eggs with grids (Incubator Easy200, J.Hemel Brutgeräte, Germany) for 3 days at 37.6 °C and 60% humidity

Stock solution	Final concentration	Volume for 36 onplants
10X MEM w/o supplements	1x MEM	108 µL
Collagen	2 mg/ml collagen	e.g. 600 µL, if c= 3.36 mg/ml)
1 M HEPES	10 mM HEPES	10.8 µL
1 M NaOH	Add dropwise	44 µL
Testing substance	Remaining volume	317.2 µL
Mastermix Σ		1080 µL

Analysis of grids and scoring of angiogenesis

1. Counting using stereomicroscope (Olympus, Japan) at magnification of 6.3x
2. Focus on the upper mash/grid
3. Count all grids of the upper mash that are:
    - directly above the bottom mash
    - surrounded by 4 borders
    - visible and not to densely
4. Count all grids that show vasculature while focusing on the upper mash
5. Calculate ratio of vasculated to not vasculated squares (angiogenic index)